Laboratory Investigation of Disperse Multiphase-Turbulent Flows

Dilute & Dense Distributions of Inertial Particles Settling in Air

A DISSERTATION

SUBMITTED TO THE FACULTY OF THE GRADUATE SCHOOL

OF THE UNIVERSITY OF MINNESOTA

BY

Alec J. Petersen

IN PARTIAL FULFILLMENT OF THE REQUIREMENTS

FOR THE DEGREE OF

DOCTOR OF PHILOSOPHY

Filippo Coletti

May, 2020

Acknowledgements

Most scientists I think pursue a PhD because we are passionate and curious about the mysteries of our universe. In my case, I fell in love with physics and understanding how the universe acts on itself to produce the galaxies and stars; the planets and moons; the oceans and mountains; the animals and forests; everything around me and everything I sense and experience. How intoxicating it was to learn as an undergraduate I could mathematically describe so much! And how alluring it seemed to join the legions of scientists working to figure out all the rest! My path took me to turbulence. While thinking about the unseen world–studying quantum mechanics for example–was exotic and fun, knowing that in our classical world there was just as much mystery once you removed the undergraduate lens of classical physics. A cow is not really a sphere, as that physicist jokes goes; and our world is not so easily simplified as often presented in those undergraduate classes. Nature is complex and chaotic so to study turbulent fluid dynamics–physics that shows up literally everywhere–seemed an opportunity to make a contribution to our understanding of the universe as a whole.

However as Shevek says in Ursula K. Le Guin's "The Dispossessed":

If you can see a thing whole it seems that it's always beautiful. Planets, lives...But close up, a world's all dirt and rocks. And day to day, life's a hard job, you get tired, you lose the pattern. You need distance, interval. The way to see how beautiful the earth is, is to see it as the moon. The way to see how beautiful life is, is from the vantage point of death.

I would guess my experience in graduate school was not unique. Many of us I think, lose sight of the thing whole. It is easy to lose perspective: the day-to-day grind wears you down; the research question can seem so specific as to be meaningless; some form of despair and regret undoubtablely plagued me during the course of graduate school. Much of that I think is learning what research is and what it is not. The reality does not compare to the ideal I held prior to graduate school. Science, as a human institution, is littered with the same imperfections of our society on large. Ego often seems more common a driver of science than curiosity. Financial survival drives research agendas. Truth and knowledge are not pursued–citation and publication counts are. All the forms of oppression are reproduced in academia and our shared science seems to engender little solidarity and less drive to collectively build better institutions. For me to come in to academica so naïve means these hardships are not acknowledged enough. We have to acknowledge these truths, all of us, collectively, before we can work together to change the reality of doing science in academia.

This thesis is a product of our imperfect institution of science, and although it presents a coherent, finished whole, know that the process was anything but. Compiling it here and in my dissertation presentation however did help me see my work from that necessary distance, which I am thankful for. How inertial particles settle in a fluid is one of those foundational questions that shows up everywhere, so I'm hopeful the story presented here will be of use to whoever you are, reading my dissertation.

her love and support over the years. Her empathy and intelligence are inspirational, and I couldn't imagine the past two and a half years without her in my life.

My foremost thanks go to my parents, Donna and Gary, without whom nothing I do is possible. It too often goes without being said, so let me formalize my gratitude here: Mom and Dad, your constant support and love is something I am truly thankful for. I would not be the person I am without you both and I am proud to be your son.

Lastly I want to acknowledge this place–the city and state I've come to love and appreciate. Every day going into lab, I got to look over the Mississippi River and see the Minneapolis skyline over the St. Anthony Falls. We probably have the best view of the city from SAFL. It is a city I've come to love. When I first arrived I was 21, alone and knowing no one around me for 1000 miles. Now I'm leaving at 27, with many dear friends, cherished memories and most importantly, a better sense of myself as an adult, who I am and what my values are. A lot of that growth, and much of what I've accomplished, is due to being here, around the people I just thanked, and all the countless others whose lives have brushed up against mine. Minneapolis is a unique place with a unique character: I am so happy to have experienced May Day in Minneapolis, to have celebrated Halloween in Hidden Falls Park with the Barebones Halloween Puppet Extravaganza, to have biked along the river and around the lakes countless times. To have skiied on winter mornings before heading into the lab. All the brewery hopping, nights out dancing, dinner parties, backyard BBQs...there are many memories from this city I will always cherish. This state also provided me with so much I didn't anticipate. Through all the hikes, nights out camping and cabin trips, I've been exposed to the land and nature of this place. I did not know how beautiful the shoreline of Lake Superior is in autumn, or the joys of a backwoods cabin in the middle of a snowy January. These things too, have become a part of me, and a part of this place will travel with me wherever I go.

And yet, it is important to acknowledge that despite being dear to me, this place

as I know it is built on a foundation of injustice. The University of Minnesota-Twin Cities is built within the traditional homelands of the Daķota people. *Minnesota* comes from the Daķota name for this region, Mni Sota Maķoce–"the land where the waters reflect the skies". The university itself is a land-grant university, originally funded with expropriated Indigenous land. It is unceded sacred land of the Daķota people, the ancestral land of the Ocheti Sakowiŋ. What does it mean that everyday I look out over the Wakpá Tháŋka, the Mississippi River, and the Owámniyomni, the St. Anthony Falls, and am grateful for that view? What does it mean to love something that was forged by, to put it mildly, a complicated past with further injustices continuing everyday? What does it mean to recognize ongoing settler colonialism and the ways that the state of Minnesota, the city of Minneapolis and the University of Minnesota have benefitted from the forced and systematical removal of Indigenous peoples? What does it mean to acknowledge my life has been built and supported by such injustices? I am thankful that living here, I have been confronted with these considerations. I think they should be a call to action. Let us recognize and support tribal sovereignty here in Minnesota and the country at large. Let us respect this land, acknowledge the harms and mistakes of the past, and dedicate ourselves to move forward for respectful partnerships with Indigenous people as we strive for collective healing and true reconciliation. This could mean reparations, land repatriation, other anti-colonial practices–but fundamentally it means a radical reshaping of our world. I understand the hesitation to change something one loves. But let us acknowledge that a different, more just future is possible. A future where the opportunity I've been afforded here is not denied to others. We are fundamentally responsible for each other and for that brighter future. Let us work to build it together.

Dedication

To my parents, Donna and Gary–everything I've done and will do is because of you and for you. I love you.

Abstract

Turbulent multiphase flows are found throughout our universe, all over Earth and in many man-made systems. Despite surrounding us, their dynamics are still in many ways obscure and require further study. These chaotic systems are however quite complicated to both simulate or explore experimentally. In this thesis, we present our laboratory investigation of particle-laden turbulent flows in air. We first focus on the statistical dynamics of dilute multiphase turbulence. Utilizing a zero-mean-flow air turbulence chamber, we drop size-selected solid particles and study their dynamics with particle imaging and tracking velocimetry at multiple resolutions. The carrier flow is simultaneously measured by particle image velocimetry of suspended tracers, allowing the characterization of the interplay between both the dispersed and continuous phases. The turbulence Reynolds number based on the Taylor microscale ranges from $Re_\lambda \approx 200$ – 500, while the particle Stokes number based on the Kolmogorov scale varies between $St_\eta = O(1)$ and $O(10)$. Clustering is confirmed to be most intense for $St_\eta \approx 1$, but it extends over larger scales for heavier particles. Individual clusters form a hierarchy of self-similar, fractal-like objects, preferentially aligned with gravity and sizes that can reach the integral scale of the turbulence. Remarkably, the settling velocity of $St_\eta \approx 1$ particles can be several times larger than the still-air terminal velocity, and the clusters can fall even faster. This is caused by downward fluid fluctuations preferentially sweeping the particles, and we propose that this mechanism is influenced by both large and small scales of the turbulence. The particle-fluid slip velocities show large variance, and both the instantaneous particle Reynolds number and drag coefficient can greatly differ from their nominal values. Finally, for sufficient loadings, the particles generally augment the small-scale fluid velocity fluctuations, which however may account for a limited fraction of the turbulent kinetic energy. We also investigate denser particle-laden flows, specifically plumes driven by the downward buoyancy of inertial particles. With similar

tools, we conduct two experiments: one to capture the particle-phase behavior and another to measure the ambient air velocity. Our first focus is on the assumption of self-similarity, which unlike single-phase plumes is not a trivial assumption. We also characterize the mean plume properties observed: the particle-phase velocity and the plume spread comparing their evolution with axial distance from the plume source. From our measurements of the ambient air flow we calculate the entrainment velocity into the particle-laden plumes and using the time-averaged value we estimate the entrainment coefficient along the plume. We find a relatively stable entrainment rate, as expected in the assumption used to formulate many integral plume models. Lastly we compared our experimental results to single and multiphase plume models with the same initial conditions as our experiments. Our multiphase plume model, inspired by the work of Liu (2003) and Lai *et al.* (2016), well described our velocity measurements, which single phase models were completely unequipped for.

Contents

List of Tables

List of Figures

Chapter 1

Introduction

This thesis concerns laboratory experiments of multiphase-turbulent flows, a mouthful that deserves some explanation. *Multiphase* simply refers to the phases of matter: solid, liquid, gas and plasma. A multiphase flow is then any flow with two or more phases. My thesis concerns *disperse* multiphase flows specifically, meaning those consisting of finite particles, droplets or bubbles interspersed in a continuous phase—a fluid like air or water. What *turbulent* means deserves a lot more explanation, but to attempt to do so would be worthy of a whole thesis of its own, and would still be neither sufficient nor definitive. But we are all intimately familiar with turbulence, whether we have studied it mathematically or not. From your very breath—at this moment—moving through your larynx into and out of your lungs, to the wind that reshapes clouds in the sky and the water rushing over a waterfall, to the smoke plume from a cigarette, turbulent flows are everywhere. And not just here on Earth, all throughout the universe you'll find turbulence. You also see it in the churning plasma of our sun and even in the interstellar medium, forming the stars and planets of solar systems like ours.

Disperse multiphase turbulent flows are similarly familiar to you. Those clouds above you are made up of water vapor and droplets continuously mixed in the turbulent air of the atmosphere. Volcanic eruptions, snow, rain, avalanches, sandstorms, sediment transport are all disperse multiphase flows. So too is the blood flow in your veins, or the inhaler you might use to deliver medication to your lungs. In industrial settings, disperse multiphase flows are also ubiquitous. Any granular material, like grain, that has to be transported, at some point or another has to flow. To make paper requires flows suspended with fibers; bubbly flow appears in nuclear reactors and there is gas-particle flow in combustion reactors, among countless other examples.

But for all their ubiquity, making predictions about these flows can be quite challenging. Fluid dynamics is a visually stunning discipline (admire figure 1.1 for examples of turbulent multiphase flows). But the beauty of the flows contrasts sharply with the nasty equations that govern turbulence in particular. There is no beautiful theory of
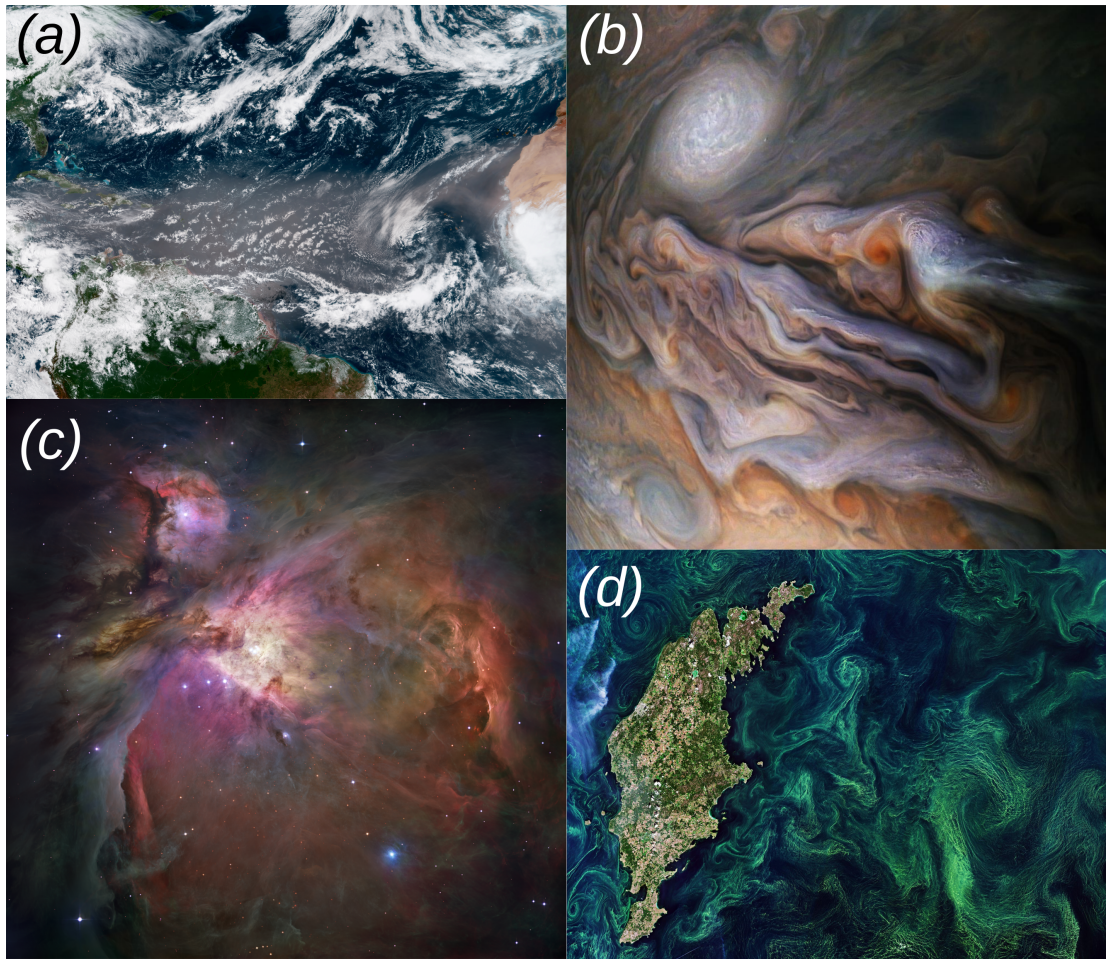
Figure 1.1: (a) A plume of Saharan dust, transporting sand and minerals across the Atlantic (credit: NOAA Environmental Visualization Laboratory); (b) Swirling storms on Jupiter (credit: Enhanced image by Gerald Eichstädt and Sean Doran (CC BY-NC-SA) based on images provided courtesy of NASA/JPL-Caltech/SwRI/MSSS); (c) Turbulent plasma and interstellar medium in the Orion Nebula seen by the Hubble Telescope (credit: NASA, ESA, M. Robberto (Space Telescope Science Institute/ESA) and the Hubble Space Telescope Orion Treasury Project Team); (d) Algal bloom in the Baltic Sea seen from space (credit: ESA CC BY-SA 3.0 IGO).

turbulence as there is in other fields of physics, like Maxwell's laws of electromagnetism, or Einstein's general relativity. Instead, turbulence theory is a mash up of messy tensor equations, closure models, semi-empirical formulas and statistical theorems. Multiple phases only further complicates the picture. To explain why requires at least a cursory definition of turbulence and a review of some of the essentials equations and terminology of fluid dynamics and multiphase flows.

1.1 Turbulence

To define turbulence generally, one could say that it is a state of a physical system with many interacting degrees of freedom deviated far from equilibrium, irregular in time and space and accompanied by dissipation (Cardy *et al.*, 2008). Though fluid dynamics is not the only system where turbulence exists, it is the one being addressed here.

The foundation of fluid mechanics lies in the conservation of mass and momentum as expressed through two differential equations.

$$\frac{\partial \rho}{\partial t} = -\nabla \cdot (\rho \boldsymbol{u}) \tag{1.1}$$

$$\frac{d(\rho \boldsymbol{u})}{dt} = \nabla \cdot \boldsymbol{\sigma} \tag{1.2}$$

Here, ρ is the fluid density, $\boldsymbol{u}$ is the fluid velocity and $\boldsymbol{\sigma}$ is the stress tensor. If the stress tensor can be expressed in terms of the density and velocity field, then the equations are closed and can in principle be solved for any arbitraty geometry, given some boundary condidtions. While there is no *a priori* reason such a relation should exist, very often a suitable constitutive law can be found which allows for solution of equations 1.1, while providing insight into what processes control the flow. One well known constitutive law is that for a Newtonian fluid, such as air or water, with a viscosity ν. The stress tensor for these fluids, which we will be dealing with exclusively in this thesis, can be expressed

as follows:

$$\sigma_{ij} = -\left(p\delta_{ij} + \frac{2}{3}\rho\nu\nabla\cdot\boldsymbol{u}\right) + \rho\nu\left(\frac{\partial u_i}{\partial x_j} + \frac{\partial u_j}{\partial x_i}\right) \ , \tag{1.3}$$

where p is the isotropic pressue, u_i are the components of the velocity vector and x_i are the spatial coordinates. Substituting this back into the momentum equation leads to the well known Naiver-Stokes equation:

$$\rho\frac{\partial\boldsymbol{u}}{\partial t} = -\rho(\boldsymbol{u}\cdot\nabla)\boldsymbol{u} - \nabla p + \rho\nu\nabla^2\boldsymbol{u} \tag{1.4}$$

The complexity of the Navier-Stokes equation arises from the humble nonlinear term with the dependent variable, the fluid velocity $\boldsymbol{u}$, appearing in a quadratic form. This term means that fluid motion is inherently unstable, with small perturbations causing instabilities and potentially being propogated by inertia throughout the flow as eddies, or vortices. The largest eddies produced by the instabilities are themselves subject to the nonlinear inertial forces leading to their breakup into smaller eddies. In that manner, with each new instability comes a new degree of freedom for the system. Controlling these instabilities is the fluid viscosity, which if strong enough, or if the eddies are small enough, can dampen them through dissipation. The protagonists for any fluid flow are thus inertia and viscosity and their relationship is captured by the Reynolds number, Re. When a fluid with velocity U and viscosity ν is perturbed on a scale D, it will become chaotic when inertia dominates viscous dissipation, e.g. when $Re >> 1$.

We generally cannot solve such a nonlinear equation analytically. We can solve it numerically, integrating forward in time to find the velocity field at each small time-step, yet such computation is expensive, requiring vast computational resources for even the most simple configurations. Not all structure is lost in the chaos however. Some statistical properties, e.g. the velocity fluctuations of the turbulent flow, seem to be predictable,

at least when discussing their probability distributions. Most theories of turbulence have thus focused on these statistical quantities and seek to divine what features of turbulence are universal. Richardson in 1921 observed the continual eddy breakdown and hypothesized the concept of the *energy cascade*–that as the eddies breakdown they pass their energy onto those smaller structures and so on until viscosity dissipates them into heat. Kolmogorov indelibly influenced the field in 1941 with his theory of turbulence which stated that the statistical properties of the smallest scales, where viscosity finally wins out dissipating the turbulence, depend only on the viscosity ν and on the rate at which energy is passed down the energy cascade. Those smallest scales–the Kolmogorov length (η), time (τ_η and velocity (u_η)–are statistically isotropic and universal. These are just the two most famous contributions to turbulence theory and as an active field of study, with over a century of study, we cannot summarize turbulence theory here adequately, nor will the theory of turbulence further feature in this thesis. The point however, is to say that the study of turbulence is not completely hopeless. There is a path forward, through observation of the statistical properties of turbulent flow.

1.2   Fundamentals of Particle-Laden Flows

The turbulent transport of matter by fluid flows is an important phenomenon, pervasive throughout the fields of earth science, astrophysics, biology, medicine, chemisty and engineering. Turbulence is already one of the most challenging topics of classical physics, and when combined with multiphase flows, they present an even greater challenge as a couple. Even when the dispersed phase is a passive tracer–following the turbulent flow field precisely, the random distribution of the large number of particles one might find in a real environmental or industrial flow humbles even our most advanced computers today. Again further complicating the picture is the presence of *intertial* particles, the topic of this thesis. Inertial particles, droplets or bubbles feel a frictional force in the fluid, proportional to their relative velocity with respect to the fluid, also known

as the slip velocity. It is this interaction between the phases, the coupling between them, that makes studying turbulent multiphase flows so difficult. The dynamics of an inertial dispersed phase in turbulence follow chaotic non-differentiable governing equations–and these systems display all sorts of unpredictable behaviors that affect the dispersed phase transport and, at high concentrations, the turbulent fluid itself.

The addition of a dispersed phase introduces many new parameters and important non-dimensional parameters used to characterize the multiphase flow. The dispersed phase concentration is an obvious parameter, and in this thesis will mainly be indicated through the volume fraction ϕ_v, the ratio of the total volume of the dispersed phase in a system to the total system volume. Multiphase flows are often classified as dilute or dense by their volume (or mass) fraction. Dense flows are dominated by interparticle collisions while dilute ones are not. The separation between a dilute a dense flow is usually taken to be around $\phi_v \sim O(1)$. Among the dilute regime there are further classifications. When the volume fraction is small, the particles have an insignificant effect on the fluid. This regime is called *one-way coupled*, in that the fluid affects the particles, but the particles do not (detectably) affect the fluid. Generally dilute flows with $\phi_v < 10^{-6}$ can be approximately as one-way coupled flows (Crowe *et al.*, 2011). Above this (flexible) threshold, the flow becomes *two-way coupled*, in which both the disperse and continuous phases significantly affect each other. Momentum transferred between the particles and the fluid changes the turbulence structures, and can either enhance or attenuate the turbulence, though the exact nature of the relationship is unclear. At higher volume fractions we enter regimes of *four-way coupling* where the dispersed phase is now dense enough that particle-particle interactions become significant. The threshold for four-way coupling is generally considered to be around volume fractions of 10^{-3} (Elghobashi, 1994).

We can also define a Reynolds number for the particles, and this particle Reynolds

number (Re_p) is again a balance of inertial and viscous forces, given as:

$$Re_p \equiv \frac{\rho_f d_p |\boldsymbol{u_p} - \boldsymbol{u_f}|}{\mu} \tag{1.5}$$

where ρ_f is the density of the fluid, d_p is the particle diameter, $\boldsymbol{u_p}$ is the particle velocity vector, $\boldsymbol{u_f}$ is the fluid velocity vector and μ is the fluid dynamic viscosity. Larger values Re_p correspond to a higher slip velocity between the disperse and continuous phases, implying longer-lasting and more turbulent wakes. One of the most important non-dimensional parameters in multiphase flows is the Stokes number, defined as:

$$St \equiv \frac{\tau_p}{\tau_f} \tag{1.6}$$

where τ_p is the particle aerodynamic response time and τ_f is some characteristic fluid time scale. The particle aerodynamic response is defined as the time it takes for a particle injected into a uniform stream at zero initial velocity to reach $1 - e^{-1} \approx 63\%$ of the freestream velocity. It is thus a measure of the particle's inertia–how resistant a particle is to changes in the flow velocity. Of course in turbulence, the flow velocity in constantly changing. Commonly the Kolmogorov time scale of the turbulence ($\tau_\eta \equiv \sqrt{\nu/\varepsilon}$, where ν is the fluid kinematic viscosity and ε is the turbulent dissipation rate) is used as the fluid time scale and this Stokes number based on the Kolmogorov time scale is written St_η. The Stokes number compares responsiveness of a solid particle to the rapidity of turbulent fluctuations; particles with $St_\eta << 1$ correspond to flow tracers able to follow the smallest scale turbulent fluctuations, while particles with $St_\eta >> 1$ are unresponsive to all but the largest turbulent scales.

1.2.1 Particle Equation of Motion

The dispersed phase follows its own governing equations that must be satisfied. However the coupled nature of the phases means that these equations will both be fed by, and

feed into the fluid phase conservation laws described above. Both the particle's mere presence and its movement relative to the fluid will modify the fluid flow field, which in turn changes the particle's trajectory. Maxey & Riley (1983) derived an equation for the motion of small (i.e. $d_p < \eta$) spherical particles based on the work of Tchen (1947) and others:

$$
\begin{aligned}
m_p \frac{d\boldsymbol{u_p}}{dt} = & -3\pi\mu d_p \left(\boldsymbol{u_p} - \boldsymbol{u_f} - \frac{1}{24}d_p^2\nabla^2\boldsymbol{u_f} \right) \\
& - \frac{3}{2}\pi d_p^2\mu \int_0^t \frac{\frac{d}{d\tau}(\boldsymbol{u_p} - \boldsymbol{u_f} - \frac{1}{24}d_p^2\nabla^2\boldsymbol{u_f})}{\sqrt{\pi\nu(t-\tau)}} d\tau \\
& - \frac{1}{2}m_f \frac{d}{dt} \left(\boldsymbol{u_p} - \boldsymbol{u_f} - \frac{1}{40}d_p^2\nabla^2\boldsymbol{u_f} \right) \\
& + m_f \frac{D\boldsymbol{u_f}}{Dt} + (m_p - m_f)\boldsymbol{g}
\end{aligned}
\tag{1.7}
$$

where m_p is the mass of the fluid and m_f is the mass of fluid displaced by the particle. In this formulation, d/dt denotes a substantial derivative following the particle such that $d/dt = \partial/\partial t + \boldsymbol{u_p} \cdot \nabla$ and D/Dt is a substantial derivative following the fluid with velocity u_f so that $D/Dt = \partial/\partial t + \boldsymbol{u_f} \cdot \nabla$.

This messy-looking force balance has been improved upon (notably Bagchi & Balachandar (2003), who improved the applicability in turbulent flows), but the essentials of the equation remains the same. The first term on the right-hand side is the steady viscous Stokes drag with the Faxem correction, accounting for the variation of the fluid velocity around the particle. The second term is the Basset history force, accounts for the past trajectory of the particle through the flow. It can be neglected for most dilute flows where either particle-particle collisions are unimportant or when the particle density is much greater than the fluid density (Rogers & Eaton, 1989; Kulick *et al.*, 1993). The third term is the added-mass force required to overcome the inertia of the fluid displaced by the particle. Although important in unsteady flows, it can also generally be neglected when the particle density is much larger than the fluid density. The fourth

term is the force exerted by the pressure gradient and the viscous stresses in the unperturbed fluid. Finally, the fifth term is the body force exerted by gravity.

Despite its complexity, this equation is already an approximation as it relies on three simplifying assumptions: that the particle Reynolds number is small ($Re_p << 1$, that the strain rate is small ($d_p^2/(\nu\tau_\eta) << 1$) and that the particle is small compared to the Kolmogorov length scale as stated above. It also relies on Stokes drag, which inevitably will not faithfully represent the drag felt by a particle. Outside the regimes for which Stokes drag is valid (in particular, vanishingly small Re_p), empirical correlations such as the one of Schiller and Naumann are often used (Schiller & Naumann, 1933). The work in this thesis addresses the accuracy of the standard Schiller & Naumann drag formulation.

The general form of eq. 1.7 can be simplified in certain cases, one being gas-solid flows which we will deal with exclusively throughout this thesis. For small particles, much denser than the fluid phase, the added mass and fluid acceleration terms can be neglected, as can the Basset history force when particle collision effects are negligible, a reasonable assumption for $\phi_v < 10^{-3}$. Under these assumptions, the particle equation of motion simplifies greatly becoming (Bagchi & Balachandar, 2003):

$$\frac{d\boldsymbol{u_p}}{dt} = \boldsymbol{g} - \frac{1}{\tau_p}(\boldsymbol{u_p} - \boldsymbol{u_f}) \tag{1.8}$$

where the particle response time is corrected for finite Re_p:

$$\tau_p = \frac{\rho_p d_p^2}{18\mu}\frac{1}{1 + 0.15Re_p^{0.687}} \tag{1.9}$$

1.2.2 Challenges posed by turbulent multiphase flows

While this equation has been greatly simplified compared to 1.7, it is still coupled to the turbulent fluid velocity and therefore is difficult to solve. While numerical simulations have proved valuable, multiphase flow siulations are often simplified, e.g. by

solving multiphase flows only at the macroscale, while using models to approximate the physics at the microscale or by simulating lower Reynolds number turbulence or only incorporating a small number of particles into the simulation (Balachandar & Eaton, 2010). Another approach is to coarse-grain the simulation spatial resolution such as in volume-averaging methods (Prosperetti & Tryggvason, 2009). Properly used, these mesoscale simulations can accurately model complex multiphase flows relatively inexpensively (Agrawal *et al.*, 2001; Capecelatro *et al.*, 2015).

Since the seminal work of Eaton and Elghobashi, a widespread approach has been to model particles as material points and track their Lagrangian trajectories through the Eulerian flow field obtained by direct numerical simulation (DNS) which numerically solve the Navier-Stokes equations by resolving all spatio-temporal scales of motion down to the Kolmogorov scales. This led to groundbreaking insights, both when treating the particles as passively advected by the fluid (one-way coupling, Squires & Eaton 1991a; Elghobashi & Truesdell 1992) and when including their backreaction on the fluid (two-way coupling, Squires & Eaton 1990; Elghobashi & Truesdell 1993). This approach, however, has well-known limitations. As mentioned, the particle equation of motion assuming Stokes drag (even with the correction terms derived by Maxey & Riley 1983) is only applicable when particles are much smaller than Kolmogorov scale, and finite-Re_p effects are minimal. Indeed, although the one-way-coupled DNS has led to overall agreement with experiments (e.g., for Lagrangian accelerations, Bec *et al.* (see 2006); Ayyalasomayajula *et al.* (see 2006), quantitative discrepancies indicate that the Stokes drag model may miss important dynamics (Saw *et al.*, 2014). Moreover, modeling the backreaction of the dispersed phase by point-particle methods present technical issues associated with the application of the point-wise forcing on the fluid computational grid (Balachandar, 2009; Eaton, 2009; Gualtieri *et al.*, 2013). To overcome these shortcomings, advanced methods have recently been proposed (Gualtieri *et al.*, 2015; Horwitz & Mani, 2016; Ireland & Desjardins, 2017) whose merits need to be fully appreciated in

future comparisons with well-controlled experiments. Setting up the turbulent flow in two-way coupled simulations is also a critical issue: forcing steady-state homogeneous turbulence in either Fourier or physical space leads to artificial energy transfers hardly discernible from the actual interphase dynamics (Lucci *et al.*, 2010). Decaying turbulence leaves the natural coupling unaltered, but quickly drops to low Reynolds numbers and complicates the extraction of statistical quantities.

Laboratory measurements also present significant challenges, especially to extract the fluid flow information. Techniques such as Laser Doppler Velocimetry (LDV), Particle Image Velocimetry (PIV) and Particle Tracking Velocimetry (PTV) require tracers that need to be discriminated from the inertial particles. This can be achieved in LDV by signal-processing schemes (Rogers & Eaton, 1991; Kulick *et al.*, 1994), which are relatively complicated and require careful adjustment (Balachandar & Eaton, 2010). Moreover, single-point techniques as LDV cannot capture the flow structures and particle clusters that are essential in the dynamics, and as such they have been superseded by whole-field methods, either by conventional or holographic imaging. Time-resolved 3D PTV (often termed Lagrangian Particle Tracking) has been successfully used to investigate inertial particle acceleration (Ayyalasomayajula *et al.*, 2006; Gerashchenko *et al.*, 2008; Volk *et al.*, 2008), dispersion (Sabban & van Hout, 2011), relative velocity (Bewley *et al.*, 2013; Saw *et al.*, 2014), and collision rates (Bordás *et al.*, 2013). A limitation of this approach is the low particle concentration needed for unambiguous stereo-matching from multiple cameras; this has prevented the volumetric investigation of clustering. For the same reason, experimental studies where both inertial particles and fluid tracers are captured in three dimensions are scarce, Guala *et al.* (2008) being a rare exception. Two-dimensional (2D) imaging has proven capable of capturing inertial particle distributions and velocities as well as the underlying flow field. Clustering has been probed by 2D imaging since Fessler *et al.* (1994), and multiple approaches have since been utilized to characterize concentration fields, as reviewed by Monchaux *et al.*

(2012). To obtain two-phase measurements, the fluid tracers and inertial particles can be discriminated based on their image size and intensity (Khalitov & Longmire, 2002) and digital/optical filtering (Kiger & Pan, 2000; Poelma *et al.*, 2007). The motion of the continuous and dispersed phases is then characterized by PIV and PTV, respectively. This approach has allowed the investigation of particle-turbulence interaction in wall-bounded (Paris, 2001; Kiger & Pan, 2002; Khalitov & Longmire, 2003) and homogeneous flows (Yang & Shy, 2003, 2005; Hwang & Eaton, 2006*a*; Poelma *et al.*, 2007; Tanaka & Eaton, 2010; Sahu *et al.*, 2014, 2016). Many of these studies were obtained for relatively large particles, for which significant loadings are obtained with limited number densities. Sub-Kolmogorov particles are harder to discriminate from tracers, and the velocimetry of the surrounding fluid is especially challenging in presence of clusters (Yang & Shy, 2005).

1.3 Motivation and Objectives

Due to the aforementioned difficulties in studying multiphase flows, there are still many aspects of their dynamics physicists and engineers find obscure and uncertain. The primary focus of the work in this thesis is to take an observational approach to the statistically relevant dynamics of multiphase turbulence. Through our laboratory observations, we have attempted to provide useful statistical analyses of two different types of particle-laden turbulence that might help guide future scientists to better model these flows and provide a springboard upon which experimentalists may launch their own investigations. Specifically, we studied: (i) homogeneous turbulence laden with small (sub-Kolmogorov) inertial particles; and (ii) falling plumes composed of microscopic solid particles settling in otherwise quiescent air. In (i) the complexity of the interphase coupling is driven by the turbulence in the carrier fluid, while in (ii) the dynamics are driven by the collective momentum of the particles falling by gravity and dispersing in the air. In the remainder of this dissertation:

- Chapter 2 briefly presents the utility of producing homogeneous, isotropic turbulence (HIT) in the lab; past lab setups used to investigate HIT; our design and a brief characterization of our facility.

- In Chapter 3, we describe our experiments in a dilute-particle regime and our observations.

- Chapter 4 describes our experiments on a denser particle-laden flow: settling particle plumes.

- Chapter 5 presents a final discussion of the analyses presented in the thesis and perspectives for the future.

Chapter 2

On Generating Homogeneous Turbulence

Experimentation neccesitates the ability to know and/or control the parameters of the experiment. With turbulent flows, any attempt to "control" them is daunting and difficult. The experiments contained in the next chapter of this thesis center around inertial particles in homogeneous turbulence with zero-mean flow. But why this particlular configuration of the turbulent flow? Why build a new apparatus ourselves from the ground up, instead of using the wonderful wind tunnel at Saint Anthony Falls Laboratory, where we conducted these experiments? We are interested in measuring the coupling between inertial particles and turbulence–the chaotic fluid fluctuating velocities, and the absence of a mean flow facilitates this in important ways. Turbulence without a mean flow allows tracking fluid tracers with stationary cameras for a longer period than if they were being advected along quickly by a strong mean flow. Previous studies (Voth *et al.*, 2002; Liberzon *et al.*, 2005; Bourgoin *et al.*, 2006) have used two facing counter-rotating impellers to generate von Karman flow–fully developed turbulence with universal traits within a region of negligible mean flow. In our multiphase studies, a lack of mean flow is important as the gravitational settling of particles in turbulence can be measured more accurately (Yang & Shy, 2005; Good *et al.*, 2014) as we can avoid the problem of trying to measure small fall speeds hidden by large convection velocities as one would obtain in a wind tunnel for example.

Homogeneous, isotropic turbulence (HIT) is an idealized version of turbulence first introduced by Taylor (1935), useful for numerical and experimental studies due to the fact that its features are well described by statistical theories (Bachelor, 1953; Kolmogorov, 1941; Davidson, 2015). In HIT, the average properties are independent of both position and direction. It is traditionally approximated by grid turbulence (Comte-Bellot & Corrsin, 1966; Mydlarski & Warhaft, 1996) in wind tunnels viewed from the frame of reference of the mean flow, but the streamwise decay of turbulent kinetic energy and the large mean flow are often undesirable features in certain experiments. These limitations

led to the development of turbulence boxes and stirred tanks. These have ranged from using oscillating grids (McKenna & McGillis, 2004; Blum *et al.*, 2010), the double-impeller design (Voth *et al.*, 2002; Worth & Nickels, 2011), to using loudspeakers or fans facing radially inward to a central point (Hwang & Eaton, 2004; de Jong *et al.*, 2009; Zimmermann *et al.*, 2010; Sahu *et al.*, 2014; Chang *et al.*, 2012; Dou *et al.*, 2016). Common to these designs however, is that the homogeneous regions produced are typically small, and importantly are smaller than the integral length scale of the turbulence–the scale of the largest eddies in the flow. Bellani & Variano (2014) commented that this is particularly detrimental when investigating particle-turbulence coupling where the dynamics are influenced by the history along the particle trajectory and whatever dynamics being measured could be due in part to the outer non-homogeneous region. Futhermore, such small regions of turbulence prevent the development of the larger scales of turbulence, which could have an important effect on the fluid-particle coupling themselves.

Variano *et al.* (2004) introduced and then qualified [(Variano & Cowen, 2008) a stirred tank design using randomly and independently controlled jets. This freedom allowed them to optimize the turbulence properties including achieving relatively high Reynolds numbers and minmizing the mean flow. Also importantly, the region of homogeneous turbulence created is much larger than the integral length scales. Bellani & Variano (2014) improved on their a single jet array design, by including two facing jet arrays, which produced relatively homogeneous and isotropic turbulence in water.

Our facility

Inspired by their successes, we designed and built a novel turbulence box, with the goal of creating a large volume of homogeneous air-turbulence with negligible mean flow, shear and strain. Our facility, depicted in figure 2.1, consists of a $2.4 \times 2 \times 1.1m^3$ chamber, with optical access provided by the acrylic lateral walls and ceiling. Two facing

jet arrays, able to slide within the chamber, consist of 256 total quasi-synthetic jets controlled by individual solenoid valves (Mac Valves 35 Series, opening time 6 ms). These are individually actuated by an IO system (cRio-9066, National Instruments) consisting of eight 32-channel output modules embedded in a 667 MHz dual core controller. The details of the apparatus, the turbulence generation and our the qualification of the turbulence are detailed in Carter *et al.* (2016). The unladen flow properties were investigated in detail by Carter & Coletti (2017, 2018).

Using the jet firing sequence proposed by Variano & Cowen (2008), we obtain approximately homogeneous turbulence with negligible mean flow and no shear over a central region of 0.5 by 0.4 by 0.7 m^3 in direction x, y and z, respectively (where x is aligned with the jet axis and z is vertical). This is substantially larger than the integral scale of the flow, allowing for the natural inter-scale energy transfer without major effects of the boundary conditions. Importantly, this also means that the particles, remembering the flow they experience through the history term in their transport equation (Maxey & Riley, 1983), are not affected by turbulence inhomogeneity. The lack of mean flow (especially small in the vertical direction, (see Carter *et al.*, 2016) is beneficial for the unbiased measurement of the particle settling velocity. The properties of the turbulence can be adjusted by varying the average jet firing time μ_{on}, the distance between both jet arrays, and by adding grids in front of the jets. In the present study, we keep the distance at 1.81 m and use a combination of firing times and grids that force turbulence with a Taylor microscale Reynolds number $Re_\lambda \approx 200 - 500$; the main properties for the unladen flow are reported in table 3.1. These may be altered by the presence of particles, although not dramatically in the considered range of particle types and loadings, as we will discuss in §5. The flow is anisotropic at all scales, with more intense velocity fluctuations in the x direction (Carter & Coletti, 2017). The fine-scale structure and topology display all signature features of homogeneous turbulence (Carter & Coletti, 2018).
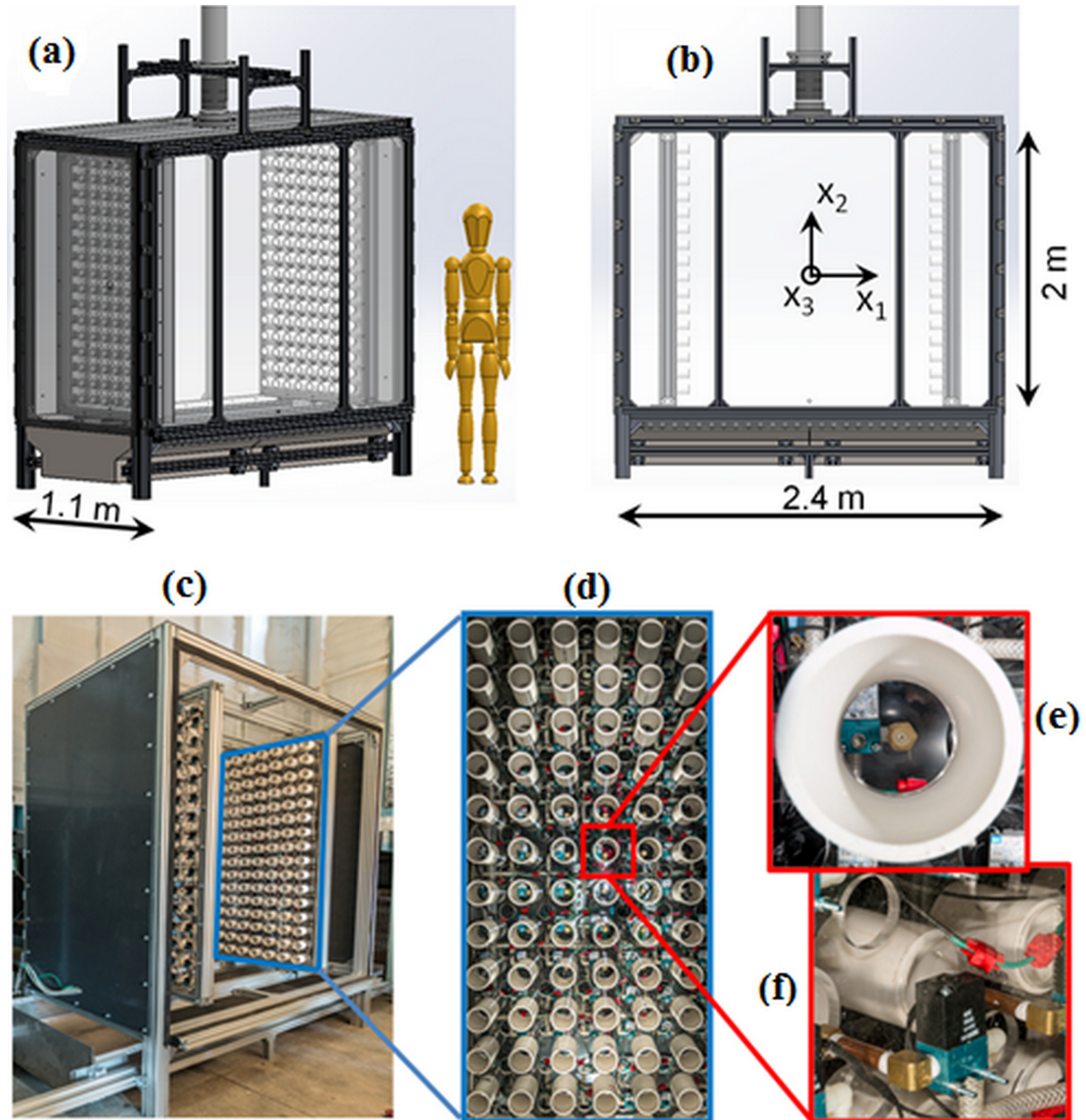
Figure 2.1: Isometric (a) and frontal (b) views of the turbulence chamber design. Photo of the built apparatus (c) with close-ups on one jet array (d) and an individual nozzle (e), and a rear view on an actuation valve (f). The chute visible in (a) and (b) is used to introduce settling particles to the turbulent flow field in the chamber.

Chapter 3

Dynamics of Dilute Turbulent Multiphase Flows

The dynamics of particles carried by turbulent fluid flows are rich with fascinating phenomena, even for the highly simplified case we consider: homogeneous incompressible turbulence laden with a dilute concentration of spherical, non-Brownian particles smaller than the Kolmogorov scale. Their behavior is especially complex when the particles are inertial without being ballistic, i.e. their aerodynamic response time τ_p is comparable to some relevant temporal scale of the flow. Several important effects observed in this regime are summarized below, making no claim of being exhaustive. For more details the reader is referred to recent reviews from Poelma & Ooms (2006), Balachandar & Eaton (2010), and Gustavsson & Mehlig (2016).

Inertial particles do not distribute homogeneously in turbulent flows, favoring regions of high strain and low vorticity (Maxey, 1987; Squires & Eaton, 1991). Such preferential concentration is consistent with early observations of particles accumulating outside the core of large-scale rollers and vortex rings in shear layers and jets (Lázaro & Lasheras, 1989; Longmire & Eaton, 1992; Ishima *et al.*, 1993), and has been attributed to the action of vortices centrifuging the particles outside of their core (Eaton & Fessler, 1994). While this tendency is noticeable even for weakly inertial particles, it is most intense when the Stokes number based on the Kolmogorov time scale ($St_\eta = \tau_p/\tau_\eta$) is close to unity (Wang & Maxey, 1993). Such a result is understood as a consequence of τ_η being the scale at which the highest vorticity occurs, and indeed particles with $St_\eta \approx 1$ were reported to form clusters scaling in Kolmogorov units (Kulick *et al.*, 1994; Aliseda *et al.*, 2002). This interpretation also implies that more inertial particles should cluster around eddies of larger turnover times, as was indeed shown by Yoshimoto & Goto (2007) who reported multi-scale preferential concentration from the dissipative to the inertial range. However, clustering of particles with St_η significantly larger than unity display different features compared to less inertial ones (Bec *et al.*, 2007), and mechanisms other than the centrifuging effect have been proposed (Goto & Vassilicos, 2008; Bragg & Collins, 2014; Ireland *et al.*, 2016*a*).

An important effect of the particle inertia is that, as they depart from the fluid streamlines, they may collide. The collision probability is a function of both the local concentration and the relative velocity (Sundaram & Collins, 1997; Wang *et al.*, 2000) the latter being potentially large as particles approach each other from different flow regions (Falkovich *et al.*, 2002; Wilkinson & Mehlig, 2005; Bewley *et al.*, 2013). When the particles are liquid droplets, collisions can lead to breakup or coalescence, with important implications for, e.g., atmospheric clouds (Shaw, 2003) and spray combustion (Jenny *et al.*, 2012). Additionally, in the presence of gravity, the drift of heavy particles crossing fluid trajectories decorrelates their motion from the turbulent fluctuations (Yudine, 1959; Csanady, 1963), reducing the particle velocity autocorrelation and dispersion coefficient (Reeks, 1977; Wells & Stock, 1983; Elghobashi & Truesdell, 1992; Squires & Eatons, 1991).

Beside concentration effects, a major consequence of turbulence in particle-laden flows is to alter the rate of gravitational settling. In their seminal work, Wang & Maxey (1993) confirmed by direct numerical simulations (DNS) the ideas put forward by Maxey (1987) using Gaussian flow simulations, and identified a mechanism by which inertial particles with $St_\eta = O(1)$ oversample downward regions of the turbulent eddies. This process, referred to as preferential sweeping or fast-tracking, can lead to a significant increase in mean fall speed compared to the expected terminal velocity in quiescent or laminar fluids, $W_0 = \tau_p g$ (g is the gravitational acceleration). Other mechanisms by which turbulence may modify the settling velocity have been proposed, as reviewed by Nielsen (1993) and Good *et al.* (2012). These include: vortex trapping, by which relatively light particles are trapped in vortical orbits (Tooby *et al.*, 1977); loitering, due to fast-falling particles spending more time in updrafts than in downdrafts (Nielsen, 1993; Kawanisi & Shiozaki, 2008); and non-linear drag increase, which may reduce the traveling speed of particles with significant Reynolds number based on their diameter and slip velocity (Mei *et al.*, 1991; Mei, 1994); all of these can lead to a decrease in

mean fall speed, as opposed to preferential sweeping. Additionally, local hydrodynamic interactions between particles were shown to increase fallspeed of bi-disperse suspensions (Wang *et al.*, 2007). While the conditions under which these mechanisms manifest are not well-known, enhanced settling due to preferential sweeping appears to be prevalent for sub-Kolmogorov particles with $St_\eta = O(1)$ (Yang & Lei, 1998; Aliseda *et al.*, 2002; Yang & Shy, 2003; Dejoan & Monchaux, 2013; Good *et al.*, 2014; Ireland *et al.*, 2016*b*; Rosa *et al.*, 2016; Baker *et al.*, 2017). Still, there is no consensus on which turbulence scales are most relevant for this process.

Though several works reported settling enhancement by turbulence under similar flow conditions, its extent remains an open question. In numerical simulations, the maximum increase of vertical velocity (which most authors found for $St_\eta \approx 1$) varies between studies, from about $0.1W_0$ to $0.9W_0$, or between $0.04u'$ and $0.16u'$, u' being the r.m.s. fluid velocity fluctuation (Wang & Maxey, 1993; Yang & Lei, 1998; Dejoan & Monchaux, 2013; Bec *et al.*, 2014*a*; Good *et al.*, 2014; Baker *et al.*, 2017). Laboratory observations have shown unsatisfactory quantitative agreement with simulations, and between each other. Aliseda *et al.* (2002) found strong increases in settling velocity of spray droplets in grid turbulence, as high as $1.6W_0$ or $0.26u'$ for their most dilute case. Later, Yang & Shy (2003, 2005) reported much weaker settling enhancement for solid particles in zero-mean-flow turbulence facilities. This led Bosse & Kleiser (2006), comparing their simulations to the results of both groups, to speculate on possible sources of errors in the measurements of Aliseda *et al.* (2002). Good *et al.* (2012) also found dramatic increases of spray droplet fall speed with turbulence, but this was amplified by mean flow effects (Good *et al.*, 2014). In a subsequent study, Good *et al.* (2014), using an extensively tested zero-mean-flow apparatus and high-resolution imaging, found levels of settling enhancement comparable with Aliseda *et al.* (2002). But they also showed that point-particle DNS at matching conditions yielding only qualitative agreement with the measurements. In a recent field study, Nemes *et al.* (2017) measured the fall speed

of compact snowflakes by high-speed imaging. They estimated the Stokes number of the observed snowflakes as $St_\eta \approx 0.1 - 0.4$, and concluded that the settling velocity in atmospheric turbulence was several times larger than the expected still-air fall speed.

An aspect of particle-laden turbulent flows in which our understanding is particularly incomplete is the backreaction of the dispersed phase on the fluid. There is substantial evidence that particles can alter the turbulent fluctuations, but it is still debated under which conditions these will be excited or inhibited (Balachandar & Eaton, 2010). Gore & Crowe (1991) argued that turbulence intensity is augmented/attenuated by particles larger/smaller than one tenth of the integral scale. For fully developed turbulence, this threshold concerns particles significantly larger than the Kolmogorov scale, which will likely modify the turbulence by locally distorting energetic eddies. Hetsroni (1989) proposed a criterion based on the particle Reynolds number $Re_p = d_p U_{slip}/\nu$ (where d_p is the particle diameter, ν is the kinematic viscosity, and U_{slip} is the slip velocity between both phases), predicting augmented and attenuated turbulence for $Re_p > 400$ and $Re_p < 100$, respectively. These thresholds are also relevant to relatively large particles. Elghobashi (1994) indicated that turbulence modification occurred when the volume fraction ϕ_v is higher than approximately 10^{-6}. In presence of preferential concentration, however, the local volume fraction can be much higher than the mean, enhancing collective effects within and around the clusters (Aliseda *et al.*, 2002). More recently, Huck *et al.* (2018) showed that by conditioning on the local volume fraction, they could identify three regimes affecting settling velocity: the sparsest dominated by the background flow, the intermediate concentrations suggesting preferential concentration effects, and the densest clusters triggering collective drag. Other parameters have been found to be consequential, including the Stokes number and the particle-to-fluid density ratio ρ_p/ρ_f, pointing to the multifaceted nature of the problem (Poelma *et al.*, 2007; Tanaka & Eaton, 2008). The question of turbulence augmentation versus attenuation is complicated by the fact that the particle-fluid energy transfer is scale-dependent:

several studies found that the presence of inertial particles increases the energy at small scales and decreases it at large scales (Elghobashi & Truesdell, 1993; Boivin *et al.*, 1998; Sundaram & Collins, 1999; Ferrante & Elghobashi, 2003; Poelma *et al.*, 2007). Gravitational settling also contributes to the turbulence modification, as the falling particles transfer their potential energy to the fluid (Yang & Shy, 2005; Hwang & Eaton, 2006*b*; Frankel *et al.*, 2016).

In this chapter we present the results of an extensive measurement campaign in which sub-Kolmogorov solid particles settle in homogeneous air turbulence created in a zero-mean-flow chamber. Planar imaging at various resolutions is used to probe both dispersed and continuous phases over a wide range of scales, providing insight into several of the outstanding questions discussed above.

3.1 The Experiment

3.1.1 Flow and Inertial Paricle Properties

All experiments were carried out in the turbulence box descirbed in chapter 2. In the present study, we kept the jet spacing at 1.81 m and used a combination of firing times and grids that forced turbulence with a Taylor microscale Reynolds number $Re_\lambda \approx 200 - 500$; the main properties for the unladen flow are reported in table 3.1. These may be altered by the presence of particles, although not dramatically in the considered range of particle types and loadings, as we will discuss in section 3.4.

The chamber ceiling is provided with a circular opening (15.2 cm in diameter) connected to a 3 m vertical chute, through which solid particles were introduced at a steady rate using an AccuRate dry material feeder. The feeding rate was adjusted to produce different volume fractions in the chamber. The particles interacted with the turbulence for at least 0.7 m before entering the field-of-view. At typical settling rates and depending on the particle types, this corresponds to between tens and hundreds of

Grids	μ_{on} [s]	u' [ms^{-1}]	u'_x/u'_z	L [mm]	η [mm]	τ_η [ms]	Re_λ
yes	.4	0.34	1.41	73	0.34	7.5	200
yes	10.	0.51	1.72	100	0.28	4.9	300
no	.2	0.59	1.41	90	0.27	4.8	300
no	.4	0.67	1.46	99	0.24	3.8	360
no	3.2	0.73	1.72	140	0.24	3.6	500
no	10.	0.76	1.67	146	0.24	3.6	500

Table 3.1: Unladen turbulence statistics for the configurations in this study. The r.m.s. velocity u' and the longitudinal integral scale L are based on a weighted average between the x and z directions. The Kolmogorov length scale $\eta = (\nu^3/\varepsilon)^{1/4}$ and time scale $\tau_\eta = (\nu/\varepsilon)^{1/2}$ are based on estimates of the dissipation rate ε from the 2nd order transverse structure functions. For further details Carter *et al.* (see 2016)

integral time scales of the turbulence-corroborating our observation that the particles spread throughout the chamber quickly upon entering it. We use several types of particles: soda-lime glass beads of various sizes (Mo-Sci Corp.), lycopodium spores (Flinn Scientific, Inc.), and glass bubbles (The 3M Company), all with a high degree of sphericity as verified by optical microscopy. The properties of the considered particle types are listed in table 3.2. The aerodynamic response time was iteratively calculated with the Schiller & Naumann correction (Clift *et al.*, 2005):

$$\tau_p = \frac{\rho_p d_p^2}{18\mu(1 + 0.15Re_{p,0}^{0.687})} \tag{3.1}$$

where μ is the air dynamic viscosity, ρ_p and d_p are the particle density and mean diameter, and $Re_{p,0} = d_p W_0/\nu$ is the particle Reynolds number based on the still-air settling velocity.

3.1.2　Measurement techniques

All measurements were performed along the $x - z$ symmetry plane, using the same hardware as in Carter *et al.* (2016) and Carter & Coletti (2017, 2018). The air flow was

$d_p[\mu\text{m}]$	material	ρ_p [kg/cm^3]	τ_p [ms]	$Re_{p,0}$
91 ± 11	glass bubbles	100	1.7	0.10
30 ± 2	lycopodium	1200	3.1	0.06
32 ± 7	glass	2500	7.4	0.15
52 ± 6.1	glass	2500	17	0.56
96 ± 11	glass	2500	47	3.26

Table 3.2: Particle properties. The diameters d_p are listed in mean $\pm$ standard deviation.

seeded with $1-2$ μm DEHS (di-ethyl-hexyl-sebacate) droplets, which are small enough to faithfully trace the air motion without altering the particle transport. The imaging system consisted of a dual-head Nd:YAG laser (532 nm wavelength, 200 mJ/pulse) synchronized with a 4 Megapixel, 12-bit CCD camera. To capture the wide range of spatial scales, we performed measurements using Nikon lenses with focal lengths of 50, 105, and 200 mm, yielding a range of fields of view (FOV) and resolutions reported in table 3.3. The laser pulse separation, chosen as a compromise to capture the in-plane motion of both flow tracers and inertial particles, ranged between 110μs (to image the heavier particles in the smaller FOV and stronger turbulence) and 850 μs (for the lighter particles in the larger FOV in weaker turbulence). For all measurements the typical displacement of both tracers and inertial particles was approximately 5 pixels. For the inertial particles this corresponds to 1 visual particle diameter on average. The sampling frequency was 7.25 Hz, which provided approximately uncorrelated realizations (given the typical large-eddy turnover time between 0.1 and 0.2 s). For most experiments, 2000 image pairs were recorded. For the cases with highest loading, the finite supply of particles in the screw-feeder limited the recordings to $1000 - 1500$ image pairs. Because those cases also had the highest number of particles per image (and do not allow accurate fluid measurements), the statistical convergence of the reported quantities was not significantly altered.

The two-phase flow images were used to perform simultaneous PIV on the tracers and PTV on the inertial particles. After subtracting a pixel-wise minimum intensity

background from each image, both phases were separated via an algorithm inspired by Khalitov & Longmire (2002). We set all pixels below a threshold intensity to zero, which we choose based on a visual inspection of each individual case. Contiguous groups of non-zero pixels were identified and labeled as either tracers or inertial particles contingent on their position in a size-intensity map. Pixels belonging to inertial particles were subtracted and substituted with a Gaussian noise of the same mean and standard deviation as the corresponding image. The resulting tracer-only images were then processed via a cross-correlation PIV algorithm with iterative window offset and deformation, applying one refinement step and 50% overlap (Nemes *et al.*, 2015). A Gaussian fitting function was used to determine sub-pixel displacements. Tests on synthetic images confirmed that the cross-correlation algorithm accurately predicts tracer displacements within ± 0.1 pixels when their images are 2–3 pixels in size, representative of our small-FOV recordings. For the large and intermediate FOV, moderate peak-locking is present in the distribution of particle displacements. This only marginally affects the fluid statistics in the present zero-mean-flow configuration, since the entire range of pixel displacement is associated with the turbulent motion (Carter *et al.*, 2016). PIV vector validation is based on signal-to-noise ratio and deviation from the median of the neighboring vectors (Westerweel & Scarano, 2005). Non-valid vector percentages varied between experiments depending on camera resolution and inertial particle volume fraction. While most runs had fewer than 8% of vectors rejected, the cases with higher particle concentration had 15–18% rejected fluid velocity vectors. This is due to the background noise from light scattered by the ensemble of the inertial particles, rather than to the removal of individual particle images from local interrogation windows. Indeed for the present cases, no statistical correlation was found between the location of non-valid vectors and the inertial particle position, except for the most highly concentrated cases where we do not attempt to extract fluid information. The dominant source of uncertainty on the flow statistics was the finite sample size, yielding typical uncertainties of 3% for mean velocity measurements and

Focal length (mm)	Field of view (cm^2)	Field of view ($L_{L,1}^2$)	Resolution (pix/mm)	PIV vector spacing (mm)	PIV vector spacing (η)
50	30^2	2^2 − 3.3^2	6	N/A	N/A
105	12.5^2	0.8^2 − 1.6^2	15	0.88 − 1.77	3.3 − 7.4
200	4.5^2	0.3^2 − 0.6^2	40	0.33 − 0.61	1.1 − 2.6

Table 3.3: Imaging parameters obtained with the CCD camera (2048 by 2048 pixels, 7.4 μm pixel size) when mounting the different lenses. The large FOV with the 50 mm lens is not used for PIV.

5% for root mean square (r.m.s.) velocity fluctuations (Bendat & Piersol, 2011).

The objects labeled as inertial particles were moved to a blank image and tracked via an in-house PTV algorithm. This is based on the cross-correlation approach (Ohmi & Li, 2000; Hassan *et al.*, 1992), although our version uses the full 12-bit pixel intensity information rather than the binarized image. The algorithm searches for a matching object within a specified radius around each particle centroid, maximizing the correlation coefficient between the image pairs. It performs well even with multiple neighboring particles, since the local distribution pattern remains similar in the image pair. Mild peak-locking is present in the large-FOV recordings of the smaller particles; however, as in the PIV of the tracers, the zero-mean-flow configuration limits the impact on the measured statistics. The process of phase separation is illustrated in figure 3.1, where a sample image is shown along with the resulting fluctuating velocity of flow tracers and inertial particles from PIV and PTV, respectively.

An advantage of the cross-correlation PTV approach is that its accuracy is weakly affected by the uncertainty in locating the object centroid. The latter will, however, affect the measurement of the particle spatial distribution, which is of interest in our study. We used different methods for locating the centroid, depending on the imaging conditions. For the larger FOV, the inertial particles cover typically 3 − 4 non-saturated pixels and a standard three-point Gaussian fit was appropriate. For the intermediate and small FOV, the particle images were larger and sometimes saturated. In these cases, we
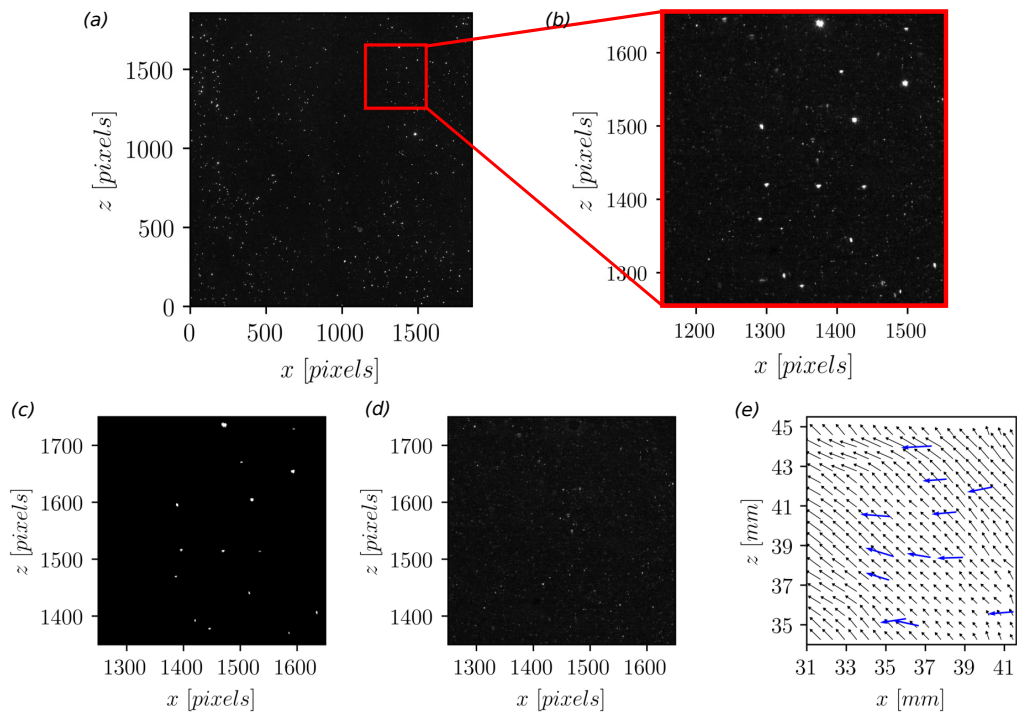
Figure 3.1: Image processing procedure for PIV/PTV measurements of tracer and particle motion: (a) raw image, (b) inset of raw image, (c) particle-only image, (d) tracer-only image, (e) resulting fluctuating fluid and particle velocity vectors.

used a least-squares Gaussian fit: for each object, a circular particle image of equivalent size is generated, following a Gaussian spatial distribution centered on the center-of-mass of the original object (the weights being the pixel intensities). The position of the circular particle was then fitted to the original particle through a two-dimensional least-squares regression, yielding the sub-pixel centroid. The accuracy of both the three-point and least-squares methods has been tested on synthetic particle images with and without saturation. The least-squares method is more computationally expensive but more accurate, with an average error of 0.12 pixels in locating the centroid of saturated particles, against 0.45 pixels for the three-point fit. Importantly, the spatial distribution of particle count presented significant inhomogeneities only over the largest FOV, as shown in figure 3.2 for a representative case, which is due to the somewhat uneven laser illumination at those scales. This allowed us to compute particle statistics via space-time ensemble-averages over the full window, without the need of compensating for spatial gradients (Sumbekova *et al.*, 2017).

Using our particle identification methods, we also are able to estimate the volume fraction ϕ_v, by counting the number of particles in the field of view and comparing their total volume with the illuminated volume. Even at the higher loading considered, the average inter-particle distance was at least $\sim$1 mm, which is larger than the particle image. Due to clustering, particles may be found much closer to each other, preventing their individual identification. However, intense clustering usually pertains to a limited fraction of the particle set (Baker *et al.*, 2017), and thus the number of undetected ones is expected to be relatively small. Yang & Shy (2005) and recently Sahu *et al.* (2014, 2016) carried out experiments in similar conditions and used the same approach to estimate ϕ_v. This method has proven robust also in our recent study of a particle-laden channel flow, in which we imaged 50 μm glass beads at $\phi_v = O(10^{-5})$ with a similar PIV system (Coletti *et al.*, 2016; Nemes *et al.*, 2016). In that case the imaging-based volume fraction agreed to within 12–15% the value obtained from the amount of particles accumulated
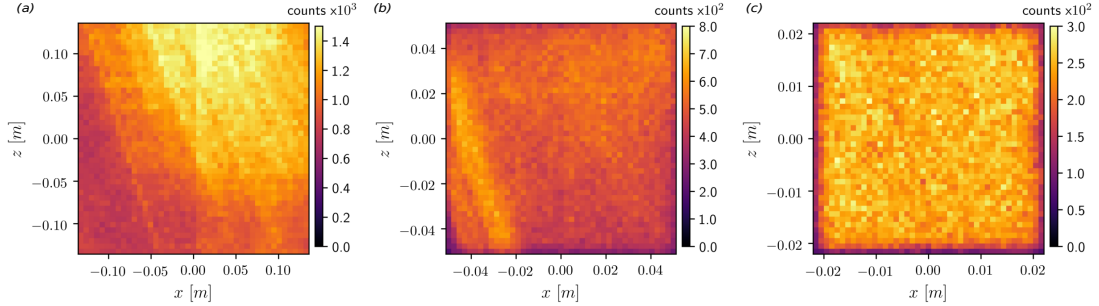
Figure 3.2: Particle counts for example fields of view.

in the exit plenum during a given run time.

3.1.3 Voronoï tessellation and cluster identification

To analyze the spatial distribution and concentration of the inertial particles, and in particular the properties of discrete clusters, we made use of the Voronoï diagram method (Monchaux *et al.*, 2010). This approach divides the domain (in this case, the two-dimensional image) into a tessellation of cells associated to individual particles, each cell containing the set of points closer to that particle than to any other. The inverse of the area A of each cell equals the local particle concentration, $C = 1/A$. The method has been used to analyze particle-laden turbulent flows in both experimental (Obligado *et al.*, 2014; Rabencov & van Hout, 2015; Sumbekova *et al.*, 2017) and numerical studies (Tagawa *et al.*, 2012; Kidanemariam *et al.*, 2013; Dejoan & Monchaux, 2013; Zamansky *et al.*, 2016; Frankel *et al.*, 2016; Baker *et al.*, 2017; Monchaux & Dejoan, 2017). Figure 3.3a shows the Voronoï tessellation for one small-FOV realization, and a representative probability density function (PDF) of cell areas normalized by the mean value $\langle A \rangle$ is plotted in figure 3.3b. (Here and in the following, angle brackets denote ensemble-average.) As typical for clustered particle fields, the observed PDF is much wider than that of a random Poisson process, which follows a Γ distribution (Ferenc & Néda, 2007).

Figure 3.3c shows the centered and normalized PDFs of the logarithm of the Voronoï cell areas for all our experiments, indicating a reasonable collapse that emphasizes their quasi-lognormality. This behavior has been exploited to characterize the particle distribution by a single parameter, the standard deviation σ_A (Monchaux *et al.*, 2010).

The value A^*, below which the probability of finding sub-average cell areas is higher than in a Poisson process, is usually taken as the threshold for particles to be considered clustered (Monchaux *et al.* 2010, Rabencov & van Hout 2015, Sumbekova *et al.* 2017, among others). Individual clusters were then defined as connected groups of such particles, as shown in figure 3.3a. To avoid spurious edge effects, we applied the additional constraint that the area of all neighboring cells are also smaller than A^* (a condition first introduced by Zamansky *et al.* (2016). Figure 3.3d shows the PDFs of cluster areas A_C for a representative case, obtained with and without this latter condition. Such a condition separates objects connected by only one Voronoi cell. The edge effect produces ripples in the distribution without the neighbor cell condition, indicating that certain cluster sizes are unlikely to occur, possibly due to the coagulation of neighboring connected objects; the application of the neighboring cell condition removes this artifact. This allowed us to isolate very small clusters and to separate artificially large ones; hence the apparent shift in the area PDF.

Following Baker *et al.* (2017), we use the Voronoï diagram method to identify individual clusters, focusing on those sufficiently large to exhibit a scale-invariant structure. Figure 3.3e displays, for the same case as in figure 3.3d, the scatter plot of cluster perimeters (P_C) versus the square root of their areas ($A_C^{1/2}$). (We refer to 'cluster perimeter' and 'cluster area', although these are strictly properties of the connected set of Voronoï cells associated to the particles in each cluster, rather than to the cluster itself). For small clusters, the data points follow a power law with exponent ~ 1 as expected for regular two-dimensional objects, while for larger ones the exponent is approximately 1.4, indicating a convoluted structure of the cluster borders. This trend, common to all

our experiments, was observed in several previous studies (e.g., Monchaux *et al.*, 2010; Rabencov & van Hout, 2015; Baker *et al.*, 2017) using Voronoï tessellation, and earlier Aliseda *et al.* (2002) using box-counting), and is consistent with the view of inertial particle clusters as fractal sets (Bec, 2003; Bec *et al.*, 2007; Calzavarini *et al.*, 2008), although it must be remarked that this latter feature was shown to be associated to the dissipative scales. The minimum size for the emergence of fractal clustering is difficult to identify precisely in figure 3.3e; however, as shown by Baker *et al.* (2017), this also corresponds to the emergence of self-similarity of the cluster sizes, as indicated by the power-law decay in their size distribution. This threshold can be located with more confidence in figure 3.3d (dashed line); it is taken as the condition for a cluster to be "coherent", i.e. associated to the coherent motions in the underlying turbulent field rather than by accidental particle proximity (Baker *et al.*, 2017).

3.1.4 Parameter space

Table 3.4 reports the main physical parameters and imaging resolution for all experimental runs, 57 in total. Not all cases are used for all types of analysis: for example, the glass bubbles are very light and do not allow sufficiently accurate measurements of the settling velocity, while the 100 μm glass beads do not disperse homogeneously enough to perform clustering analysis. The importance of particle weight is characterized by the settling parameter $Sv_\eta = W_0/u_\eta$, where $u_\eta = \eta/\tau_\eta$ is the Kolmogorov velocity. Since both small-scale and large-scale eddies are consequential for the settling process, a definition based on the r.m.s. fluid velocity fluctuation, $Sv_L = W_0/u'$, is also relevant (Good *et al.*, 2014). The Froude number $Fr = St_\eta/Sv_\eta$ is also often used in literature, and is reported in table 4 for completeness. From a comparison with previous studies, we expect the turbulence to induce significant clustering and settling modification, and the particles to possibly modify the turbulence at the higher volume fractions. We remark that, as in any laboratory study with a fixed gravitational acceleration, varying only one
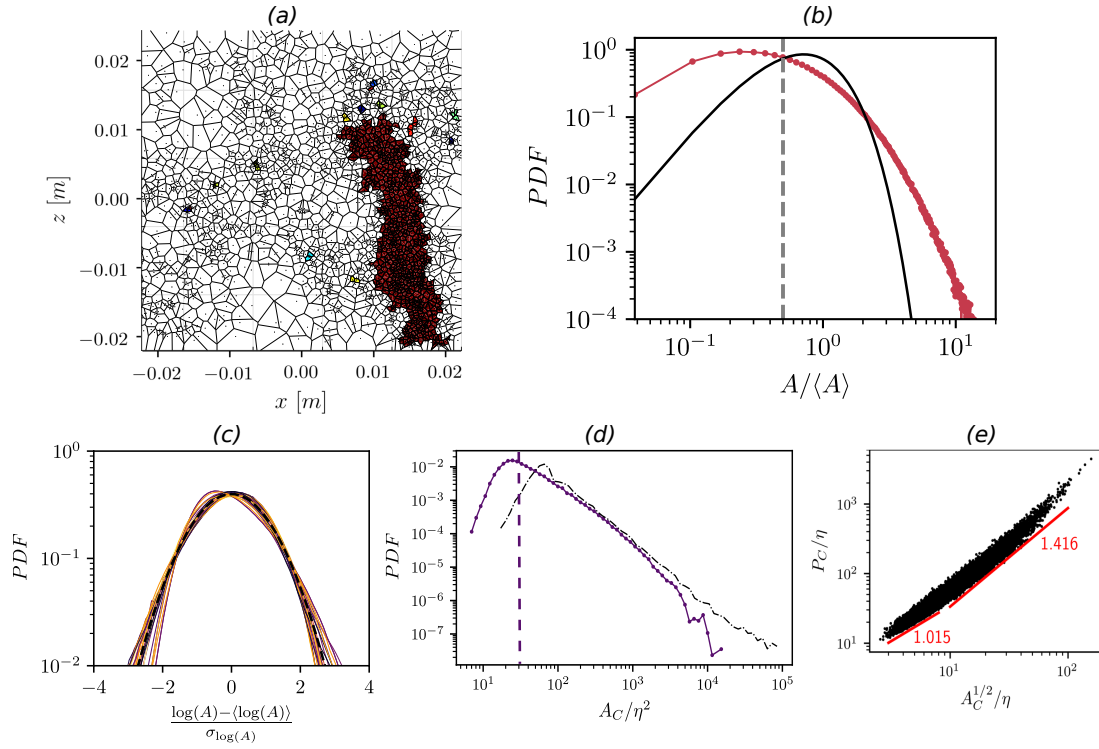
Figure 3.3: (a) Example Voronoï tessellation with connected sets of Voronoï cells below the area threshold colored. (b) Example Voronoï area PDF shows clear departure from random Poisson distribution indicating the presence of clusters and voids for a case with $St_\eta = 3.2$. (c) All PDFs of $\log(A)$, centered at the mean and normalized by the standard deviation. The black dotted line shows a normal distribution with variance $= 1$. (d) PDF of a sample case, with (purple circles) and without (black dashes) the neighboring cell condition. (e) Scatter plot of cluster perimeter and square root of its area (same case as in (d)).

parameter at a time is not feasible. For example, increasing St_η by using heavier particles leads to higher Sv_η, unless Re_λ is also adjusted. Likewise, varying ϕ_v may modify the turbulence properties, and therefore the effective values of the other parameters. Therefore, throughout the paper we will often show the simultaneous dependence of the observables with multiple parameters.

Case	material	Re_λ	d_p/η	St_η	Sv_η	Sv_L	Fr	ϕ_v	ϕ_m
1	glass	500	0.52	20.8	5.6	0.59	3.7	5.5e-5	1.0e-1
2	glass	500	0.43	14.7	6.5	0.66	2.3	2.6e-6	5.3e-3
3	glass	300	0.43	14.0	6.8	0.77	2.1	3.4e-5	6.9e-2
4	glass	500	0.42	14.0	6.7	0.66	2.1	2.5e-6	5.2e-3
5	glass	500	0.40	12.4	7.1	0.63	1.8	1.5e-5	3.1e-2
6	glass	500	0.40	12.4	7.1	0.63	1.8	1.6e-5	3.7e-2
7	glass	300	0.40	12.5	7.1	0.90	1.8	1.6e-6	3.4e-3
8	glass	300	0.39	12.0	7.2	0.86	1.7	1.7e-6	3.8e-3
9	glass	300	0.35	9.8	8.0	0.77	1.2	1.7e-5	3.5e-2
10	glass	500	0.26	6.5	2.3	0.24	2.9	6.5e-6	1.3e-2
11	glass	500	0.26	6.6	2.3	0.23	2.7	3.2e-7	6.5e-4
12	glass	400	0.26	6.4	2.3	0.26	2.8	2.4e-7	4.9e-4
13	glass	500	0.24	5.8	2.3	0.23	2.5	1.2e-6	2.4e-3
14	glass	500	0.24	5.4	2.4	0.24	2.2	9.5e-7	1.9e-3
15	glass	500	0.23	5.2	2.5	0.23	2.1	1.4e-6	2.8e-3
16	glass	500	0.23	5.1	2.6	0.25	2.0	1.4e-7	2.9e-4
17	glass	300	0.23	5.1	2.5	0.30	2.0	3.6e-7	7.4e-4
18	glass	300	0.23	4.9	2.6	0.31	1.9	2.2e-5	4.6e-2
19	glass	500	0.22	4.6	2.6	0.23	1.8	2.3e-6	4.8e-3

Table 3.4 – continued

Case	material	Re_λ	d_p/η	St_η	Sv_η	Sv_L	Fr	ϕ_v	ϕ_m
20	glass	500	0.22	4.6	2.6	0.23	1.8	6.6e-7	1.3e-3
21	glass	500	0.22	4.6	2.6	0.23	1.8	2.8e-5	5.7e-2
22	glass	500	0.21	4.4	2.7	0.26	1.7	3.1e-6	6.3e-3
23	glass	300	0.21	4.2	2.7	0.34	1.5	2.3e-6	4.8e-3
24	glass	300	0.21	4.6	2.6	0.28	1.7	1.8e-6	3.8e-3
25	glass	500	0.20	4.1	2.7	0.30	1.5	6.6e-8	1.4e-4
26	glass	300	0.20	4.1	2.8	0.34	1.5	1.0e-6	2.0e-3
27	glass	300	0.19	3.6	2.9	0.29	1.2	6.5e-6	1.3e-2
28	glass	300	0.19	3.6	2.9	0.29	1.2	3.8e-6	7.8e-3
29	glass	300	0.19	3.2	3.3	0.38	1.0	2.3e-7	4.7e-4
30	glass	300	0.18	3.3	3.0	0.39	1.0	1.6e-7	3.2e-4
31	glass	500	0.15	2.8	1.0	0.10	2.9	4.8e-7	9.8e-4
32	glass	500	0.15	3.2	0.90	0.10	3.5	3.0e-7	6.2e-4
33	glass	500	0.15	2.9	1.0	0.10	3.0	4.4e-8	9.0e-5
34	glass	300	0.14	2.4	1.1	0.13	2.2	8.0e-8	1.6e-4
35	glass	500	0.13	2.4	1.0	0.10	2.3	8.0e-8	1.6e-4
36	glass	300	0.13	2.2	1.1	0.13	2.0	4.2e-7	8.5e-4
37	glass	500	0.12	2.0	1.1	0.10	1.8	5.8e-7	1.2e-3
38	glass	500	0.12	2.0	1.1	0.10	1.8	2.7e-8	5.0e-5
39	glass	500	0.12	2.0	1.1	0.10	1.8	2.6e-6	5.3e-3
40	glass	500	0.12	2.0	1.1	0.10	1.8	1.2e-7	2.4e-4
41	glass	300	0.12	2.0	1.1	0.13	1.7	6.3e-7	1.3e-3
42	glass	300	0.12	1.8	1.2	0.14	1.6	8.4e-7	1.7e-3
43	glass	300	0.11	1.6	1.3	0.12	1.2	7.8e-7	1.6e-3

Table 3.4 – continued

Case	material	Re_λ	d_p/η	St_η	Sv_η	Sv_L	Fr	ϕ_v	ϕ_m
44	glass	300	0.11	1.7	1.2	0.14	1.4	8.8e-7	1.8e-3
45	glass	300	0.11	1.7	1.2	0.15	1.4	1.4e-7	2.8e-4
46	glass	300	0.11	1.6	1.3	0.12	1.2	2.1e-6	4.4e-3
47	glass	300	0.11	1.8	1.2	0.14	1.5	6.5e-8	1.3e-4
48	glass	300	0.11	1.6	1.3	0.13	1.2	6.7e-8	1.4e-4
49	glass	300	0.11	1.7	1.2	0.14	1.4	1.3e-7	2.7e-4
50	glass	200	0.09	1.1	1.6	0.22	0.73	1.2e-7	2.4e-4
51	lycopodium	500	0.12	0.80	0.46	0.04	1.8	5.4e-7	5.3e-4
52	lycopodium	500	0.12	0.80	0.46	0.04	1.8	8.6e-8	8.0e-5
53	lycopodium	300	0.12	0.75	0.48	0.06	1.6	1.6e-7	5.0e-4
54	lycopodium	300	0.11	0.63	0.51	0.05	1.2	9.4e-6	9.2e-3
55	lycopodium	300	0.11	0.63	0.51	0.05	1.2	6.0e-7	5.9e-4
56	lycopodium	300	0.11	0.63	0.51	0.05	1.2	1.9e-7	1.8e-4
57	glass bubbles	300	0.34	0.37	0.30	0.03	1.2	3.4e-5	2.7e-3

Table 3.4: Main experimental parameters for all considered cases, ordered in decreasing particle Stokers number St_η.

3.2 Particle spatial distribution

3.2.1 Clustering analysis

In this section we explore the spatial structure of the inertial particle fields and the length scales over which clustering occurs. In the literature this has been characterized by two main tools: the radial distribution function (RDF) and, more recently, Voronoï tessellation. Both methods provide different and complementary information—we apply them both for a comprehensive description.

The RDF describes the scale-by-scale concentration in the space surrounding a generic particle, compared to a uniform distribution. For 2D distributions such as those obtained by planar imaging, this is defined as:

$$g(r) = \frac{N_r/A_r}{N/A_{tot}} \tag{3.2}$$

where N_r represents the number of particles within an annulus of area A_r, while N is the total number of particles within the planar domain of area A_{tot}. In presence of clustering, the RDF is expected to increase for decreasing r, and the range over which it remains greater than unity indicates the length scale over which clustering occurs (e.g., Sundaram & Collins, 1997; Reade & Collins, 2000; Wood *et al.*, 2005; Saw *et al.*, 2008; de Jong *et al.*, 2010; Ireland *et al.*, 2016*a,b*). We compute RDFs by binning particle pairs based on their separation distance. To avoid projection biases at separations below the illuminated volume thickness (Holtzer & Collins, 2002), we only calculate $g(r)$ for $r > 1.5$ mm. As noted by de Jong *et al.* (2010), imaging-based RDF measurements are sensitive to the size and shape of the observation region, and some sort of edge-correction strategy is needed for particles near the image boundaries. One can omit statistics for radial annuli that cross the image boundary, but this approach has two shortcomings: the maximum separation becomes limited to the radius of the domain-inscribed circle; and the number of particle pairs per unit area used to calculate the RDF decreases as the separation increases. Both effects combine to thwart the reliable assessment of large-scale clustering. Indeed, past RDF measurements at distances $O(L)$ in flows with wide scale separation were obtained using single-point probes and invoking Taylor's hypothesis (Saw *et al.*, 2008, 2012; Bateson & Aliseda, 2012). Here, following de Jong *et al.* (2010), we leverage the spatial homogeneity of our fields and apply a periodic-domain correction: the particle field is mirrored across the image boundaries, so that the same number of radial annuli can be used for each particle location, yielding

a maximum separation equal to the full size of the FOV. Although this assumption introduces unphysical correlations between particles near the reflected boundaries, numerical experiments using DNS showed the associated error to be small (Salazar *et al.*, 2008).

Due to the large range of scale separation ($L/\eta \sim O(10^3)$, $L/d_p \sim O(10^4 - 10^5)$) it is not feasible to simultaneously resolve all scales at play, and thus the small-FOV and large-FOV imaging will suffer from large-scale and small-scale cutoffs, respectively. Comparing the different FOVs, however, provides quantitative information over a wide range of scales. Figure 3.4a) shows examples from the small-FOV measurements. At small separations, several authors have found satisfactory fit to the data using a power law, which indicates a self-similar spatial distribution (Chun *et al.*, 2005; Salazar *et al.*, 2008; Zaichik & Alipchenkov, 2009; Ireland *et al.*, 2016*a,b*):

$$g(r/\eta) = c_0(r/\eta)^{-c_1} \qquad (3.3)$$

where c_0 and c_1 are coefficients dependent on St_η (and, in presence of gravity, Sv_η). While theoretical arguments consistent with this formulation strictly apply for dissipative separations ($r/\eta < 1$,Chun *et al.* (2005), Saw *et al.* (2008) argued that the power-law form should continue into the correlation scale of the velocity gradients ($r/\eta = O(10)$). In figure 3.4a) we see indeed that RDFs closely follow a power-law decay up to $r/\eta \approx 40$ for St_η close to unity. The departure from the power law at larger separations indicate the particle set is not self-similar at those scales (Bragg *et al.*, 2015). We evaluate the coefficients c_0 and c_1 by least-square fit over the range $10 < r/\eta < 30$, and plot them in figure 5b and 5c as a function of St_η. The error bars for the coefficients come from the covariance matrix of the fit. The results, which are only weakly sensitive to varying the fit upper bound between $r/\eta = 20$ and 40, display the higher values in the approximate range $1.5 < St_\eta < 4$. This confirms that particles with Stokes number $O(1)$ display the stronger degree of clustering over the near-dissipative range. However, the most intense clustering occurs for $St_\eta > 1$, possibly because of the significant effect of

gravitational settling as discussed below. The trend and values are in fair quantitative agreement with the DNS of Ireland *et al.* (2016*b*) in similar conditions. The c_1 coefficient is related to the correlation dimension used in dynamical system theory (Bec *et al.*, 2008), $D_2 = n - c_1$, where the number of spatial dimensions is $n = 2$ for our planar realizations. Figure 5d plots D_2 for the different cases, showing trends and values consistent with the channel flow experiments by Fessler *et al.* (1994) and the grid turbulence experiments by Monchaux *et al.* (2010, 2012). For increasing particle inertia, one expects a loss of spatial correlation as the particle response time grows beyond the fine turbulent scales. Although the present range does not extend to very large St_η, we note that the return to a homogeneous distribution appears slow. Recent numerical studies compared settling and non-settling conditions, and concluded that gravity hinders clustering for $St_\eta < 1$ but enhances it for $St_\eta > 1$, resulting in significant clustering over a wide range of Stokes numbers (Bec *et al.*, 2014*b*; Gustavsson *et al.*, 2014; Ireland *et al.*, 2016*b*; Matsude *et al.*, 2017; Baker *et al.*, 2017). Ireland *et al.* (2016*b*) attributed this behavior to the competing effects of the particle path history and preferential flow sampling. Sahu *et al.* (2016) measured RDFs for spray droplets and also noticed an increasing tendency to cluster for increasing St_η (although their range was very close to unity).

The large-FOV measurements allow us to probe the spatial distribution over much greater scales. Figure 3.5a clearly indicates that considerable clustering occurs over lengths $O(L)$. For a quantitative assessment, we consider the original power-law model proposed by Reade & Collins (2000):

$$g(r/\eta) - 1 = c_0^*(r/\eta)^{-c_1^*}e^{-c_2^* r/\eta} \tag{3.4}$$

which, unlike eq. 3.3, does recover the return to unity at large separations. The excellent fit to the data over the entire window confirms the observation made by Reade & Collins (2000), that the RDFs of preferentially concentrated particles have a power-law decay
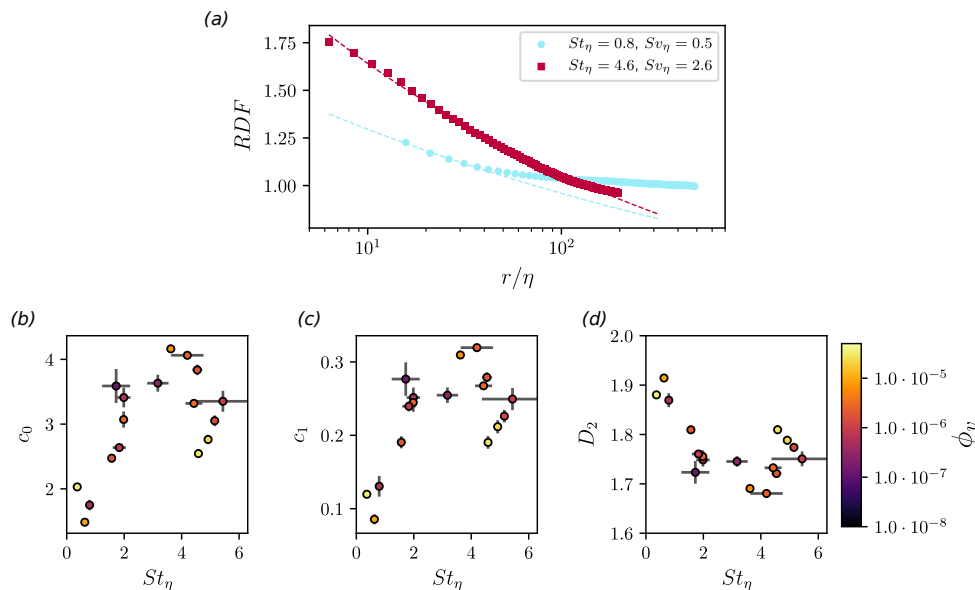
Figure 3.4: (a) Example RDFs where symbols represent the calculated RDFs and dashed lines their fits according to equation 3.3. (b) and (c) show the fitted values versus St_η, and (d) shows the value of the correlation dimension.

at small scales and an exponential tail at large scales. Figure 3.5b,c,d display the least-square-fit coefficients as a function of St_η. The c_2^* coefficient decreases as St_η increases, implying a greater spatial extent of clustering for the more inertial particles. This may be due to the more inertial particles responding to larger time scales of the turbulence, and to the influence of gravitational settling as mentioned above. The length scale of the large-scale clustering can be estimated from the exponential decay as η/c_2, which for $St_\eta > 1$ is about $300\eta - 400\eta$, close to the integral scale of the turbulence. Taken together, these results confirm that clustering can extend over larger scales for heavier particles. This is in agreement with the conceptual picture of Goto & Vassilicos (2006) and Yoshimoto & Goto (2007) and the simulations of Bec *et al.* (2010) and Ireland *et al.* (2016*a*,*b*), which showed that particles of $St_\eta > 1$ respond to eddies in the inertial range. However, as we will reiterate in the next sub-section, the present results indicate that some level of clustering may extend even beyond, approaching the integral scales.
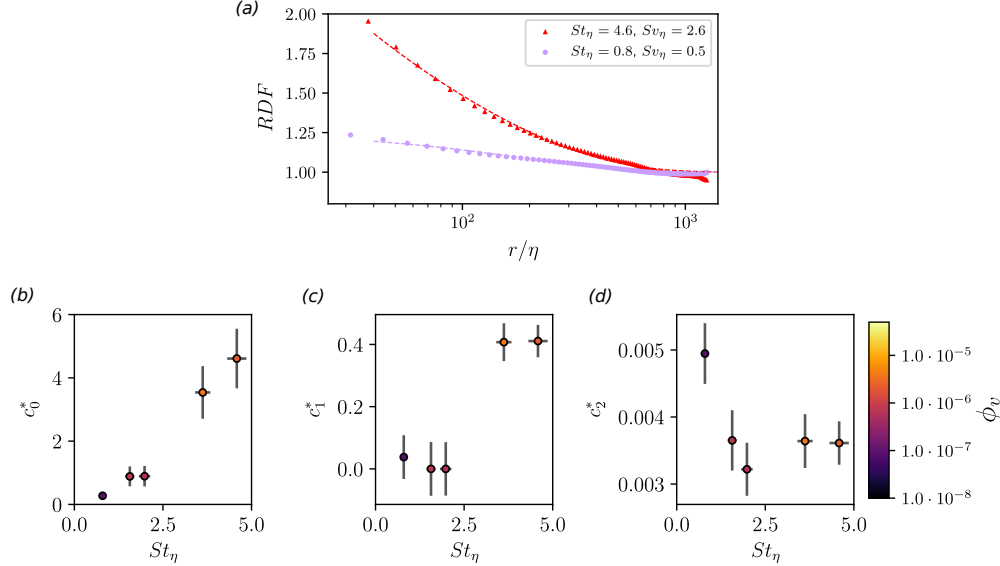
Figure 3.5: (a) Example RDFs where symbols represent the calculated RDFs and dashed lines their fits according to equation 3.4. (b), (c) and (d) show the fitted coefficients versus St_η.

The degree of clustering can also be evaluated from the Voronoï diagrams. We remark that the type of information provided by this method is somewhat different than the RDF. The latter is strictly a two-particle quantity, while the shape and size of the Voronoi cells result from the mutual position of multiple particles. Therefore, we looked for an insight complementary to our RDF results. In figure 3.6a we plot the standard deviation of the Voronoï cell areas σ_A as a function of the Stokes number, normalizing it by the expected value for particles distributed according to a random Poisson process, $\sigma_{RPP} \approx 0.53$ (Monchaux *et al.*, 2010). As a general trend, clustering is most pronounced for particles of $St_\eta \approx 1$, in agreement with previous studies (Monchaux *et al.*, 2010; Tagawa *et al.*, 2012; Dejoan & Monchaux, 2013; Monchaux & Dejoan, 2017). However, the significant scatter suggests that other parameters may also play a role. Indeed, in their grid turbulence study, Sumbekova *et al.* (2017) found that σ_A was strongly dependent on Re_λ, moderately on ϕ_v, and negligibly on St_η. While

the considerable degree of polydispersity in their experiments may have influenced such conclusion, their results convincingly indicated that clustering is affected by a range of turbulent scales, whose breadth is controlled by Re_λ. Moreover, as pointed out by Baker *et al.* (2017), σ_A is not only a function of the concentration of the clustered particles, but also of the size and distribution of the voids, and the latter are strongly influenced by the inertial and integral scales of the turbulence (Yoshimoto & Goto, 2007).

The decrease in σ_A for $St_\eta > 1$ is mild. Since increasing St_η also implies increasing Sv_η, this again suggests that, in this range, gravitational settling may enhance clustering. This idea is supported by figure 3.6b, showing the fraction of particles belonging to coherent clusters (according to the definition in §2.3) plotted versus σ_A. A clear correlation is visible, indicating that the number of clustered particles, N_c, is is similarly affected by the physical parameters. The values are possibly underestimated because particles in highly concentrated regions are more likely to be overshadowed by neighboring particles and go undetected. Still, the results are in fair agreement with the DNS of Baker *et al.* (2017), where less than 3% of the particles with $St_\eta < 1$ belonged to coherent clusters, with the percentage increasing up to 14% for $St_\eta = O(10)$. Therefore, the more inertial (and faster falling) particles are more likely to belong to clusters; or, equivalently, they tend to form clusters that are more numerous, larger, or denser. The question of the cluster size and the concentration within them is addressed in the following section.

3.2.2 Individual clusters

The multi-scale nature of the clustering process is reflected in the features of the individual clusters. Figure 3.7 shows several sample clusters from various instantaneous realizations, as captured by the large-FOV measurements and identified by the Voronoi diagram method, illustrating the variety of sizes and complex shapes of these objects. Some of them are even larger than the integral scales of the flow, often exceeding the
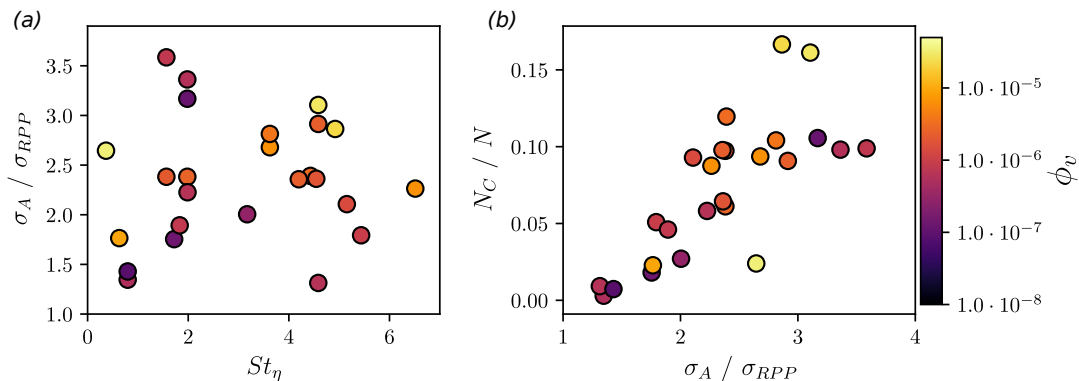
Figure 3.6: Two qualifications of clustering intensity using the Voronoï tessellation method: (a) σ_A/σ_{RPP} representing departure from a random particle distribution versus Stokes number. (b) Fraction of inertial particles belonging to coherent clusters as a function of normalized σ_A/σ_{RPP}.

limits of the imaging window. Their borders are jagged and convoluted, and their bodies non-simply connected. In the following, we provide quantitative support to these observations. We stress that the objects captured by 2D imaging are cross-section of 3D clusters; this naturally conditions our ability to assess their topology. Such limitation, however, is not expected to overshadow the main conclusions of the analysis.

Figure 3.8 shows the PDF of the areas A_C of the clusters, coherent and not, distinguishing between measurements obtained over the small, intermediate, and large FOV. In agreement with Sumbekova *et al.* (2017) and Baker *et al.* (2017), most cases display a power-law behavior over several decades, suggesting a self-similar hierarchy of structures, possibly associated to the scale-invariant properties of the underlying turbulent field (Moisy & Jiménez, 2004; Goto & Vassilicos, 2006). The data is consistent with the previously suggested values of -2 and $-5/3$ for the power-law exponent for planar measurements (Monchaux *et al.*, 2010; Obligado *et al.*, 2014; Sumbekova *et al.*, 2017).

As expected, the spatial resolution influenced the size distributions. The small FOV is affected by a cut-off at large scales. At small scales, the limited resolution in the large FOV makes particles more likely to go undetected due to the glare of their
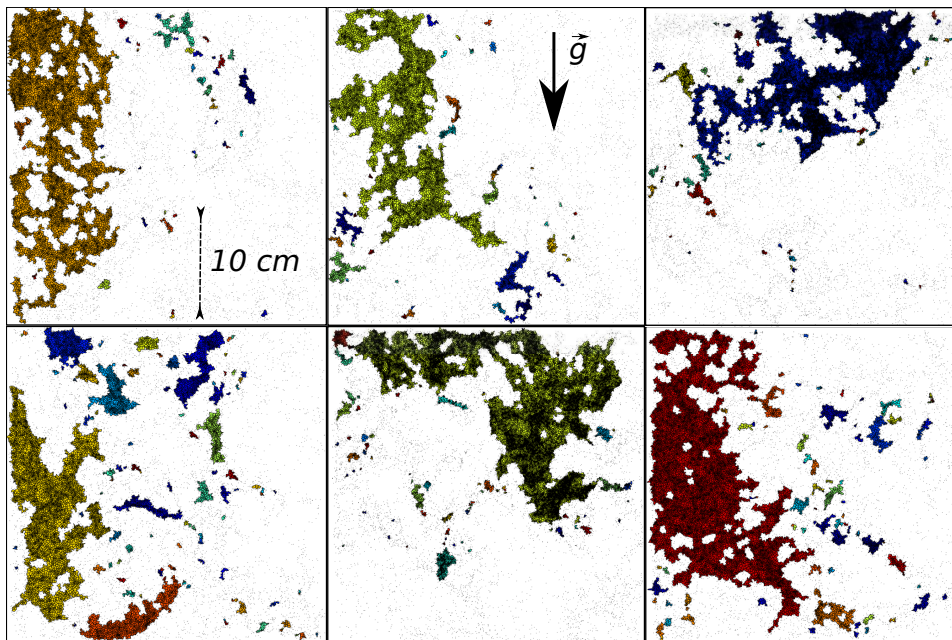
Figure 3.7: Example clusters for the cases $St_\eta = 1.6$ and 4.6 imaged in the large FOV, highlighting the wide variety of sizes and shapes.

neighbors, reducing the probability of finding small clusters. The latter effect can partly explain why the area threshold for self-similarity (see vertical dashed line in figure 3.3d) varies significantly between cases, while it was found to be very consistent in the simulations of Baker *et al.* (2017). Another factor influencing this threshold is the particle volume fraction. Although the value of A^* was shown to be robust to particle subsampling (Monchaux *et al.*, 2012; Baker *et al.*, 2017), varying the number of particles in the domain results in a shift of the cluster area distribution (figure 3.9), which in turn affects the number of detected coherent clusters above the self-similar threshold. Finally, as ϕ_v increases, the possibility of significant two-way coupling effects also increases, which may alter the turbulence structure and consequently the clustering process. This aspect will be discussed in §3.4.

A remarkable aspect of the distributions in figure 3.8 is the non-negligible probability of finding clusters of size comparable to the inertial scales of the turbulence.
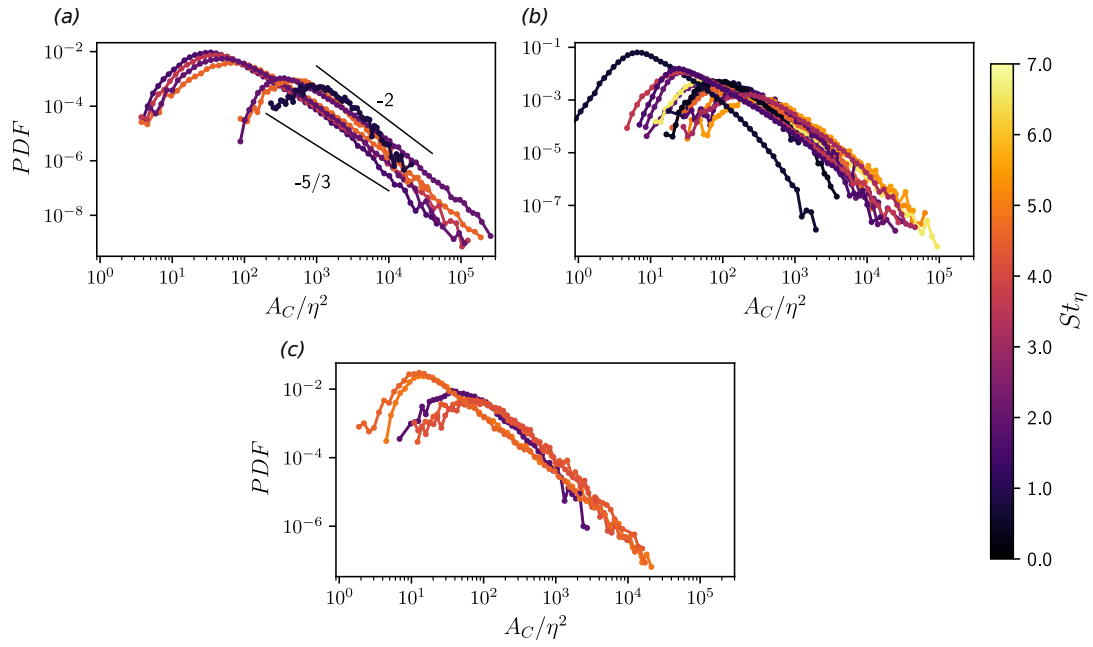
Figure 3.8: PDFs of cluster area normalized by η and separated by field-of-view size. Largest FOV (30x30 cm^2) in (a), medium field (14.5x14.5 cm^2) in (b), and the smallest field in (c) (4.5x4.5 cm^2).
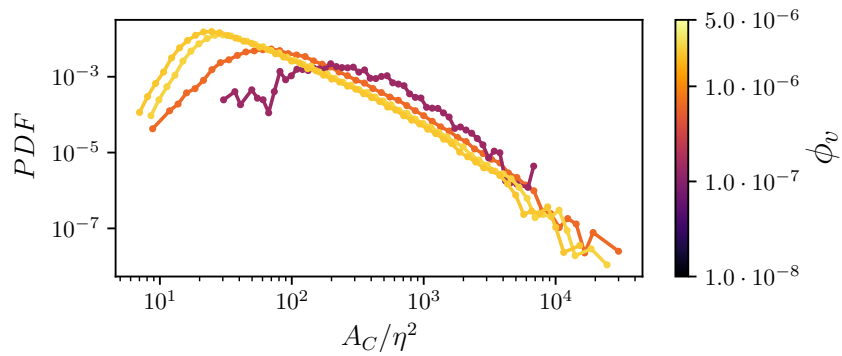
Figure 3.9: PDFs of cluster area for experiments with St_η between 1 and 2.5 (30 μm glass spheres) in the medium field-of-view showing how increasing volume fraction shifts PDFs to smaller scales.
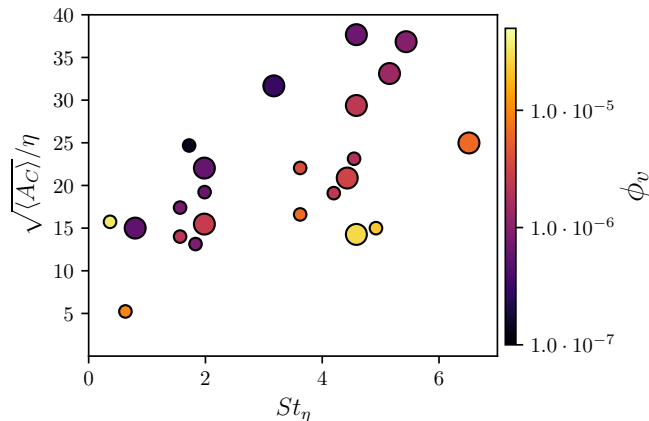
Figure 3.10: Mean cluster area versus particle inertia. Marker size is proportional to Re_λ of the underlying turbulent flow.

Since our definition of coherent clusters entails a power-law size distribution, and this was found to have an exponent close to -2, the mean area of the coherent clusters is ill-defined. In order to compare with past studies, we calculated the mean area of all clusters $\langle A_C \rangle$, below and above the self-similarity threshold, and plot its square root in figure 3.10. The majority of cases display mean sizes between 10η and 40η, with a generally increasing trend with St_η. Several previous studies have reported mean cluster sizes around 10η (Aliseda *et al.*, 2002; Wood *et al.*, 2005; Dejoan & Monchaux, 2013). Most of these studies, however, considered turbulent flows with relatively low Re_λ and thus limited scale separation. Recently, Sumbekova *et al.* (2017) investigated droplets in grid turbulence at Re_λ approaching 500, and found cluster size distributions and averages comparable with ours. At large Reynolds numbers the spectrum of temporal scales widens, and particles with a broad range of response times become susceptible to clustering mechanisms (Yoshimoto & Goto, 2007). As noted in §3.2.2, the more inertial particles respond to larger eddies and therefore can agglomerate in larger sets. The observed dependence of the cluster size with St_η is consistent with this view.

To investigate the degree of self-similarity exhibited by individual clusters, and to

provide a descriptor of their complex shape, we calculated their box-counting dimension. This has been widely used to characterize the topology of both turbulent structures (Moisy & Jiménez, 2004; Lozano-Durán *et al.*, 2012; Carter & Coletti, 2018) and particle clusters in turbulence (Baker *et al.*, 2017). The domain is partitioned into non-overlapping square boxes of side length r, and for each cluster we counted the number of boxes N_B containing at least one particle. If $N_B(r)$ follows a power-law, i.e. $N_B \sim r^{-D}$, over a sizable range of scales, the exponent D is taken as the box-counting dimension of the object, which is in turn a measure of its fractal dimension. (Several other definitions of fractal dimension exist, and typically they only coincide for mathematical constructs, Falconer (2003)) Relatively large objects are needed for a robust estimate of D over a wide range of scales, and we thus consider only clusters of area larger than $10^4\eta^2$. Additionally, we neglect clusters touching the image boundary, as their silhouette would include spurious straight segments. Figure 3.11 shows, for three sample cases, $N_B(r)$ normalized by the maximum number of boxes for each cluster (corresponding to the smallest box size, $r = \eta$). For each case, curves for only 20 example clusters are shown for clarity. These reveal a remarkably consistent box-counting dimension $D \approx 1.6$ over at least a decade of scales; the same trend is followed by all other cases. Baker *et al.* (2017) found $D \approx 1.9$ for 3D clusters. Relating the box-counting dimension of 3D objects and their 2D cross-sections is not straightforward (Tang & Marangoni, 2006; Carter & Coletti, 2018). Rather, the present result may be compared with that of Carter & Coletti (2018) who evaluated the box-counting dimension of turbulent coherent structures using 2D PIV in the same facility. They found $D \approx 1.5$, which suggests a strong link between the particle cluster topology and the underlying turbulent flow. Beside the precise value of the box-counting dimension, the main observation is that large clusters of inertial particles do exhibit a scale-invariant shape in the present range of St_η and Sv_η.

In order to characterize the spatial distribution of particles within each cluster, we use the singular value decomposition (SVD) method introduced by Baker *et al.* (2017).
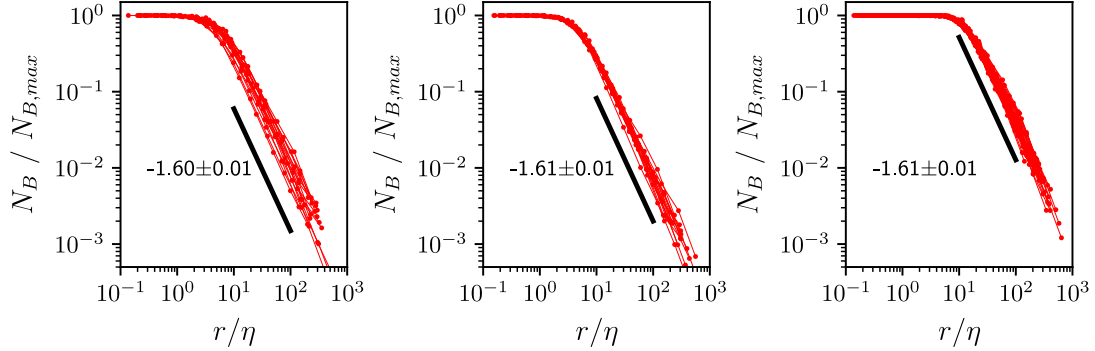
Figure 3.11: $N_B(r)$ for three cases with $St_\eta = 4.6$ in (a), 3.6 in (b)) and 2.0 in (c), normalized by the respective maximum. The box-counting dimension of 1.6 is consistent for all cases.

The SVD provides the principal axes and corresponding singular values for a particle set. In two dimensions, the primary axis lies along the direction of greatest particle spread from the cluster centroid, the secondary axis being orthogonal to it (figure 3.12a). The corresponding singular values s_1 and s_2 measure the particle spread along the respective principal axes, and can be used as simple shape descriptors through the aspect ratio s_2/s_1: the limit $s_2/s_1 = 0$ corresponds to particles arranged in a straight line, whereas $s_2/s_1 = 1$ corresponds to a perfect circle. The PDF of the aspect ratio for all considered cases (figure 3.12b) shows that clusters are likely to exhibit aspect ratios between 0.4 and 0.5, reflecting a tendency to form somewhat elongated objects. Furthermore, the distribution has a positive skew, indicating that globular shapes were more common than extremely long streaks. While these observations are influenced by the 2D nature of the technique, they are consistent with the results of Baker *et al.* (2017) who found that 3D clusters had s_2/s_1 distributions peaking around 0.5, and were positively skewed.

The orientation of the primary axis from the SVD analysis provides information on the cluster orientation in space. In figure 3.13a we plot the PDF of the cosine of θ_g, i.e. the angle between the cluster primary axis and the vertical, evidencing a strong preference for the clusters to align with gravity. That particles tend to agglomerate along
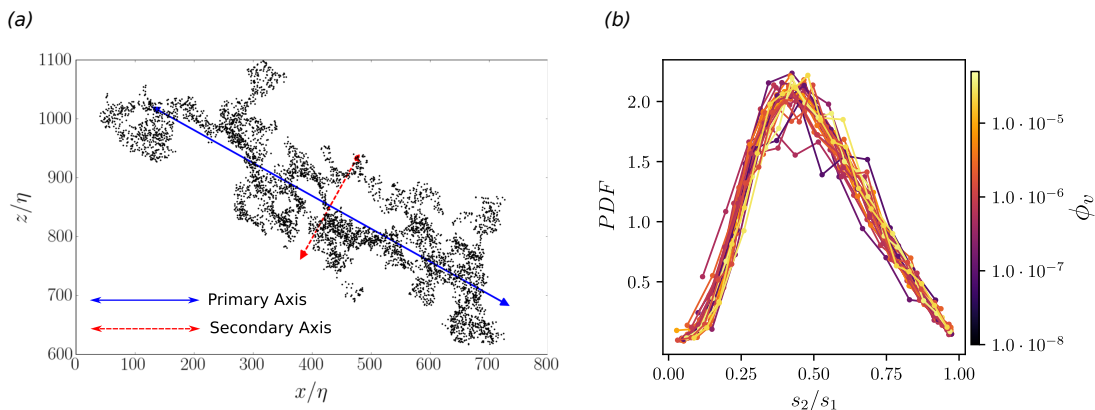
Figure 3.12: (a) A single coherent cluster, with primary and secondary axes as computed through SVD. The length of each arrow is proportional to the corresponding singular value. (b) PDFs of the aspect ratios of clusters for each case.

their falling direction was found in past one-way coupled simulations (Woittiez *et al.*, 2009; Dejoan & Monchaux, 2013; Bec *et al.*, 2014*a*; Ireland *et al.*, 2016*b*; Baker *et al.*, 2017), indicating the mechanism is not necessarily related to the particle backreaction on the flow. Baker *et al.* (2017) reasoned that, especially for cases with high St_η and high Sv_η, particles are influenced by intermittent downward gusts that add to their fallspeed, channeling them and creating elongated quasi-vertical structures. The joint probability distribution of $\cos(\theta_g)$ and A_C (figure 3.13b) supports this view, showing that a vertical alignment corresponded to generally larger clusters. Further studies, possibly including time-resolved information, are needed to gain a mechanistic understanding of the cluster formation process.

We finally consider the concentration of particles within each coherent cluster, $C_C = N_{PC}/A_C$, where N_{PC} is the number of particles in each cluster. Figure 3.14a,b shows scatter plots of cluster areas and number of particles for two representative cases. The excellent fit using a power law of exponent close to unity indicates that the relationship is approximately linear, i.e. the concentration within each cluster is approximately the same for a given case. This trend is recovered for all cases. Considering the wide
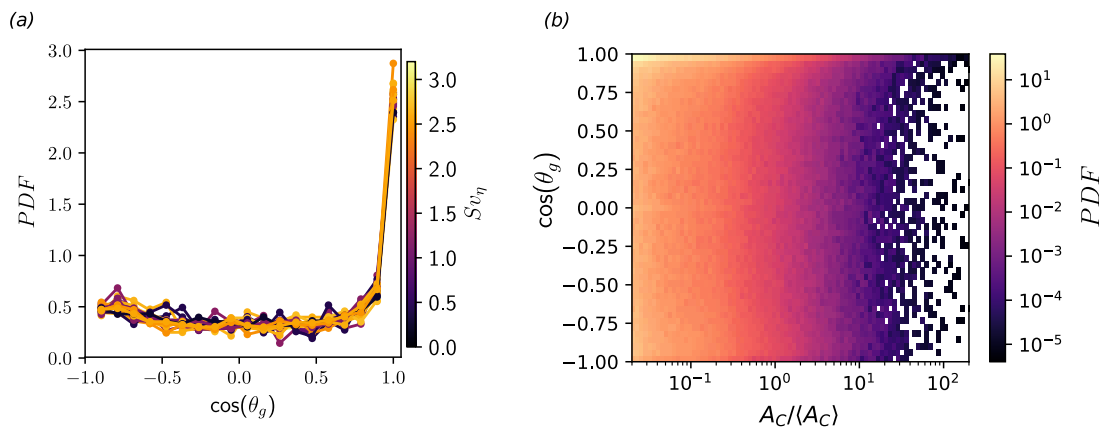
Figure 3.13: (a) PDFs of the cosine of the angle between clusters' primary axis and the vertical. (b) Joint PDF of angle from vertical and size of cluster.

range of sizes, this result (reported by Baker *et al.* (2017) at a much lower Re_λ) indicates again that clusters display scale-invariant features. Figure 14c illustrates the average in-cluster concentration as a function of St_η. Despite the scatter (which points to the concurrent effect of the multiple parameters at play), one notices an increase up to $St_\eta \approx 2$, followed by a plateau. The concentration within clusters can be up to an order of magnitude higher than the average over the whole particle field $(C_0 = 1/\langle A \rangle)$; these values are likely underestimated as particles may shadow each other at high local concentration. The present results are comparable to those from the experiments by Monchaux *et al.* (2010) and the DNS by Baker *et al.* (2017).

3.3 Settling velocity

3.3.1 Mean settling velocity

In this section we present and discuss the settling velocity measurements W_s, obtained ensemble-averaging over all particles and realizations for each case. In figure 3.15a this is normalized by W_0 (so that values greater and smaller than one indicate turbulence-enhanced and turbulence-inhibited settling, respectively) and plotted against
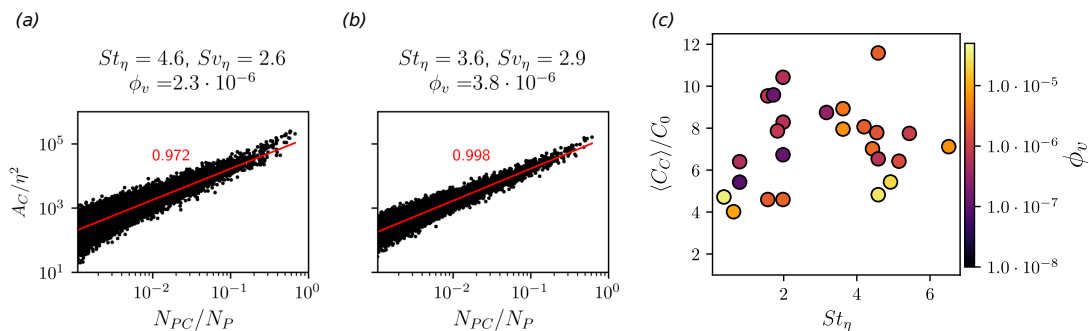
Figure 3.14: (a,b): Scatter plots of cluster area (normalized by the Kolmogorov scale) versus the number of particles in each cluster (normalized by the total number of particles in the domain) for two sample cases. (c): Average particle concentration in the clusters, normalized by the global concentration, plotted versus St_η and colored by overall solid-volume fraction.

St_η. The main contribution to the error is the uncertainty in τ_p due to the particle size variance, and the non-zero vertical air velocity measured at the same time as the settling. We only plot cases in which the mean vertical fluid velocity is smaller than $0.25W_s$, and in fact in most cases it is $0.01 - 0.05W_s$. The first observation from the plot is that the vast majority of cases display strong settling enhancement, especially for $St_\eta \approx 1$, which is consistent with most previous numerical (Wang & Maxey, 1993; Bosse & Kleiser, 2006; Dejoan & Monchaux, 2013; Bec *et al.*, 2014*a*; Ireland *et al.*, 2016*b*; Rosa *et al.*, 2016) and experimental studies (Aliseda *et al.*, 2002; Yang & Shy, 2003, 2005; Good *et al.*, 2014). The amount of such increase is more remarkable, with the settling velocity being enhanced by a factor 2.6 for $St_\eta \approx 1 - 2$. As mentioned in the Introduction, most numerical studies reported maximum increase in fallspeed between about 10% and 90%; some experiments (Yang & Shy, 2003, 2005) found even smaller values. The present results instead indicate that turbulence can lead to a multi-fold increase in settling rate, which agrees with the conclusions from the field study of Nemes *et al.* (2017).

Similar levels of settling enhancement could also be deduced from the data of Aliseda *et al.* (2002) and Good *et al.* (2014); and while the former used concentrations
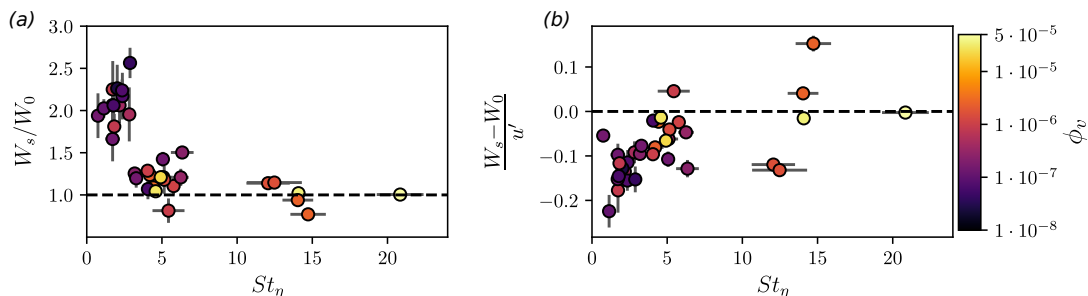
Figure 3.15: (a) Measured settling velocity normalized by the still-fluid Stokes value versus St_η and colored by solid-volume fraction. (b) Measured settling velocity variation from the still-fluid Stoked value normalized by the fluid r.m.s. fluctuations.

where collective effects are expected ($\phi_v \geq 10^{-5}$), the latter used particle loadings small enough to neglect two-way coupling ($\phi_v \approx 10^{-6}$). In fact, those authors did not explicitly mention a multi-fold increase in vertical velocity, as they mostly plotted their data as $(W_s - W_0)/u'$. We present this scaling in figure 3.15b, where a maximum settling enhancement of $0.28u'$ was found for $St_\eta \approx 1$, again in good agreement with those authors. (Note that the vertical velocity is positive when downward, hence negative values imply settling enhancement and vice versa.) The scatter and the superposition of multiple factors prevented distinguishing a clear trend at the larger St_η. Those data points were also at relatively high ϕ_v, which may have had a non-trivial influence on settling, as we discuss later. Thus, the reduced settling exhibited by some of the most inertial cases, while it might appear consistent with recent results (Good *et al.*, 2014; Rosa *et al.*, 2016), should be considered with caution.

Figure 3.16 shows the results in the $St_\eta - Sv_\eta$ plane. This provides a clearer view of the data, as both parameters are expected to have significant influence on the dynamics. The maximum enhancement of settling rate occurs when both St_η and Sv_η are close to unity, in broad agreement with Good *et al.* (2014) and Rosa *et al.* (2016). The distribution of values suggests that a dependence with $StSv$ may capture the observed trend. Figure 3.16b shows the settling enhancement ratio against the group $St_\eta Sv_L$, displaying
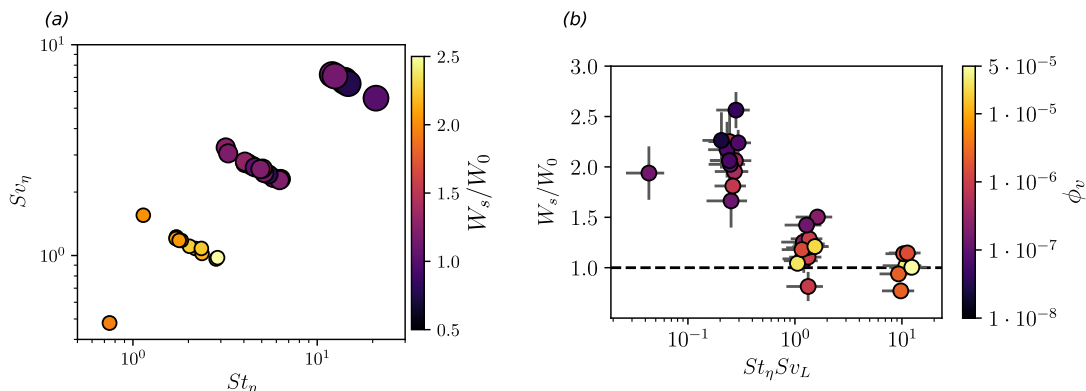
Figure 3.16: (a) Settling increase plotted as a function of both St_η and Sv_η. (b) Settling increase as a function of the mixed scale, $St_\eta Sv_L$.

a significantly improved collapse of the data. This scaling follows the argument of Nemes *et al.* (2017) that τ_η and u' are the main time and velocity scales, respectively, determining increase of fallspeed by turbulence. That both the small and large eddies impact the settling process has been acknowledged (Good *et al.*, 2014), and already Wang & Maxey (1993) favored u' over u_η as driving parameter. Yang & Lei (1998) explicitly indicated τ_η and u' as the correct flow scales, reasoning that the former controlled clustering and the latter controlled the drag experienced by the particles. The group $St_\eta Sv_L$ can be interpreted as the ratio of the particle stopping distance ($\tau_p^2 g$) and a mixed length scale ($\tau_\eta u'$); settling enhancement appears most effective when this ratio is $O(0.1)$. This is approximately the condition at which Nemes *et al.* (2017) reported turbulence-augmented fallspeeds of snowflakes in the atmospheric surface layer ($Re_\lambda \approx 10^3$). Mixed-scaling arguments have been successfully used in various turbulent flows (e.g., in boundary layers, (Graff & Eaton, 2000)) but their theoretical underpinning poses issues which are beyond the scope of the present study.

Overall, the results presented in this section indicate that turbulence greatly enhances the settling velocity of sub-Kolmogorov particles with Stokes number around unity, which is consistent with the preferential sweeping mechanism proposed by Wang

& Maxey (1993). However, a full demonstration of this view requires the simultaneous measurements of particle and fluid velocity. These will be presented in §5.2.

3.3.2 Settling velocity conditioned on particle concentration

To explore the interplay between the particle accumulation and settling mechanisms, we consider the fallspeed associated to individual coherent clusters. In figure 3.17 we plot the cluster settling velocity W_C, obtained by averaging the vertical velocity of all particles belonging to a given clustered set. This is normalized by the mean settling velocity W_s, and plotted against the cluster area. Overall, clusters settle significantly faster than the mean, and there was an apparent trend of increasing fallspeed with cluster size, especially for the larger objects. There are two possible interpretations for this result. On one hand, clustered particles may affect the flow by virtue of their elevated concentration, exerting a "collective drag" on the surrounding fluid that results in increased settling velocity. This view reflects the argument proposed by Bosse & Kleiser (2006) in interpreting their two-way coupled DNS study. On the other hand, particles may be merely oversampling downward regions of flow according to the preferential sweeping mechanism, and therefore cluster in such regions, leading to the observed trend. This latter interpretation, which does not require any significant two-way coupling between the dispersed and continuous phase, is consistent with the results of Baker *et al.* (2017), who reported cluster fallspeeds up to twice the mean particle settling velocity in their one-way-coupled DNS.

Contrasting the effect of local and global concentration may provide further hints. In figure 3.18, the particle settling velocity of all particles W_s (normalized by the still-air fallspeed W_0) is plotted against the local relative concentration C/C_0 (which is readily available for each particle from the Voronoï diagrams). As expected, W_s/W_0 increases monotonically with C/C_0, in agreement with the trends reported by Aliseda *et al.* (2002). Indeed, particles residing in regions of low concentration are often associated with upward
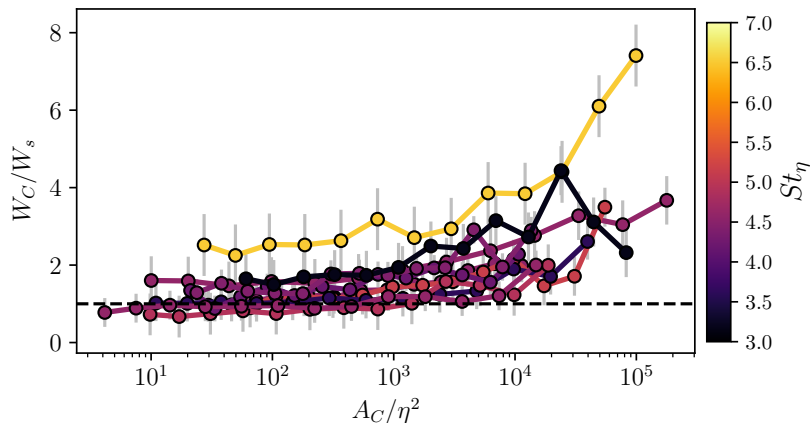
Figure 3.17: Average settling velocity of all clusters as a function of cluster size. Error bars indicate ± the standard deviation.

velocity. We also observed, although with some scatter, the beginning of a plateau in the settling enhancement around $C/C_0 \approx 5$. More importantly, the plot clearly indicates that the fallspeed dependence with concentration is strongly mitigated at larger global volume fractions, ϕ_v. If the high fallspeed of the clusters are mainly due to a collective effect of the particles on the fluid, we would expect such speed to be further enhanced with increasing ϕ_v. The fact that the opposite is true rather suggests that the augmented cluster settling is mainly caused by preferential sweeping (or other mechanisms not depending on the mass loading). In fact, figure 3.18 suggests that two-way coupling may be significant over the considered range of ϕ_v, but its effect may be subtle: if the particles are altering the turbulence structure, this backreaction can have a non-trivial effect on the settling rate. In general, it should be remarked that the simultaneous variation of multiple physical parameters between the considered cases (in this as in other studies) is a confounding factor in determining the role of two-way coupling, and one cannot rule out the influence of collective drag on the settling velocity (as argued by Huck *et al.* (2018)). Future dedicated studies, in which the global volume fraction is systematically varied while keeping all other parameters constant, may help shed light
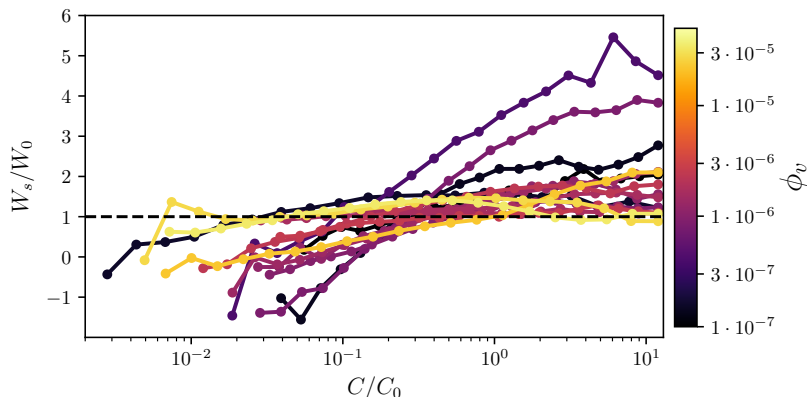
Figure 3.18: Normalized vertical particle velocity conditioned on the local particle concentration.

on this point.

3.4   Analysis of simultaneous particle and fluid fields

In this section we investigate the particle-fluid interaction by exploiting the concurrent PIV/PTV measurements of both phases. These allow us to demonstrate and quantify effects which, although considered hallmarks of particle-laden turbulence, had rarely (if ever) been documented in experiments.

3.4.1   Preferential concentration

The fact that inertial particles oversample high-strain/low-vorticity regions, as theorized by Maxey (1987) and demonstrated numerically by Squires & Eaton (1991), was confirmed by several later DNS studies of homogeneous turbulence, at least for $St_\eta \leq 1$ (Chun *et al.*, 2005; Bec *et al.*, 2006; Cencini *et al.*, 2006; Coleman & Vassilicos, 2009; Salazar & Collins, 2012; Ireland *et al.*, 2016*a*; Esmaily-Moghadam & Mani, 2016; Baker *et al.*, 2017). To our knowledge, this prediction has not been directly verified by experiments in fully turbulent flows. Indeed, most previous laboratory studies on

this topic only captured the dispersed phase (Fessler *et al.*, 1994; Aliseda *et al.*, 2002; Wood *et al.*, 2005; Salazar *et al.*, 2008; Saw *et al.*, 2008; Gibert *et al.*, 2012), and as such could only provide results consistent with a certain picture of preferential concentration, rather than demonstrating it. We characterized the local balance of strain-rate versus rotation in the particle-laden air flow measured by PIV, using the second invariant of the velocity gradient tensor $Q = 1/2(\mathbf{\Omega}^2 - \mathbf{S}^2)$, where $\mathbf{S}$ and $\mathbf{\Omega}$ are the symmetric and anti-symmetric parts of the velocity gradient tensor (Hunt *et al.*, 1988). To this end, we calculated spatial derivatives using a second-order central difference scheme on the small and medium-FOV fields, where our resolution is sufficient to capture the Kolmogorov scales (Worth *et al.*, 2010; Hearst *et al.*, 2012). From the planar data we can only determine the four components in the upper-left 2 x 2 block of the full 3 x 3 velocity gradient tensor. This limitation needs to be kept in mind, because 2D sections of 3D flows can sometimes be misleading (Perry & Chong, 1994). However, several studies showed how high-resolution 2D imaging of homogeneous turbulence yields features of the coherent structures and high-order statistics in quantitative agreement with 3D imaging and DNS (Fiscaletti *et al.*, 2014; Carter & Coletti, 2018; Saw *et al.*, 2018). Therefore, we do not expect the qualitative results of the present analysis to be biased by the nature of the measurements.

Figure 3.19 shows the fraction of inertial particles found in regions where $Q < 0$. As expected, this fraction is larger than 50% for all cases, confirming that the particles were more likely to be found in strain-dominated regions than rotation-dominated ones. The figure also presents the percentage of clustered particles found in $Q < 0$ regions. Interestingly, the fraction was systematically lower compared to the entire particle set. This suggests that the preferential sampling of high-strain regions might not be the main factor (or at least not the only one) for the formation of clusters over the considered parameter space. Indeed, most of our cases feature particles with $St_\eta > 1$, and in this regime several numerical studies indicate that the nature of the clustering mechanism is
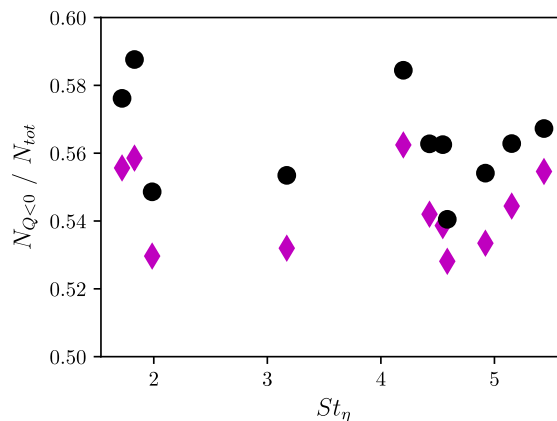
Figure 3.19: Fraction of particles in rotation-dominated regions. Black circles represent all particles in the field, while the purple diamonds represent only particles in coherent clusters.

different compared to weakly inertial particles (Bec *et al.*, 2007; Coleman & Vassilicos, 2009; Bragg & Collins, 2014; Bragg *et al.*, 2015). In particular, Bragg & Collins (2014) argued for the importance of path-history effects (i.e., particles retaining memory of the velocity fluctuations they experienced), while Vassilicos & coworkers (Chen *et al.*, 2006; Goto & Vassilicos, 2008) proposed that clustering in this range is due to a sweep-stick mechanism (i.e., particles sticking to zero-acceleration points which are swept and clustered by large-scale motions). A critical discussion of these and other possible explanations is beyond the scope of this work. In fact, while instantaneous realizations and velocity statistics may provide support to a given theory (see Obligado *et al.*, 2014; Sumbekova *et al.*, 2017), time-resolved measurements would be better suited to inform a mechanistic understanding of the process.

3.4.2   Preferential sweeping

As discussed previously, preferential sweeping is considered the most impactful mechanism by which turbulence affects the fallspeed of sub-Kolmogorov particles. Its main manifestation is the tendency of particles with Stokes number of order one to
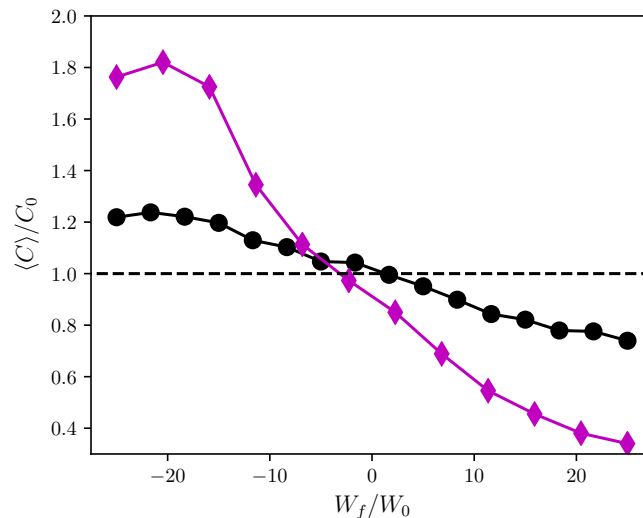
Figure 3.20: Example case of the relative particle concentration conditioned on the vertical fluid velocity (normalized by the still-air settling velocity.) Black circles indicate the full particle set, while purple diamonds represent only particles in clusters.

oversample regions of downward velocity fluctuations. This was first theorized by Maxey & Corrsin (1986) and Maxey (1987), demonstrated numerically by Wang & Maxey (1993), and confirmed by several other analytical and computational studies (Yang & Lei, 1998; Dávila & Hunt, 2001; Dejoan & Monchaux, 2013; Frankel *et al.*, 2016; Baker *et al.*, 2017). While laboratory studies (Aliseda *et al.*, 2002; Yang & Shy, 2003, 2005; Good *et al.*, 2014)and field observations (Nemes *et al.*, 2017) showed results consistent with this picture, no direct experimental verification has been reported. Similar to preferential concentration, the challenges associated to two-phase measurements may be responsible.

We provid such verification first by considering the particle concentration conditionally averaged on the local fluid velocity. This was obtained by counting the number of inertial particles in each PIV interrogation window, and binning the results by the value of W_f/W_0 (because the mean vertical fluid velocity was negligibly small, total and fluctuating components coincide). The relative concentration was calculated as the

number of particles in each bin, divided by the sum of window areas associated to that bin, and finally normalized by the global concentration. The procedure is equivalent to that originally adopted by Wang & Maxey (1993) and later by Baker *et al.* (2017) to analyze DNS results, with the PIV interrogation windows in lieu of the computational cells. In figure 3.20 we show the result for a representative case, clearly indicating downward fluid velocity corresponding to higher local concentration. When the process was repeated only considering particles belonging to clusters, the trend was significantly more pronounced. This is consistent with the result that clusters fall at faster speeds than the rest of the particles (figure 3.17). At the same time, it also supports the idea that preferential sweeping plays an important role in the clustering of settling particles.

To quantify the impact on the settling rate, we considered the vertical component of the fluid velocity at the particle location, $W_f(\mathbf{x_p})$ (figure 3.21). The latter was approximated via a piecewise linear interpolant between the particle position and the four closest fluid velocity vectors; tests with other schemes indicated only a weak dependence with the interpolation method. Error analysis based on the fluid velocity gradient statistics (see Carter *et al.*, 2016; Carter & Coletti, 2017) yield uncertainty on $W_f(\mathbf{x_p})$ around $2 - 7\%\ u'$. Despite some scatter partly attributable to the several factors at play, the results indicat that preferential sweeping is important for most considered regimes, being the strongest for $St_\eta = O(1)$.

Comparing figure 3.15b and 3.21, the oversampling of downward fluid velocity regions seems to account for a large part of the settling enhancement. A more quantitative account can be given in the framework of the point-particle approximation. Retaining only drag and gravity in the particle equation of motion, the fallspeed can be approximated as (Wang & Maxey 1993):

$$\langle W_s \rangle \approx \langle w_f(\mathbf{x_p}, t) \rangle + \frac{\tau_p g}{\langle f \rangle} \tag{3.5}$$

where $w_f(\mathbf{x_p})$ is the vertical fluid velocity at the particle location obtained via the
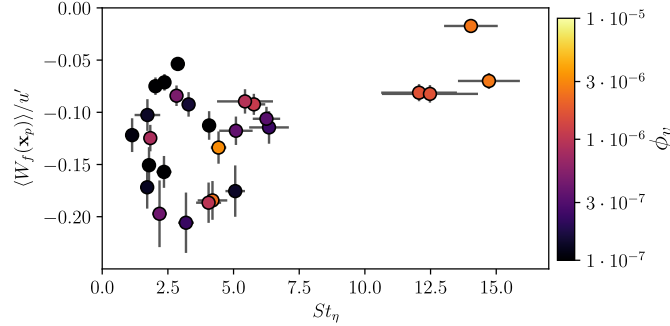
Figure 3.21: Vertical fluid velocity at particle location, normalized by the fluid rms velocity, plotted versus particle Stokes number.

piecewise-linear interpolation, and $\langle f \rangle$ is the ensemble-average of Schiller & Naumann correction factor in equation (2.1), $f = 1 + 0.15 Re_p^{0.687}$. We can directly verify this approximation using the instantaneous Re_p measured from the simultaneous PIV/PTV measurements (which will be discussed further in the next section). Figure 3.22 shows the ratio between the fallspeed calculated from (3.5) and the measured values. This formulation consistently underpredicts the measured fallspeed. Such a discrepancy between experiments and theory suggests that the one-way coupled point-particle approach, while providing the correct qualitative trend, is missing significant aspects of the particle-fluid interaction. We investigate possible sources of the mismatch in §3.4.4, where we consider the instantaneous slip velocity.

3.4.3 Crossing-trajectory and continuity effect

Since Yudine (1959), it has been recognized that the drift induced by body forces such as gravity causes heavy particles to decorrelate from their past velocity faster than a fluid element. This so-called crossing trajectory effect can be quantified by the Lagrangian autocorrelation of the particle velocity (Elghobashi & Truesdell, 1992). For large drift velocities, this reduces to the fluid space-time correlation in an Eulerian frame (Csanady, 1963; Squires & Eatons, 1991). In this limit, as the longitudinal integral scale
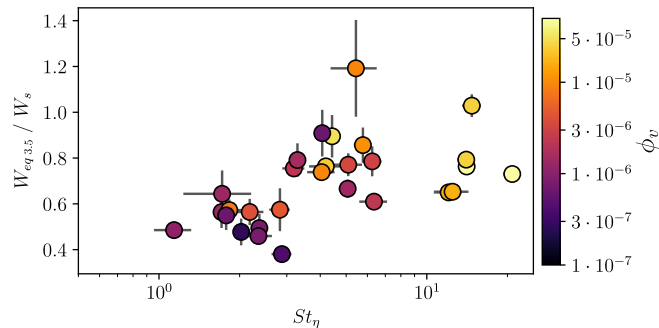
Figure 3.22: Prediction of settling velocity based on equation 3.5 normalized by the measured settling velocities, versus particle Stokes number.

is twice the transverse one, the particle dispersion parallel to the drift direction is double the dispersion perpendicular to it (the so-called continuity effect; Csanady (1963); Wang & Stock (1993)). The footprints of these effects are visible in the Eulerian particle velocities. In figure 3.23 we present a scatter plot of the vertical and horizontal r.m.s. particle velocity fluctuations ($W_{p,rms}$ and $U_{p,rms}$, respectively), normalized by the r.m.s. fluid fluctuations in the respective directions (u'_z and u'_x) to account for the anisotropy in our facility. The normalized vertical fluctuations of the particles exceed those in the horizontal direction, the disparity being more substantial for larger Sv_η. This trend is consistent with the continuity effect, and in line with previous analysis of Wang & Stock (1993) and measurements of Good *et al.* (2014): the falling particles have more time to respond to the vertical fluid fluctuations, due to the larger longitudinal integral scale compared to the transverse one.

3.4.4 Particle-fluid relative velocity

The relative (slip) velocity between suspended particles and the surrounding fluid plays a vital role in both the particle kinematics and the interphase coupling. The slip velocity determines the exchanged forces and the local flow regime around a particle (Maxey & Riley, 1983; Calzavarini *et al.*, 2008; Bellani *et al.*, 2012), and is critical for the
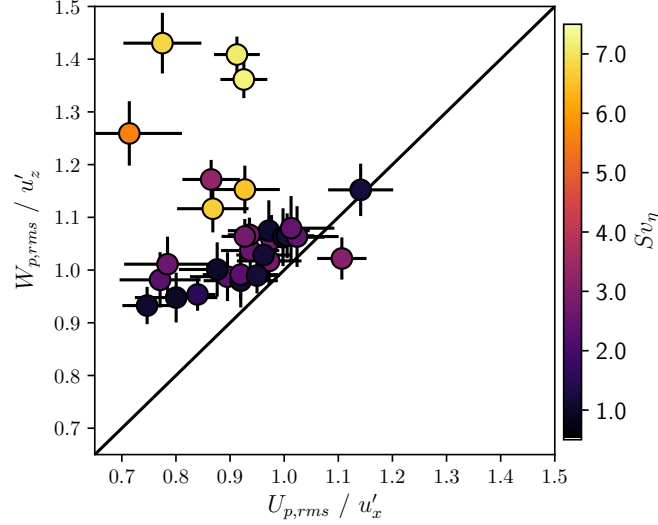
Figure 3.23: Ratio of vertical particle to fluid rms velocity versus ratio of the same horizontal velocities.

momentum two-way coupling with the fluid (Sahu *et al.*, 2016). It is also a key quantity for modeling sub-grid scale dynamics in large-eddy simulations of particle-laden turbulence (Soldati & Marchioli, 2009). Due to the abovementioned difficulties in measuring both phases, the slip velocity has been reported by only a few experimental studies, notably Kiger & Pan (2002) and Khalitov & Longmire (2003) in wall-bounded turbulent flows, and Yang & Shy (2005) and Sahu *et al.* (2016) in homogeneous turbulence.

Here we evaluate the slip velocity as $\mathbf{u}_{slip} = \mathbf{v_p} - \mathbf{u_f}(\mathbf{x_p})$, where $\mathbf{v_p}$ is the particle velocity vector. In the present measurements we only have access to the in-plane projection of those vectors. Here we only used data from the small and intermediate FOVs. We remark that the relevant definition of slip velocity (as it appears, e.g., in Stokes' drag law) is the difference between the particle velocity and the undisturbed fluid velocity evaluated at the particle location. Because in the considered cases $d_p < \eta$ and $Re_{p,0} \leq 1$, the region of perturbation from an individual particle (as estimated, e.g., by the Oseen's solution) is expected to be a few particle diameters, i.e. typically

smaller than the Kolmogorov scale. Under this assumption, the interpolated fluid velocity approximates the undisturbed velocity. However, as we shall see, the instantaneous particle Reynolds number Re_p can reach much larger values than $Re_{p,0}$.

Figure 3.24a presents PDFs of the slip velocity magnitude normalized by the fluid r.m.s. fluctuation. At the higher St_η, $\mathbf{u}_{slip}$ can significantly exceed u', suggesting that the potential energy transferred to the fluid by the fast falling particles is considerable with respect to the turbulent kinetic energy. We will return to this point in §3.4.5. In figure 3.24b we plot the PDF of the vertical component of the slip velocity W_{slip}, normalized by the still-air particle settling velocity W_0. The mean vertical slip is approximately equal to W_0, as one expects from eq. 3.5. However, the standard deviation is large and, especially for the lower St_η, greatly exceeds the mean value; indeed, the probability of an upward particle slip is significant. This behavior is consistent with the simulations of particle-laden wall-bounded turbulence by Zhao *et al.* (2012), who found that the r.m.s. fluctuations of both streamwise and wall-normal slip velocities were several times greater than their mean. The r.m.s. slip velocities are presented in figure 3.24c,d separating horizontal and vertical components and normalizing by the r.m.s. fluid velocity fluctuations in their respective directions. The slip velocity fluctuations increas with St, also consistent with the results of Zhao *et al.* (2012): the heavier particles increasingly move independently from the fluid, and their r.m.s. slip velocities reach levels comparable to the r.m.s fluid fluctuations. The vertical r.m.s. is consistently higher than the horizontal. This is likely a consequence of the vertical r.m.s. velocity of the particles being larger than the horizontal one, as discussed in the previous section.

The magnitude of the in-plane slip velocity can be used to calculate the instantaneous particle Reynolds number. The PDFs of Re_p for various cases are plotted in figure 3.25a, with the vertical lines indicating the respective theoretical $Re_{p,0}$. The large slip variance results in long tails of the distributions: while the wake-shedding regime is never achieved, there is a sizeable probability of Re_p being an order of magnitude larger
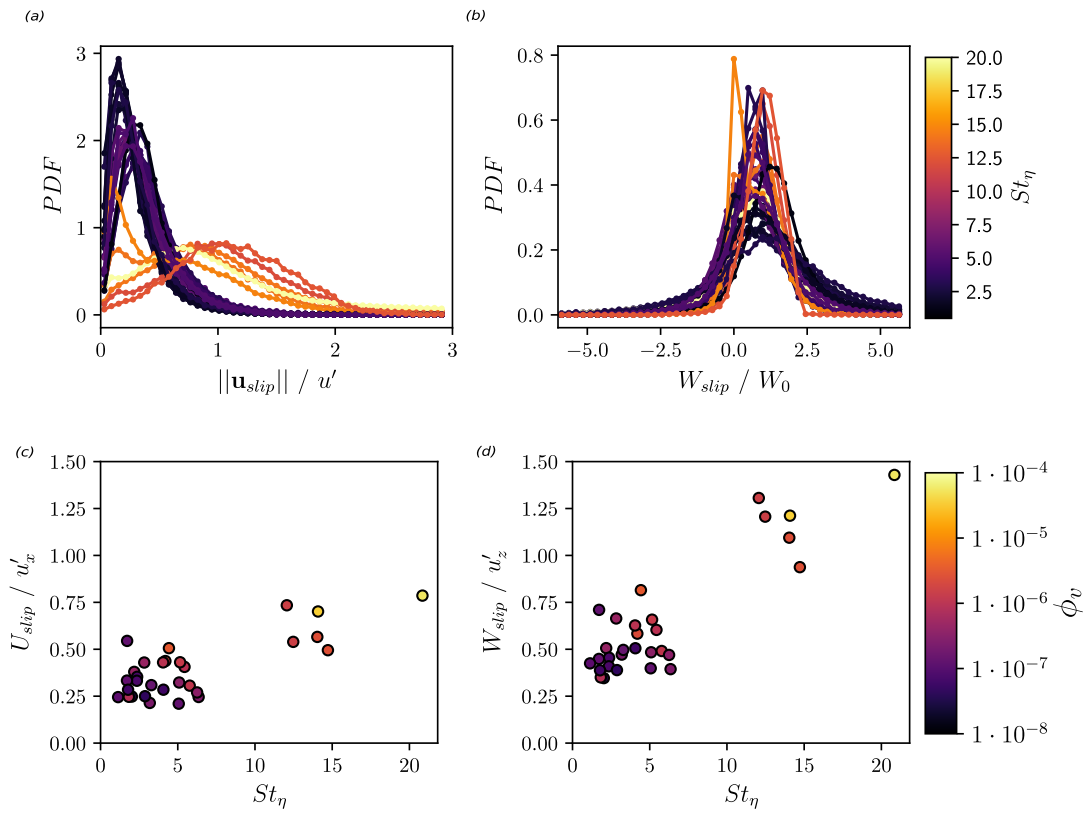
Figure 3.24: Probability density functions of slip velocity magnitude normalized by fluid r.m.s. velocity (a), and vertical slip velocity (b) normalized by the still-fluid settling. (c) and (d) plot horizontal and vertical r.m.s. particle slip velocity, respectively, normalized by the fluid r.m.s. fluctuations along the corresponding direction.

or smaller than the nominal value. The values are in fact somewhat underestimated, because the out-of-plane slip is not accounted for.

The slip velocity and Reynolds number can be used to evaluate the drag coefficient on the settling particles. In presence of background turbulence, this is expected to differ from the "standard drag" in a steady uniform flow (Bagchi & Balachandar, 2003). The latter can be estimated following Schiller & Naumann correction for finite Reynolds number:

$$C_{d,SN} = \frac{24}{Re_{p,0}} \left(1 + 0.15 Re_{p,0}^{0.687} \right) \tag{3.6}$$

As suggested by Balachandar & Eaton (2010), for particles settling in zero-mean flow homogeneous turbulence, one can evaluate an effective drag coefficient:

$$C_{d,eff} = \frac{24}{\langle Re_v \rangle} \frac{1}{\langle W_p \rangle} \left| \langle \mathbf{u}_{slip} \rangle + 0.15 \left(\frac{d_p}{\nu} \right)^{0.687} \langle \mathbf{u}_{slip}^{1.687} \rangle \right| \tag{3.7}$$

where $Re_v = d_p|\mathbf{v_p}|/\nu$. This may differ from the $C_{d,SN}$ owing to three main factors: the mean fluid velocity seen by the particles being non-zero (e.g., due to preferential sweeping); the non-linear relation between drag and slip velocity; and possible two-way coupling. Most previous studies concerned with the influence of ambient turbulence on C_d considered larger Re_p compared to the present case (typically of order $10^2 - 10^3$; e.g., Wu & Faeth (1994); Warnica *et al.* (1995); Bagchi & Balachandar (2003)). In these cases, the effect on the mean drag was found to be small. Bagchi & Balachandar (2003), however, recognized the potential importance of preferential flow sampling for particles falling freely through turbulence. Here we use eqs. 3.6 and 3.7 and plot the ratio $C_{d,eff}/C_{d,SN}$ in figure 3.25b. There is a significant reduction in effective drag over the St_η range displaying preferential sweeping. This is consistent with the early measurements of Rudoff & Bachalo (1988), who found substantially reduced drag for liquid droplets in turbulent air. We also observe a clear increasing trend with St_η. This is likely a consequence of diminishing preferential sweeping effects, giving way to those of
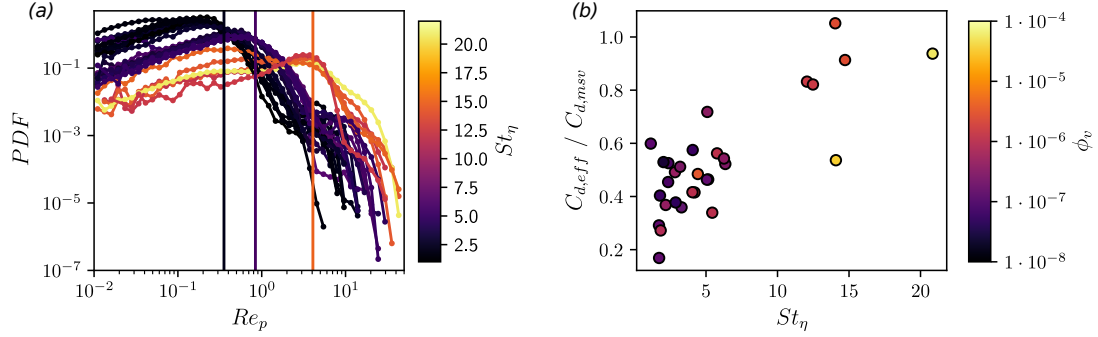
Figure 3.25: PDFs of instantaneous particle Reynolds number. Vertical lines represent average Reynolds particle number based on the Stoked still-fluid settling velocity for each respective grouping of experiments. In (b), the ratios between drag coefficients 5.2 and 5.3, showing reduced drag when the "effective drag" model is used.

non-linear drag and possibly loitering (Good *et al.*, 2014). We remark, however, that the high-St data points are affected by larger uncertainty due to two factors: non-negligible perturbation of the local fluid velocity by the particles (because of their relatively large Re_p), and limited spatial resolution (because those are imaged with the intermediate FOV). Thus, further analysis and measurements are warranted for those regimes.

We then considered the spatial orientation of the particle slip velocity. Figure 3.26a shows the PDF of $\cos(\theta)$, θ being the angle between $\mathbf{v_p}$ and $\mathbf{u_f(x_p)}$. For moderate particle inertia ($St_\eta < 10$) the fluid and particle velocity vectors tend to be closely aligned, with $\theta < 30\,\mathrm{deg}$ in more than 90% of the instances. As expected, the more inertial particles are more likely to display a velocity orientation substantially different from the fluid velocity. The probability of oppositely aligned vectors is also non-negligible, possibly due to weak upward gusts that are unable to reverse the particle settling motion. The probability distribution of slip orientation and magnitude is illustrated by the wind rose diagrams in figure 3.26b for selected cases. The length of each spoke represents the probability associated to its orientation; additionally, each spoke is broken down in segments representing the probability of a certain slip velocity magnitude (normalized by W_0). In all cases the slip velocity favors the downward direction, as expected. In the
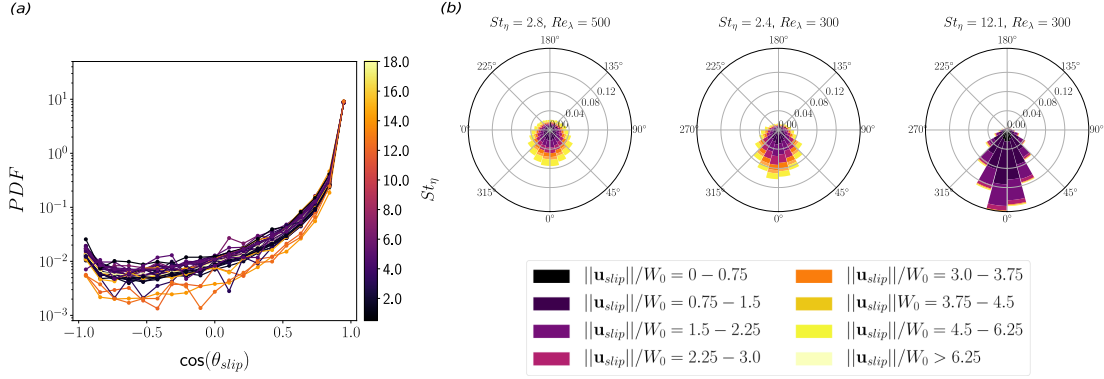
Figure 3.26: PDF of the cosine of the angle between the particle velocity and the fluid velocity at the particle location (a). In (b), three example cases showing the probability distribution of the slip velocity orientation and magnitude.

larger Re_λ cases, however, the strong fluid velocity fluctuations mitigate this tendency and the azimuthal distribution of the particle slip is less skewed. As discussed above, particles with $St_\eta \approx 1$ can have slip velocities several times larger than their still-air fall speed. On the other hand, $\mathbf{u_{slip}}$ for the more inertial cases is closer in magnitude to W_0 and mostly oriented downward (typically within $\pm 45\,$deg from the vertical), confirming that these particles follow more ballistic downward trajectories.

3.4.5 Turbulence modification by particles

We finally consider the scale-by-scale effect of the particles on the fluid turbulent fluctuations by means of the second-order structure functions, which contain analogous information as the energy spectra used in most previous studies:

$$D_{ii}(\mathbf{r}) = \overline{[u_i(\mathbf{x} + \mathbf{r}) - u_i(\mathbf{x})]^2} \tag{3.8}$$

Here $\mathbf{x}$ is the generic location on the imaging plane, $\mathbf{r}$ is the separation vector, and u_i is the i-th component of the velocity fluctuations. Thus, we denote as D_{uu} and D_{ww} the structure functions associated to the horizontal and vertical components. We

focus on longitudinal structure functions (i.e., with separations parallel to the velocity components), the transverse structure functions yielding similar results. For this analysis we used only small and intermediate FOVs, in order to resolve a sufficient fraction of the fine-scale fluctuations.

Figure 3.27 displays horizontal and vertical structure functions for representative cases, comparing the laden and unladen measurements. At very low volume fractions ($\phi_v = O(10^{-7})$), the particles marginally affect the energy distribution across scales, and the expected scaling $D_{ii}(r) \sim r^{2/3}$ is approached entering the inertial range according to Kolmogorov theory (Fig. 3.27a). At significant loadings ($\phi_v = O(10^{-5})$), we observe an increase of turbulent energy at small scales. For $St_\eta = O(1)$ (figure 3.27b) the laden and unladen curves approached each other at larger scales, possibly leading to a cross-over which however is not captured within the field of view. At $St_\eta = O(10)$, the crossing happens at smaller scales as demonstrated in figure 3.27d, in which particles appear to excite turbulent fluctuations at the small scales and modulate them at the large scales. This behavior (sometimes termed "pivoting") was reported by several numerical studies, as reviewed in detail by Poelma & Ooms (2006). Most of those (e.g., Sundaram & Collins, 1999; Ferrante & Elghobashi, 2003) showed the cross-over wavenumber to increase with increasing particle response time, consistent with our observations. The only previous experimental study to clearly demonstrate the pivoting effect was, to our best knowledge, the one from Poelma *et al.* (2007). However, a direct comparison is difficult as these authors considered spatially decaying turbulence at maximum $Re_\lambda \approx 29$.

The vertical velocity structure functions (figures 3.27c,e) display the same behavior as their horizontal counterpart (figures 3.27b,d), suggesting that the turbulence responds to the presence of the particles in similar ways in both directions. It is indeed verified that the anisotropy ratio u'_x/u'_z is not significantly affected by the particles. Poelma *et al.* (2007) and Frankel *et al.* (2016) found that particles enhanced the fluid velocity fluctuations aligned with gravity compared to the transverse ones, whereas in
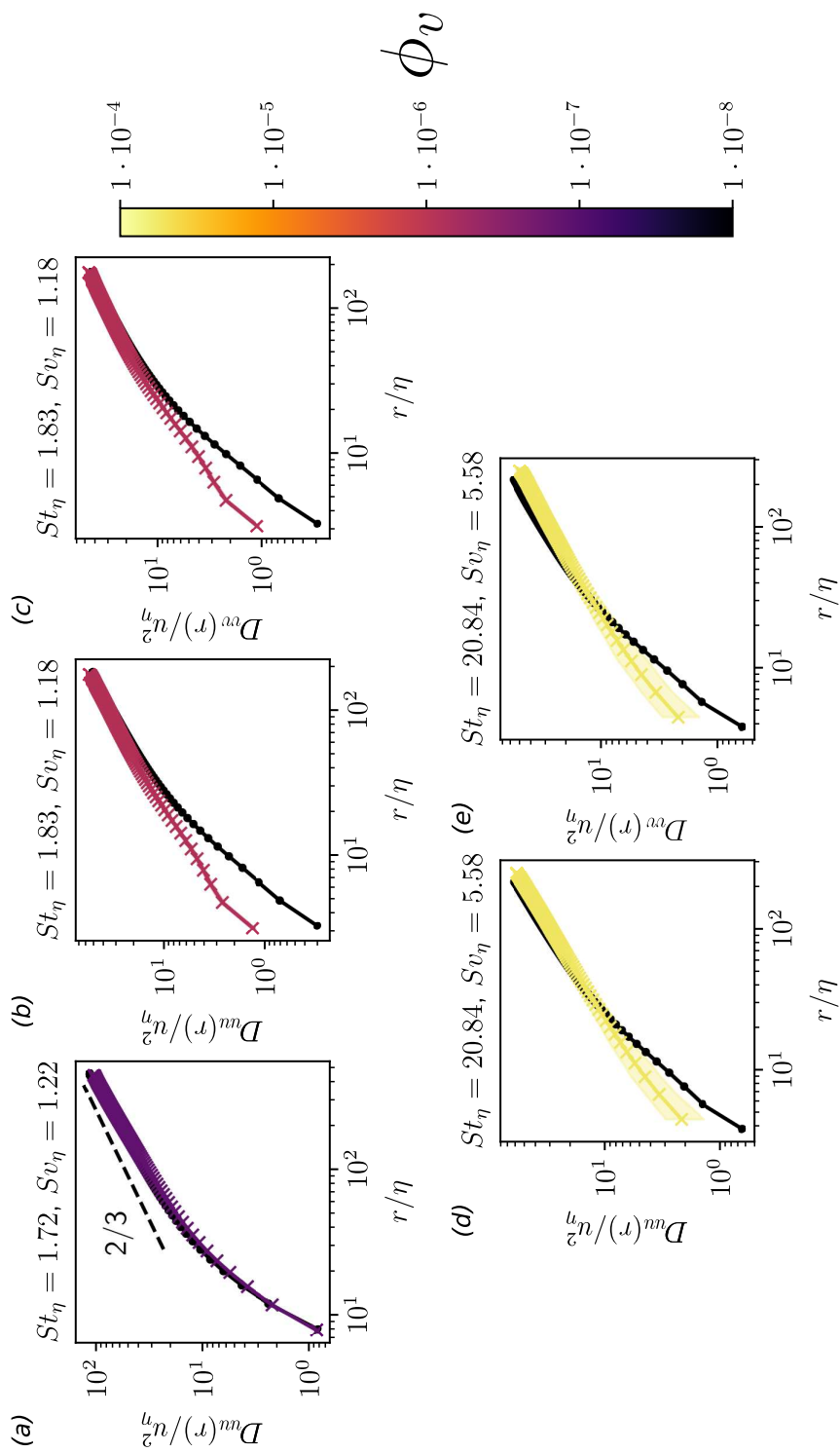
Figure 3.27: Horizontal (a,b,d) and vertical (c,e) longitudinal structure functions for laden (color-coded by volume fraction) and unladen (black) multiphase flows. The shaded regions represent 95 % bootstrap confidence bounds.

Hwang & Eaton (2006b) the level of isotropy was marginally influenced even at particle mass loadings that heavily modulated the turbulence intensity. Among these studies, Hwang & Eaton considered a much higher Reynolds number ($Re_\lambda \approx 240$), comparable to the present study. One may conjecture that the wide range of scales allows for a redistribution of the energy among the different components; certainly, further studies that systematically investigate the role of Re_λ are needed.

Even for the higher volume fractions, the changes in the fluid turbulence intensities in both vertical and horizontal directions (not presented) are scattered within the measurement uncertainty, with no consistent trend in terms of St_η, Sv_η, or ϕ_v. This suggests that the turbulence augmentation/attenuation, over different scales and from different mechanisms, largely compensate each other, at least in the considered range of parameters. On one hand, particles increase the overall inertia of the mixture and locally enhance the dissipation around them, modulating the turbulence; on the other hand, the drag force exerted by the falling particles perturbs the fluid an excites the turbulence (Balachandar & Eaton, 2010). Both effects are amplified for larger and heavier particles (which provide higher loading, distort more the flow around them, and shed more energetic wakes). For comparison, Hwang & Eaton (2006a) investigated particles with $St_\eta \approx 50$ settling in homogeneous turbulence and measured a reduction of r.m.s. fluid velocity of about $10 - 15\%$ for a mass fraction of 0.1 (close to the highest loading considered in the present measurements). The balance between opposing effects was demonstrated by measurements obtained in the same facility in micro-gravity (Hwang & Eaton, 2006b), where the turbulence modulation was found to be greater than in the fixed laboratory frame. Hwang & Eaton (2006b) also compared their laboratory results against DNS studies which showed significantly smaller turbulence attenuation. While this suggested that the point-particle approach used in the simulations missed important physics, the DNS were also at significantly smaller St_η, between 1 and 11 and comparable to the present cases.

Chapter 4

Dynamics of Settling Particle Plumes

In this chapter we discuss a flow where the particles are not only in the turbulence, they actively drive it through buoyancy. Instead of being sparsely dispersed homogeneously within the flow, in this case the particles are more densely packed and concentrated inhomogeneously. Specifically, we conducted experiments on dense suspensions of inertial particles falling in a quiescent ambient environment, forming particle plumes. Plumes fall into the same family of flows as jets–shear flow where one fluid moves through another. Although the flows we studied were driven by particles, multiphase plumes/jets can be driven by any dispersed phase: bubbles, droplets or particles, and the density difference between the ambient fluid and the mixture of fluid and dispersed phases is the source of buoyancy. This mixture bulk density, ρ_b is a function of the disperse-phase volume fraction:

$$\rho_b = \phi_v \rho_d + (1 - \phi_v)\rho_f \tag{4.1}$$

where, as before ϕ_v is the disperse-phase volume fraction, and ρ_d and ρ_f are the densities of the disperse phase and the continuous phase fluid respectively. The initial momentum of the multiphase plume or jet depends not only on the initial mixture density, but also the velocities of the dispersed and continuous phases and the relationship between these two sources determines the flow's classification. Whether single or multiphase, jets are driven mainly by their momentum, whereas plumes are driven by buoyancy. There are also forced plumes, also known as buoyant jets, forced by a combination of momentum and buoyancy, and the multiphase plumes we studied fall into this last category. No matter the driving force, plumes and jets are often turbulent, and excellent at mixing their contents with their surroundings. They do so through entrainment–the process of engulfing air from the surrounding environment. This mixing can be seen as often one observes energetic, turbulent motions a the plume edge. These billows–covering a wide range of temporal and spatial scales–are responsible for diluting and spreading the plume as well as well-mixing the body of the plume with the ambient.

Turbulent multiphase plumes are common throughout the natural and human environment, comprising some of the most dramatic and violent flows on Earth. Volcanic eruptions for example are mixtures of hot gas and ash particles, driven both by the buoyancy of the mixture and the initial momentum of the explosion. Ash and glass particles often settle out of the resulting plume and umbrella cloud via convective particle-driven instablities (Carazzo & Jellinek, 2013; Scollo *et al.*, 2017) forming multiphase plumes. The particles in these plume settle much faster than they would individually, and the lack of understanding of their dynamics undermines the accuracy of volcanic ash transport and dispersal models, with differences in field data and model results differing by up to 150% (Scollo *et al.*, 2008). Sediment deposits in lakes were theorized to be affected by multiphase plumes back in 1965 by Bradley (1965) to explain discrepancies between predicted Stokes settling and field observations. The same has been theorized of marine tephra layers which seem to deposit much faster than predicted by individual particles settling under Stokes' Law (Manville & Wilson, 2004). Hydrothermal vents on the seafloor create multiphase plumes composed of hot water, metalliferous sediments and dissolved chemicals often rising hundreds of meters, transporting their contents and mixing them throughout the ocean water column (Carey *et al.*, 1988; Carazzo *et al.*, 2013) Multiphase plumes are even theorized inside the Earth's crust where low-density magma replenishes basaltic magma chambers, with implications for geologic deposits (Carey *et al.*, 1988).

Better understanding turbulent multiphase plumes will not only allow us to better understand our planet, but how our actions affect it, and potentially how we can better protect it. Another violent and dramatic multiphase plume was the Deepwater Horizon oil spill in 2010, where a blowout during drilling of a deepwater well led to 5 million barrels of oil spilling out into the Gulf of Mexico, along with indelibly harming the gulf environment and marine life. Many of the ways humans interact and alter the environment involve multiphase plumes: dredging operations, discharge of industrial and

urban waste, pulverized coal combustion, dust emission from mining operations, transport of grain, and many more (Liu, 2003; Hall *et al.*, 2010). We may even use multiphase plumes in our efforts to mitigate climate change. Carbon sequestration can involve injecting carbon dioxide at the ocean floor, forming multiphase plumes that dissolve the carbon dioxide into the water (Alendal & Drange, 2001). While these applications and occurences are vastly different, they share physics and understanding the dynamics of one can translate to the others. However our collective understanding of turbulent multiphase plumes is still relatively limited, especially compared to single-phase ones.

Our quantitative understanding of turbulent plumes starts in the late 1930s and early 1940s with the studies of Zeldovich (1937); Schmidt (1941a,b), who derived similarity solutions for steady plumes. Morton *et al.* (1956) published a seminal paper which developed an integral model based on conservation of mass, momentum and buoyancy with a few key assumptions. They assumed that the entrainment of fluid into the plume was constant throughout the plume length, and could be related to the plume velocity by a constant such that $u_e = \alpha w$ where u_e is the entrainment velocity, w a characteristic plume velocity (such as the centerline velocity) and α is called the entrainment coefficient. This assumption was first proposed by Taylor (1946) for the case of convection currents in the atmosphere. Morton *et al.* (1956) further assumed that the plume was self-similar (inspired at least in part by Batchelor (1954, Batchelor's (1954)) expressions for mean velocity and temperature profiles also in convection currents) and axisymmetric. Finally they also assumed that the density difference between the plume and the ambient can be ignored, e.g. that $\rho_b \approx \rho_f$ where ρ_b and ρ_f are the bulk plume density and the density of the ambient fluid respectively (called Boussinesq plumes). Those three assumptions simplified the coupled system of nonlinear partial differential equations subject to complicated boundary conditions into a system of ordinary differential equations–easily solved given the initial plume conditions. Morton *et al.* (1956, Morton's (1955)) theory forms the basis of "classical" plume theory which has been revised and

improved upon, with the inclusion of non-Boussinesq plumes, where the density difference is significant (Morton, 1959; Ricou & Spalding, 1961; Rooney & Linden, 1996; van Den Bremer & Hunt, 2010), but remains as the standard in the literature for modeling turbulent plumes.

Morton (1959) (later Hunt & Kaye (2001); non-Boussinesq case Carlotti & Hunt (2005)) also introduced a nondimensional plume number Γ_0, essentially a plume Richardson number, to relate the relative strengths of the momentum, mass and buoyancy fluxes at the plume source and is given by:

$$\Gamma_0 = \frac{5B_0 Q_0^2}{8\alpha\sqrt{\pi}M_0^{5/2}} \tag{4.2}$$

where B_0, Q_0 and M_0 are the source buoyancy $(= \pi g(1 - \rho_b/\rho_f)wb^2)$, volume $(= \pi wb^2)$ and momentum flux $(= \pi\frac{\rho_b}{\rho_f}w^2 b^2)$ respectively and where b is the plume radius. This plume function provides convenient classification for plumes: fountains $(\Gamma_0 < 0)$ i.e. negatively buoyant jets driven by an initial momentum directed against gravity, pure jets driven by momentum $(\Gamma_0 = 0)$, forced plumes driven by a mix of momentum and buoyancy $(0 < \Gamma < 1)$, pure plumes $(\Gamma_0 = 1)$ and lazy plumes $(\Gamma_0 > 1)$ characterized by an excess of buoyancy with respect to momentum. Caulfield (1991) and Hunt & Kaye (2005) extended Γ as a function of axial distance z from the source such that:

$$\Gamma(z) = \frac{5B(z)Q(z)^2}{8\alpha\sqrt{\pi}M(z)^{5/2}} \tag{4.3}$$

The well known solutions for pure plumes lead to decay rates for the velocity and concentration of $-1/3$ and $-5/3$ respectively (see eqs. 4.16–4.18). While both forced and lazy single-phase plumes asymptote to pure-plume behavior in the far field, their near-field behaviors are unique. Forced plumes expand more rapidly than pure plumes, transitioning from jet-like to plume-like behavior as evidenced by the plume function monotonically increasing wit axial distance and converging to $\Gamma(z) = 1$ (Hunt & van den

Bremer, 2010). Lazy plumes on the other hand, initially contract and accelerate before expanding and slowing down, with their plume function monotonically decreasing–also asymptotically converging on pure plume behavior with $\Gamma = 1$.

These insights into single-phase plumes have informed much of our understanding of multiphase plumes, and often are used in modeling flows like volcanic eruptions (Fagents *et al.*, 2013). However, it is not trivial to suggest that integral models based on Morton's work translate directly to multiphase plumes. The disperse phase is coupled to the continuous phase flow, and the slip velocity between the two phases as well as the concentration can affect the plume entrainment and mixing (Parthasarathy & Faeth, 1987). For example, one of the fundamental Morton assumptions, that of self-similarity, was shown to not hold for bubble plumes by Bombardelli *et al.* (2007), as it evolves with a characteristic length scale, which is a function of the bubble slip velocity and buoyancy flux.

Using the foundation of the three Morton assumptions, single-phase integral models were extended to bubble plumes by citetDitmars1975,Milgram1983,Sun1986 with the important inclusion of the bubble slip velocity. LES simulations of bubble plumes have been conducted in both the two-way (Mudde & Simonin, 1999; Deen *et al.*, 2001; Dhotre & Smith, 2007) and four-way coupled regimes (Delnoij *et al.*, 1997). The thesis of Marjanovic (2018) explored direct numerical simulations of forced, pure and lazy bubble plumes. Interestingly, the bubbles plumes (whether forced, pure or lazy) shared some characteristics with lazy-single phase plumes–notably the width contraction and initial velocity acceleration before entraining back to a self-similar solution. Lazy multiphase plumes instead differentiated themselves by rapid mixing after the source and a significantly larger maximum velocity. On the experimental side, empirically derived closure schemes have provided better predictions of bubble plume dynamics (Lance & Bataille, 1991; Risso & Ellingsen, 2002; Mercado *et al.*, 2010; Alméras *et al.*, 2017).

Less present in the literature are particle plumes, which have some fundamental

differences with bubble plumes whose disperesed phase is less dense than the ambient fluid and less inertial. Figure 4.1 illustrates the structure of a generalized particle plume. Black indicates particle-phase quantities, such as bulk density, velocity and width while blue indicates the fluid phase quantities which are governed by separate, but coupled conservation equations. The rest of the chapter will follow the coordinate and labeling conventions as presented in this illustration. Carey & Sparks (1986) experiementally studied buoyant particle plumes, specifically relating them to the growth and collapse of volcanic plumes. Mazurek *et al.* (2002) photographed sand-laden jets and found they spread linearly, and their growth rates increased as the ratio of the source momentum flux to the the buoyancy flux increased. Liu (2003); Liu *et al.* (2007) studied dense particle plumes falling in air and was able to measure both the air and particle velocity profiles, along with other characterstics like the spread rate and compared these values to an integral model formulation. Jiang *et al.* (2005) suggested that the vertical particle-phase velocity (w_p) is a sum of the fluid phase velocity (w_f) and a slip velocity for dilute particle concentrations. This slip velocity is indicated in figure 4.1 by the difference between the profiles of w_f and w_p. The sand and slurry jet experiments of Hall *et al.* (2010) found that the fluid phase velocity and particle concentration could be represented by self-similar Gaussian profiles. They also measured centerline concentration and velocity as well as spread rate and momentum fluxes. The thesis of Taub (2013) explored a forced multiphase plume experimentally, focusing on the decay rate of centerline variables and the assumption of a constant particle settling velocity. Lai *et al.* (2016) developed an integral model for particle plumes based on a spreading hypothesis rather than the classic entrainment hypothesis and compared their model to past experimental studies.
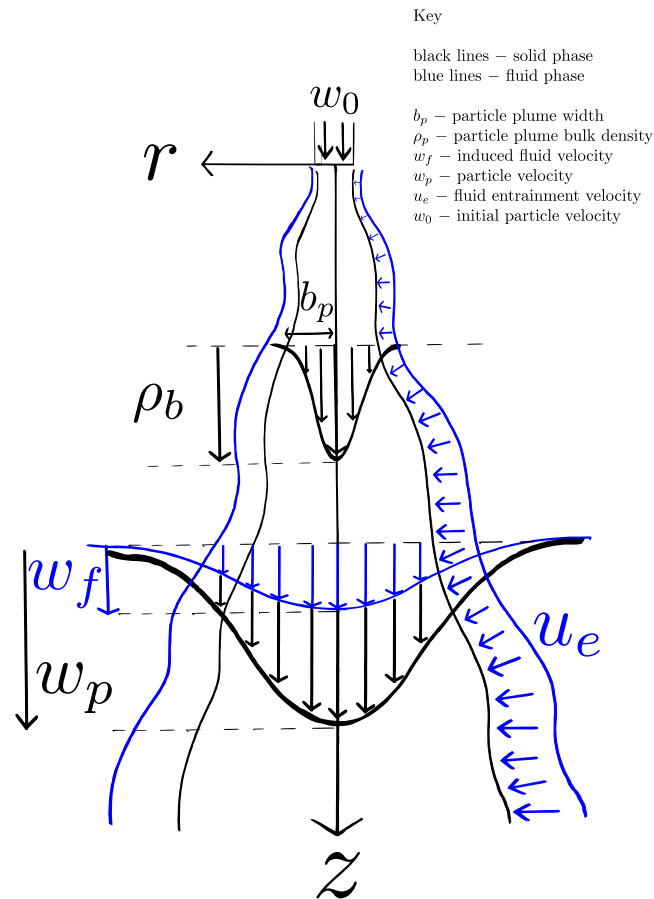
Figure 4.1: Particle plume falling through a quiescent environment with relevant variables.

4.1 The Plume Experiment

To enhance our understanding of particle plume dynamics, we took an observational approach, imaging the plumes to measure their behavior. The goal of our experiments was to compare the dynamics of particle plumes with different initial mass fluxes falling into a quiescent environment. We wanted to both capture the dynamics of the plume itself–the velocity, concentration and spreading–and the induced air flow, particularly the entrainment velocity into the particle plume. We measured the plume

properties via high-speed imaging over a large window. In order to revolve the relevant scales of air entrainment at the particle plume boundary, we performed a separate set of measurements with a higher resolution.

4.1.1 Setup and Plume Initial Conditions

We again used the same turbulence box, which conviently provided a large, controlled test-section for the particle plumes to fall into. This was key for a few reasons. The first is that to capture the plume evolution with streamwise distance from the outlet, the plume needed room to fall for a significant distance compared to its initial diameter. In our turbulence box, we were able to image the plume over 1.5 m of vertical distance which when compared to our chute size, D_0 of 1.905 cm, came out to an observed plume length of $z/D_0 \approx 75$. Secondly, the nearly 5 cubic meters of volume ensures that our plumes are not affected by any interactions with the walls. In our case, even at the widest spread, our plumes are always at least 0.25 m or more from the walls of the turbulence box.

Figure 4.2 shows a schematic (not to scale) of the experimental setup. A high speed laser (Photonics Industries, DM30 Series, 80 mJ) sits on top of the turbulence box, and the beam is redirected by two Thorlabs Nd:YAG laser mirrors and spread into a sheet with a cylindrical lens to illuminate the $x - z$ symmetry plane of the box. The laser sheet was approximately 3 mm in thickness at the center of the chamber. We used two high-speed CMOS cameras (Phantom VEO 640L), synchronized with the laser.

As figure 4.2 shows, the chamber ceiling has an opening connected to a 3 m vertical chute (1.9 cm in diameter, at the top of which is a resevoir of 30 μm glass particles. The properties of these particles used are the same as in table 3.2 in Chapter 3. Those particles were fed by gravity at a steady rate, through a nozzle at the bottom of the resevoir. These nozzles are interchangable threaded inserts, and by changing the
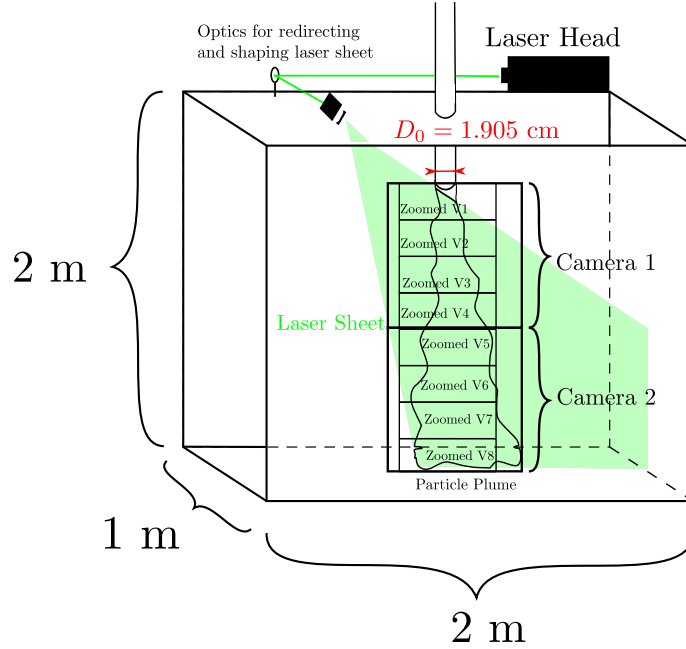
Figure 4.2: Schematic of the turbulence chamber and laser-sheet setup for the particle plume experiments. The bounding boxes around the plume represent camera views taken of each plume. Two, labeled Camera 1 & 2, image the whole plume, while 8 views are zoomed in to image the surrounding air flow.

nozzle size, we could systematically vary the mass flow rate of particles, which corresponds to the initial plume concentration. Using the following equation (Nedderman, 1992) we could use the initial mass flow rate to estimate the initial plume concentration when planning the experiments:

$$\dot{m}_p = C\rho_b \sqrt{g} \left(D_0 - kd_p\right)^{2.5} \tag{4.4}$$

where C is a function of the friction coefficient (taken here to be 0.64), ρ_b is the bulk density (related to the packing factor, taken here to be $0.6\rho_p$), D_0 is the nozzle diameter, d_p is the particle diameter and k is a shape factor equal to 1.5 for spheres. To obtain

a finer estimate, we used a digital scale collected the output particles to log the time-resolved weight of the released particles. Because we conducted the plume experiments multiple times for each flow-rate setting it was important to ensure the mass flow rate was repeatable. To that end we measured the mass flow rate multiple times, the mean and its uncertainty for each nozzle is listed in table 4.1. Table 4.1 also lists the estimated initial vertical velocity and volume fraction, though we do not directly measure these. Details on how they are estimated are reported in section 4.2.2.

Plume	$\dot{m}_p$ [g/s]	$W_0/\tau_p g$	$\rho_{b,0}/\rho_f$	$\phi_{v,0}$
P_1	1.42 ± 0.21	9.6	7.17	2.4e-3
P_2	2.99 ± 0.22	2.1	68	2.6e-2
P_3	8.04 ± 1.2	3.0	128	5e-2

Table 4.1: Initial mass flow rates for the three particle plume experiments in this study along with the estimated initial vertical velocities and bulk densities (see section 4.2.2 for details on how these were estimated).

The goals of these experiments required imaging the plume over the full height of the measurement chamber, nearly a meter and a half, while also imaging the air flow around the plume. Measuring both simultaneously required two separate campaigns, one for imaging the particle plume itself, and another for capturing the flow around it. To image the inertial particles, we positioned the two cameras with 50 mm focal length Nikon lenses such that each captured about 75 cm in vertical distance (with a little overlap). These views are represented in figure 4.2 by the solid bounding boxes around the particle plume, labeled Camera 1 and Camera 2. To image the air entrainment process, we conducted separate experiments with higher resolution and eight vertically stacked camera views, slighly overlapping with each other, labeled as Zoomed V1 through Zoomed V8 in 4.2. The chamber was seeded with 1–2 μm DEHS droplets ain order to image the air flow motion, and illuminated by the laser. We were able to image the whole 1.4 m length of the plume, now resolved sufficiently to measure the air

flow around the plume boundary. Imaging properties for both experiments are listed in table 4.2.

Experiment	# cameras	lens	resolution	field of view	frequency	# frames
Plume	2	50 mm	3.5 pixels/mm	30 x 146 cm^2	600 Hz	19949
Air entrainment	8	200 mm	15 pixels/mm	11 x 17 cm^2	300 Hz	12471

Table 4.2: Imaging settings for plume and air entrainment experiments.

4.1.2 Velocity Measurements

PIV was again our tool of choice to measure velocity in these experiments, and the same PIV algorithm as in chapter 3 was used with interative window offset and deformation (Nemes *et al.*, 2015). For the plume velocimetry, instead of correlating images of individual particles, the algorithm correlated patterns in the plume. Figure 4.3(a) shows an example raw image while (b) and (c) show zoomed-in views of the pattern correlated by PIV between successive frames. PIV was processed with an interative 96x96 to 48x48 refinement with 50% overlap, and thus a 24 pixel vector spacing. The mean pixel displacement obviously varies in the plume in the streamwise and spanwise directions, but generally the maximum displacement was around 10-12 pixels. Figure 4.3(d) shows the resulting instantaneous PIV velocity field. The common estimate of the PIV bias error (± 0.1 pixel, Raffel *et al.* (2018)) is not necessarily applicable to the present case, in which patterns are correlated rather than individual particles. To estimate the pixel-displacement uncertainty, we artifically transformed 1000 images with a known gaussian shift, and then reprocessed the shifted images. The mean pixel-displacement uncertainty was 0.1 pixels, with a standard deviation of 0.06 pixels. This is almost certainly optimistic, since the same shift was applied to the whole image, not representative of a turbulent motion. We therefore expect that the bias error to be

somewhat larger, so we conservatively assumed a 0.5 pixel bias error, which figures into $5-15\%$ error on the displacement. The exact percentage depends on the location in the plume, as centerline displacements are greater than those at the edges. To estimate the random error due to finite sampling, we calculated a turn-over-time scale (τ_t of the plume as the plume half-width (b_p) over the centerline velocity ($\tau_t = b_p/W_c$). We used this time scale to approximate the number of independent realizations in each experiment, which falls between $500-900$ realizations depending on the plume and the streamwise location. Using only independent realizations, mean and r.m.s. velocities were converged with some uncertainty, with the random error estimated to vary between 3% and 7% depending on the streamwise plume location.
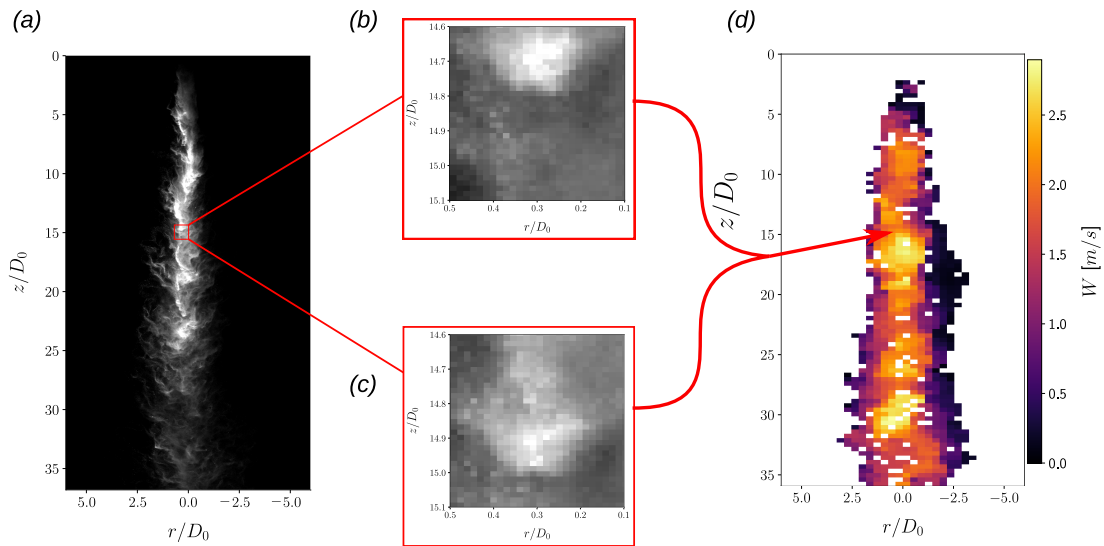
Figure 4.3: (a) Example raw image of the particle plume. (b) and (c) show an example of the patterns correlated between frames by the PIV algorithm. (d) shows the resulting instantaneous vertical velocity map, with rejected vectors and vectors outside the plume blanked out in white.

Measuring the fluid velocity involved more traditional PIV, but still with some complications. Larger, more reflective and highly concentrated, the inertial particles

making up the plumes outshined the small DEHS tracer droplets. Making out the tracers thus required opening the camera aperature and increasing the laser power enough that the small particles could be seen by the camera. This resulted in the inertial particles appearing oversaturated, which made it easy to discriminate between inertial particles and the tracers. As in the dilute experiments (see section 3.2), we used a similar separation algorithm based off intensity and size. This version differed in that when replacing inertial particles with Gaussian noise, it used a local mean and standard deviation. This was necessary, because unlike the dilute experiments, the image intensity was not homogenous over the field of view. A moving 50x50 pixel^2 window was used to calculate local intensity statistics for tracer separation, which was chosen because it balanced a few considerations best: the size of inertial particles in the field of view, which is $3 - 6$ pixels^2, as well as the gradient of background noise intensity.

After image separation, we did background substraction as in section 3.2 and then continued performing PIV on the tracers, processing with 64x64 to 32x32 window refinment, again with 50% overlap. Figure 4.4 summarizes the procedure for processing the tracer images. The typical tracer displacement was approximately 5 pixels. Similarly to our plume velocity vectors, since the datasets were time-resolved, the number of independent frames was less than the total. Using the same time-scale as in the inertial particle PIV, the number of independent realizations ranged between 1000 and 1800 with the random error from the finite sample size ranging from 2%−4%.

4.1.3 Calculating Plume Width & Spread

To extract the plume width, we use the time-averaged raw images of the particle plumes. Previous plume studies (Lai *et al.*, 2016) have relied on the observation from Bernard & Wallace (2002) that the scattered light intensity varies linearly with particle concentration for monodisperse particles. We therefore use the image light intensity as a proxy for local particle concentration, allowing us to calculate the particle concentration
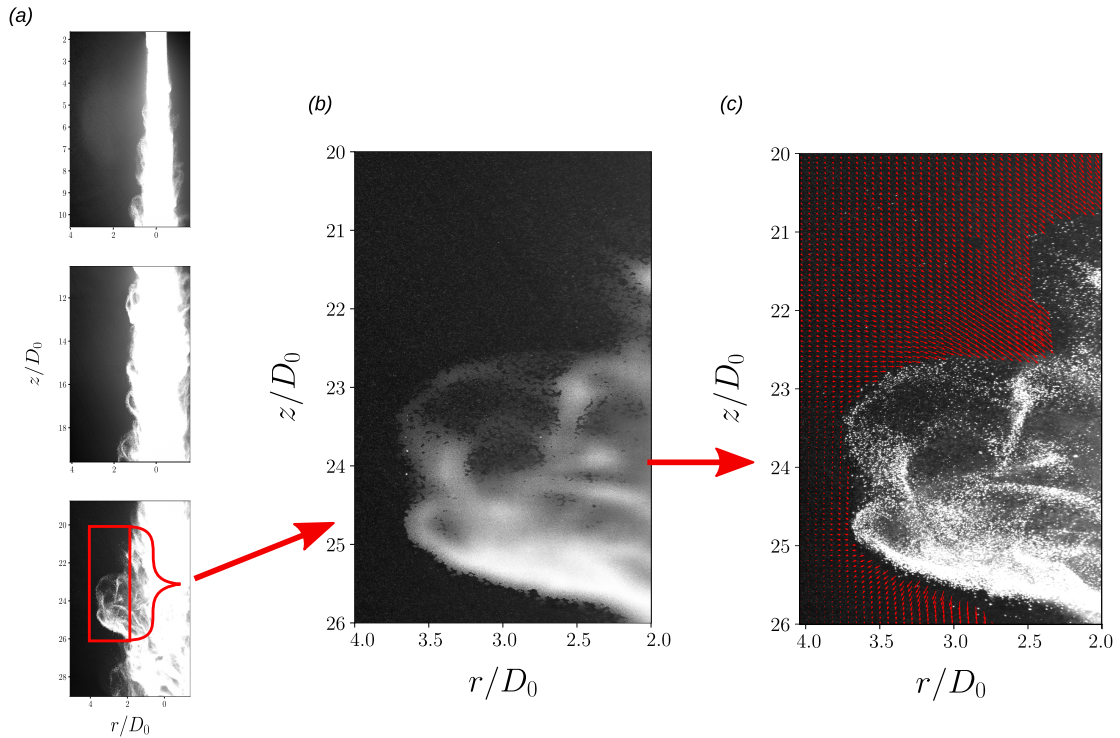
Figure 4.4: (a) Example raw images of the tracers for the first three camera views. (b) Section of camera view three after separation algorithm is applied. (c) Resulting instantaneous velocity over the raw image.

profiles across the plume cross-section. The light intensity vary significantly with axial distance, as the laser sheet continually darkens with distance from the optics shown in figure 4.2, making conversion to an absolute concentration unreliable.

One complication arose due to the particles themselves blocking out light. As shown back in figure 4.2, the laser sheet illuminates the plume from the left side. For the densest plume, P_3, as the plume exits the chute, it is dense enough that the edge blocked transmission of light to the rest of the plume. This results in local concentration profiles with non-symmetric peaks closer to the side first illuminated by the laser until $z/D_0 \approx 20$, when the plume dilutes enough to let the laser sheet through and the horizontal intensity profile become symmetric as expected. Fortunately for the two other

plumes, P_1 and P_2, the situation was less severe, and the plumes are better illuminated through their cross sections by $z/D_0 = 5$. We estimate the error associated with light attenuation by comparing the concentration profiles from the positive and negative r-axes. Gaussian widths obtained from each side vary only by approximately 4% past $5z/D_0$ for plumes P_1 and P_2 and $20z/D_0$ for plume P_3, whereas before those limits, the difference reaches 25%. Subsequently, we limit our analysis of the local relative concentration profiles to the regions the error was relatively small.

4.2   Mean Plume Characteristics

In this section, we explore the time-averaged behavior of the particle plumes–whether they are self-similar, how the centerline concentration and bulk density changes with height, and the spreading rate of each plumes' particle phase. Figures 4.5a and 4.5b show a split-view of the time-averaged images (brightness indicating relative concentration) and the mean velocity magnitudes (normalized by their maximum) fields for the three plumes. We use these time-averaged maps to calculate centerline and radial velocity profiles, as well as concentration profiles and the time-averaged plume width.
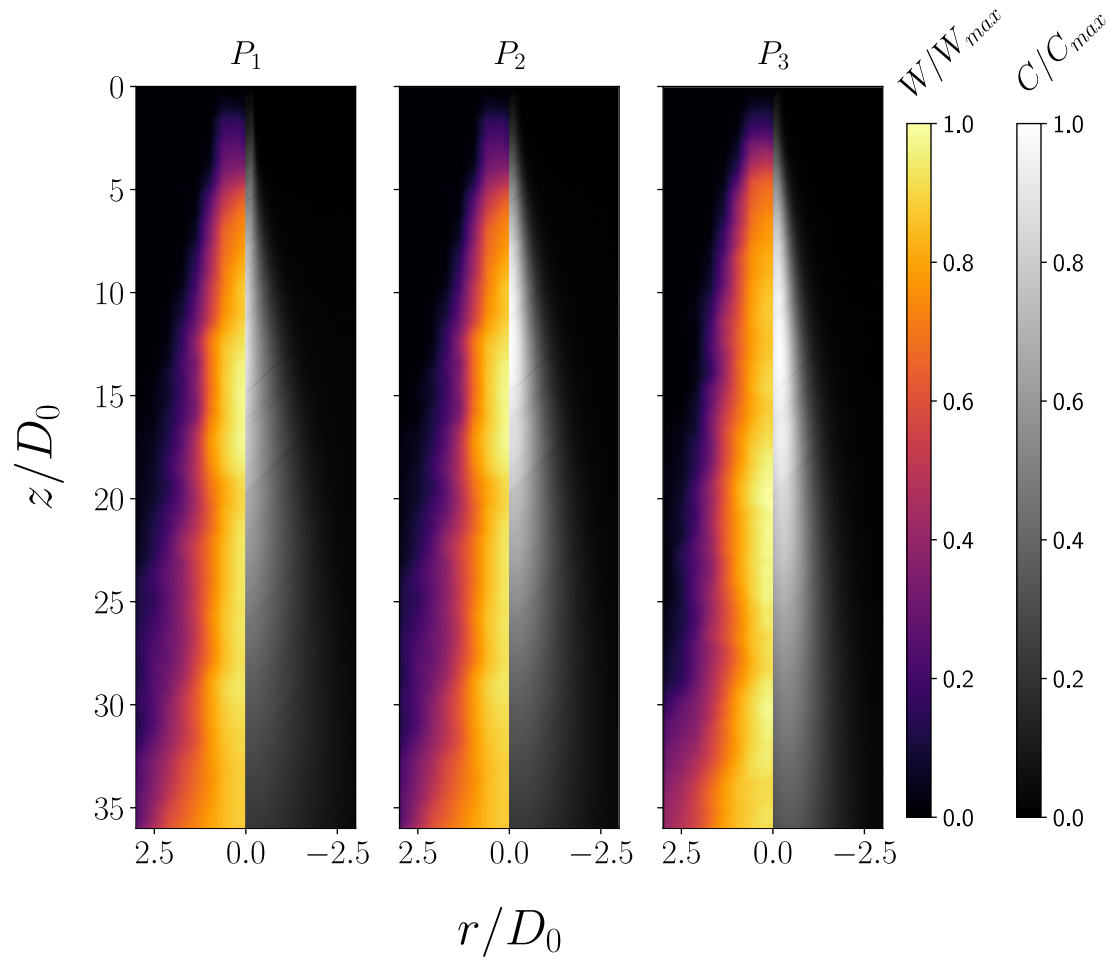
(a) Upper camera view
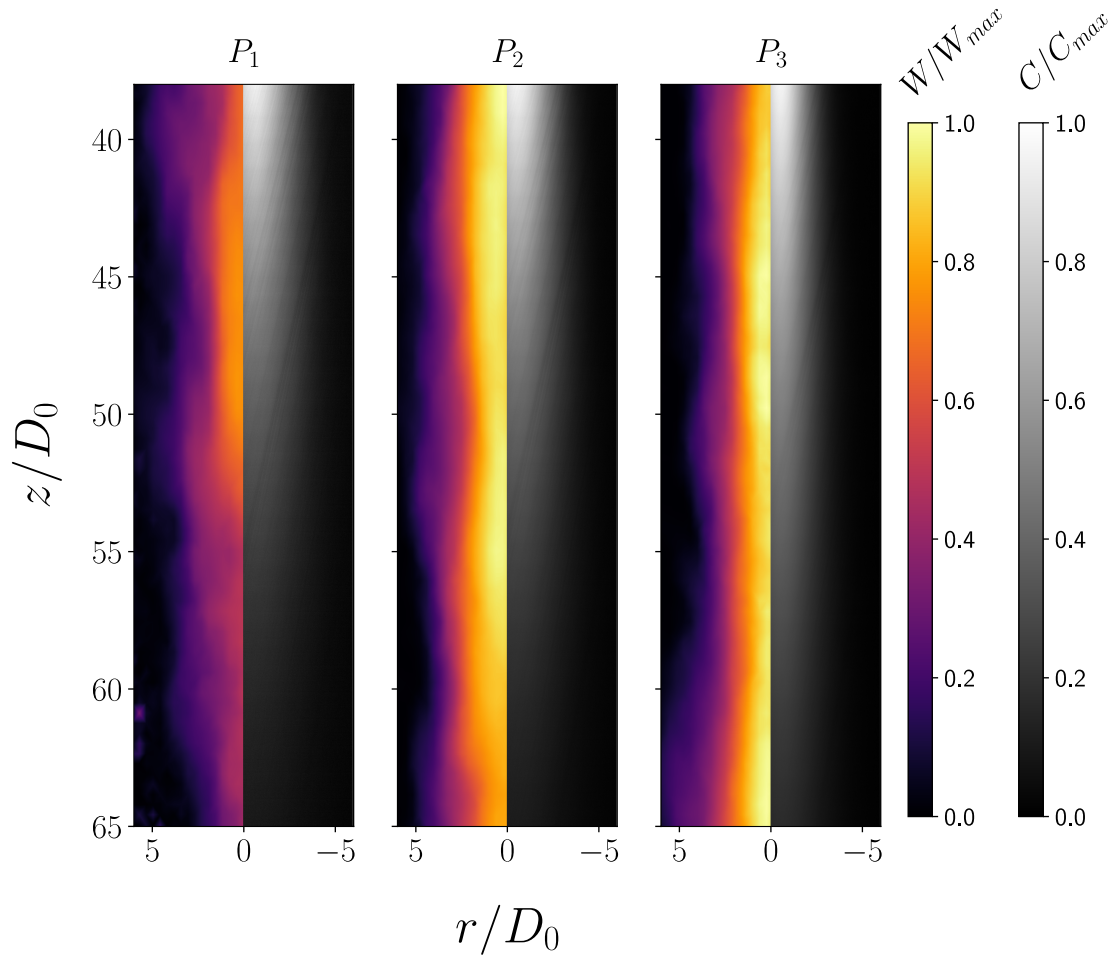
(b) Lower camera view

Figure 4.5: Time-averaged velocity magnitude (right) and relative concentration, normalized by their respective local maximums for the upper (a) and lower (b) cameras view.

4.2.1 Self Similarity

Going back to Morton *et al.* (1956), the formulation of plume conservation equations have generally relied on a few important assumptions. Although Morton originally formulated and solved these equations for single-phase Boussinesq plumes from point

sources, many non-boussinesq and even multiphase plume models share these assumption: perhaps most importantly, the that these plumes are self-similar–that is, their profiles of velocity and concentration collapse at all axial locations when appropriately re-scaled. As mentioned previously, in Morton *et al.* (1956), self similarity shows up in the entrainment assumption–that the radial entrainment velocity at the edge of the plume is proportional to the characteristic vertical velocity of the plume through a constant, which is independent of height. An alternative to the entrainment assumption is the spreading hypothesis, which specifies the plume spreading rate to close the system of plume equations (Wood *et al.*, 1993), but this too requires self-similarity: the spreading rate is assumed to be independent of height. This assumption of self-similarity however developed out of the analysis of single-phase plumes and there is no promise that the same holds true for multiphase ones.

Most commonly in modeling, the horizontal variation of time-averaged vertical velocity and bulk density (or concentration) are described with Gaussian profiles in axisymmetric plumes such that for a given height:

$$w_f(r) = w_c e^{-r^2/b^2}; \quad c = c_c e^{-r^2/b^2} \tag{4.5}$$

where r is the radial distance from the plume centerline (as shown in the coordinate system of 4.1), w_c and c_c are the centerline velocity and concentration respectively and b is the plume width. Also common, especially for reducing models to a single dimension, are top-hat profiles, though the two can be related (often, though not always, by taking the top-hat to be half the Gaussian-centerline variable, e.g. $w_{avg} = w_c/2$). No matter how the plume is modeled though, when models are compared to experimental plumes, Gaussian profiles often fit quite well to the observations (Turner (1979); Ramaprian & Chandrasekhara (1989); Shabbir & George (1994) among others for single-phase plumes, Seol *et al.* (2007) for bubble plumes, Hall *et al.* (2010); Carey *et al.* (1988) for particle plumes/jets.

One way to identify self-similarity is to examine the horizontal profiles of concentration and velocity at various vertical locations. Figure 4.6 shows the velocity and concentration profiles for plumes P_1, P_2 and P_3 scaled by the respective centerline value. Previous experimental studies (Hall *et al.*, 2010) used both the maximum value along the profile, or the the value at the geometric center, though for us as for Hall *et al.* (2010) these generally match. On the horizontal axis the radial distance from the centerline r is scaled by the half-width $r_{1/2}$, or the width at which the velocity/concentration drop to one-half their maximum. We do indeed observe reasonable collapse throughout the length of the plume, with shapes close to a Gaussian, lending some validity to assumptions of self-similarity for these multiphase plumes.
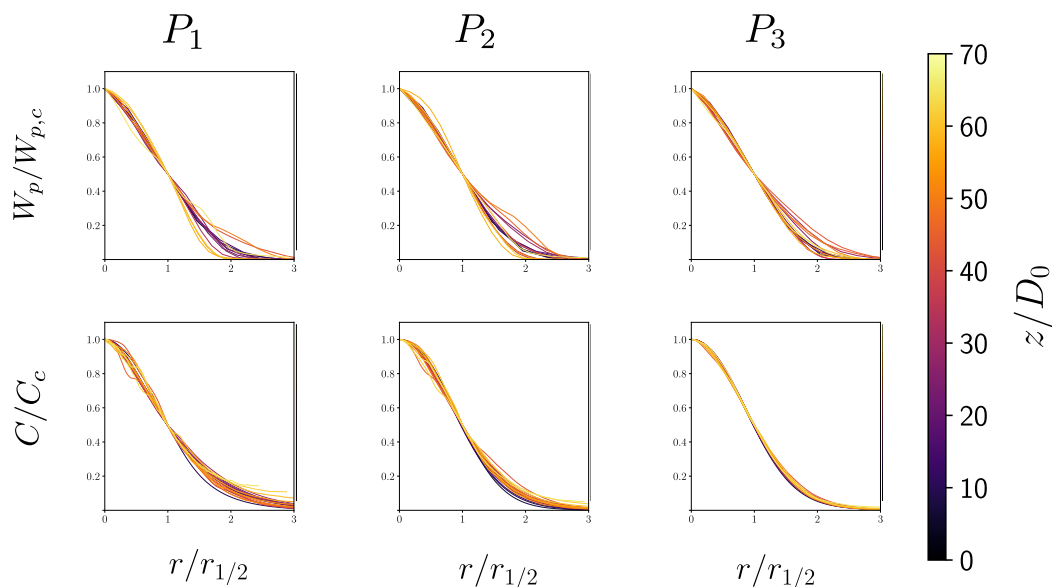

Figure 4.6: (top row) particle vertical velocity profiles scaled by the maximum (or centerline) value vs. radial distance from center, scaled by the half-width and (bottom row) particle concentration profiles scales by its maximum again vs. radial distance scaled by the half-width for each experimental plume. Colors represent vertical height, z/D_0 as indicated by the colorbar.

4.2.2   Centerline variables

We then look at the centerline observables in our plumes–the centerline velocity and width as a function of vertical distance. In figure 4.7, we plot the plume widths, as measured by the mean concentration profiles. We define the radius of the particle-phase of the plume b_p, to be the radius at which the particle concentration drops to $1/e$ of the maximum value, or roughly 36.8%. Lazy single-phase plumes are known to display necking, i.e. a narrowing of the plume width in the near-field development region, for example in the simulations of Marjanovic (2018) where the plumes contract between $0 - 2z/D_0$. Our plumes do not display this necking, although this could be due to our unbiased measurements not starting until $z/D_0 \approx 5$ for P_1 and P_2, and $z/D_0 \approx 20$ for P_3. However we notice that the half-width of the plume at the top of the unbiased imaging window is very close to the chute radius. Therefore if present, the necking must be relatively mild.

Interestingly, although all three plumes behave similarly until about $z/D_0 \approx 20$, they then diverge significantly. P_1, with the smallest initial mass flux begins to spread faster than the other plumes, followed by P_2 and then P_3, spreading the slowest. Calculating the slope of the approximately linear growth of plume radii between $z/D_0 = 20 - 60$, it becomes clear that the plume spreading rate, $\beta_p = db_p/dz$ decreases with increasing mass flux. For P_1, $\beta_p \approx 0.068$, while for P_2 it decreases to $\beta_p \approx 0.051$, and still further for P_3, down to $\beta_p \approx 0.032$. These spreading rates are generally lower than found in Hall *et al.* (2010), which ranged from $\beta_p = 0.08 - 0.1$. Lai *et al.* (2016) and Mazurek *et al.* (2002) considered particle plumes and found spreading rates more similar to ours, suggesting that the multiphase nature of the plume is responsible for this feature. Instead the particle-plume spreading rate seems to depend on the initial conditions, such as the initial mass flux.

The centerline vertical velocity is another important observable and figure 4.8 shows the results for the three plumes. Each of the three cases initially accelerated,
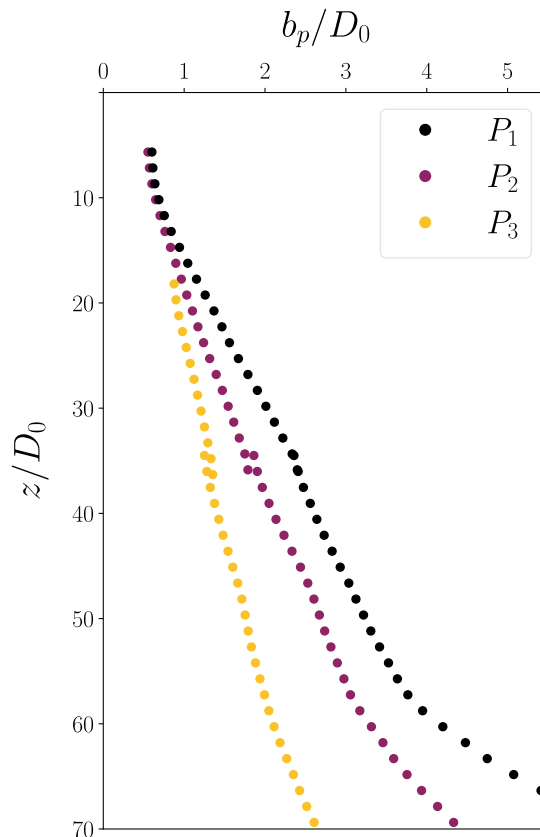
Figure 4.7: Plume radii, b_p, normalized by the chute diameter D_0. The respective spread rates (db_p/dz) for plumes P_1, P_2 and P_3 are 0.068, 0.051 and 0.032.

though again we are limited in our observations of the initial plume development region, and can only reliably draw conclusions for the velocity above $z/D_0 \approx 5$. This acceleration suggests that in the region beyond $z/D_0 = 5$, there probably is some contraction of the plume, as hypothesized above, and in the simulations of Marjanovic (2018). There is considerable uncertainty in P_3, partially due to convergence issues, and the total uncertainty on the mean velocity tops at 15% for this case, such that those oscillations are mostly within the uncertainty. Despite differences in the initial mass flux, there seems to be little difference between the maximum centerline velocity, which peaks for all cases around 30 times the Stokes settling velocity. After reaching this peak, the centerline

velocities in cases P_1 and P_2 slowly decay, with P_2 decaying slower than P_1. P_3, with all of its uncertainty taken into account, continues accelerating, or at least plateaus at a high velocity for an extended stretch–most of our experimental domain. Instead of differences in the maximum velocity, the plumes seem to differ on the vertical location where they reach their maximum velocity.
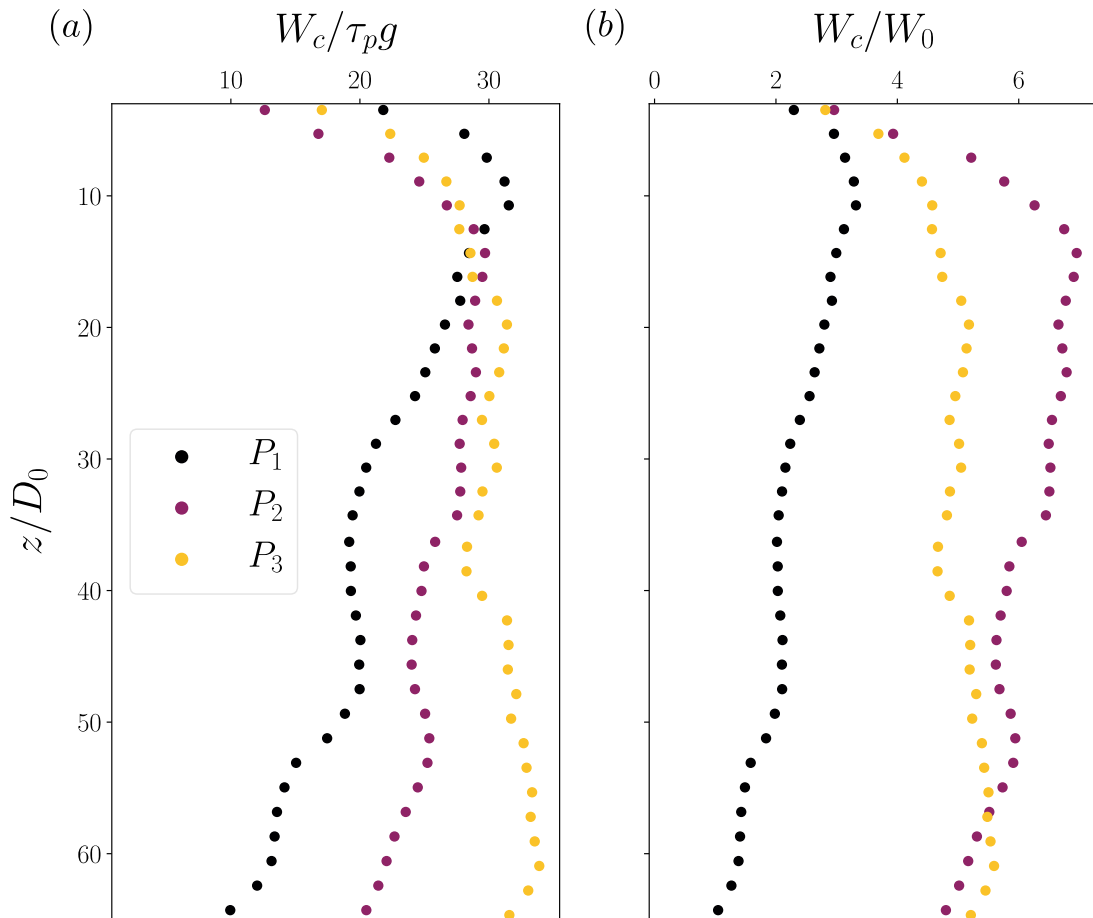
Figure 4.8: Plume centerline velocities normalized in (a) by the Stokes Settling velocity ($\tau_p g$) and in (b) by the source velocity at the outlet. While the three plumes accelerate to approximately the same absolute velocity (a), their relative maximum velocities with respect to their source velocities seems to depend on the initial conditions.

We quantify the differences between the plume decay rates by looking for a power-law relation between the centerline velocity and vertical drop distance, which is suggested by power-law arguments. Interestingly, it seems to be dependent on the initial mass flux. P_1 displays a gradual decay rate of -0.4, close to the $-1/3$ power-law trend for the velocity in a single-phase plume. Hall *et al.* (2010) observed a similar adherence to the $-1/3$ power-law behavior for their sand and slurry jets. Marjanovic (2018) saw similar behavior for the pure and forced plumes, whereas their lazy particle plumes decayed more slowly, an effect of the particle slip velocity continuing to generate momentum downstream. P_2 has a slower decay rate than P_1, with an approximate power-law dependence with a decay rate of -0.1. The densest plume, P_3, as discussed previously seems to be maintain a high velocity for a larger drop distance than the other plumes, and we do not observe a noticable decay.

Taken together, the trends in plume width and centerline velocity indicate a strong dependence of the behavior on the initial conditions, and more fundamentally, a stark contrast between the particle and single-phase plumes: denser plumes accelerate over much longer distances compared to single-phase lazy plumes. In the case of our densest plume, we do not capture a significant velocity decay after 60 diameters.

We use these centerline velocity profiles to get an estimate of the initial plume conditions: the initial average (top-hat) vertical velocity W_0 and initial average density $\rho_{b,0}$ and volume fraction $\phi_{v,0}$ listed back in table 4.1. For all the plumes, the initial velocity growth between $z/D_0 = 3.5 - 5$ seems relatively linear, and working under this assumption we extrapolate the centerline velocity to $z/D_0 = 0$. With these estimated initial velocities, we then apply conservation of mass. Using our measurements of the mean mass flow rate $\dot{m}_p$, and $b_{p,0}$ the initial plume radius, assumed equal to the chute radius, we solve $\dot{m}_p = \rho_{b,0} w_{p,0} \pi b_{p,0}^2$ for $\rho_{p,0}$, the average bulk density which we convert into a volume fraction via the relation $\phi_v = (\rho_f - \rho_b)/(\rho_f - \rho_p)$.
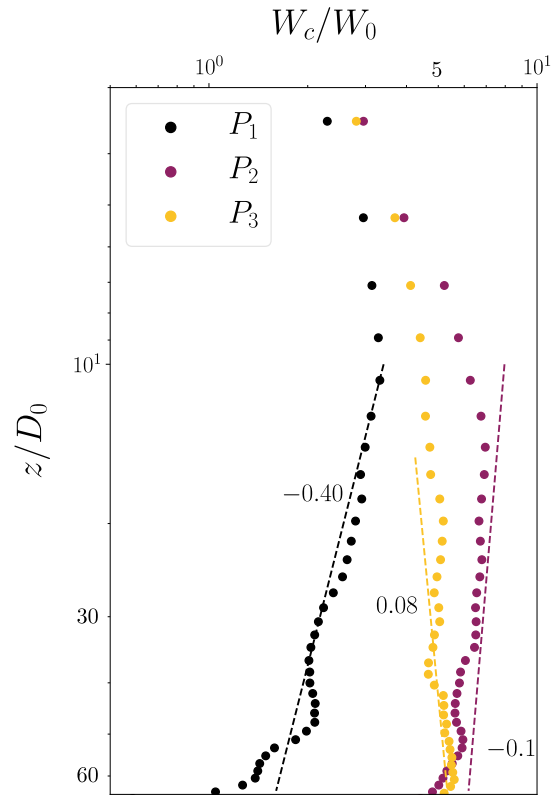
Figure 4.9: Plotted in log-log scale, the centerline velocity seems to follow approximately a power law with exponents indicated by the text.

4.3 Entrainment into Particle Plumes

As mentioned in section 4.1.2, we are able to image the ambient flow surrounding the particle plumes by zooming in on the interface separating the particles from their environment. However to calculate the entrainment velocity, u_e, into the plume required additional processing. First, we needed to define a plume boundary. Doing so involved dilating, thresholding and median filtering the raw images in such a way that the plume boundary followed the major billows and curves of the instantaneous images, while also extending into the field of valid PIV vectors. The dilation kernel was chosen so that the

boundary extended into the tracer field, and is typically the width of the PIV interrogation window ~ 50 pixels. This ensured that we did not underestimate the entrainment velocity as the gradient of the tracer velocity changes by a maximum of 10% per interrogation window, though the mean was approximately 3%. The median filter slightly smoothed out the boundary, so that it limited the effect of noise on the intricacy of the plume interface, and the filter size was also 1–2 interrogation window sizes. Figure 4.4 c) illustrates the result of this process, as we used the resulting image to mask the tracer PIV. The boundary between the masked and unmasked regions of that array define the plume boundary. After defining the plume boundary, we interpolated the tracer PIV at the boundary location. The final step was to calculate the component of the fluid velocity orthogonal to the local plume boundary. The angle of the local plume boundary relative to the velocity was determined by first using a small moving window of 5 boundary locations to define a line. With that line, we computed the fluid velocity normal to the local plume boundary. Finally, we averaged this entrainment velocity in time at each streamwise distance z to obtain the average entrainment velocity, shown for each plume in figure 4.10, with negative velocity indicating it is moving into the plume.

4.10 shows the mean entrainment velocity into the plume, along with the moving average of that mean. Despite being composed of separate camera views, the average entrainment velocity shows remarkable continuity. There is an initial jump in the entrainment velocity, followed by an equally sudden decrease, before the entrainment velocity stabilizes. From the simulations of Marjanovic (2018) we know that bubbles plumes initially mildly contract and accelerate, consistent with our experiments as shown in section 4.2. Between $z/D_0 \approx 0 - 10$ in the plume development region, the plumes engulf relatively little air. We saw this in the plumes visually as well, with few billowing structures for the first few z/D_0 of plume development–structures which are known to be responsible for entrainment and mixing. After $z/D_0 \approx 10$, the entrainment velocity levels out, remaining relatively stable with axial distance.
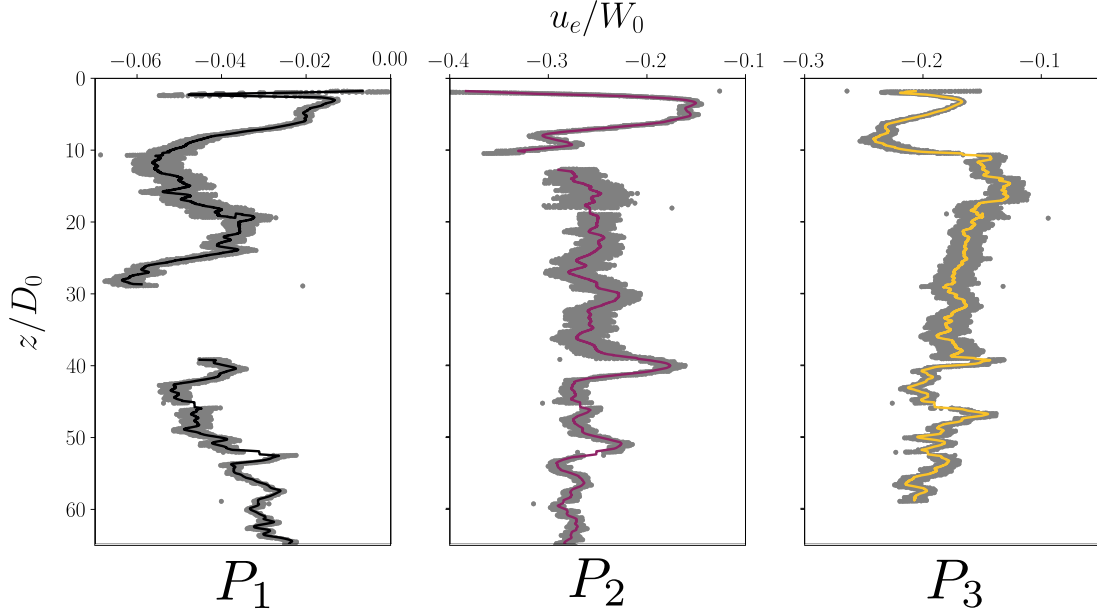
Figure 4.10: Mean entrainment velocities into plumes P_1 (left) P_2 (center) and P_3 (right). Gray dots indicate the mean at each plume-boundary pixel location, while the colored lines represent moving averages with a kernel size of 100 pixels.

With so much of integral plume theory being built of Morton's assumption of a constant entrainment coefficient, we further wanted to directly estimate α in these multiphase plumes. To do so, we make the assumption that the centerline air velocity can be related to the centerline particle velocity by a constant slip velocity equal to the Stoke's settling velocity of the particles. Since the velocity profiles are well approximated by a Gaussian, we take the top-hat velocity $w_{f,avg} = (W_{p,c} - \tau_p g)/2$ to be the characterstic air velocity against which to compare the entrainment. The ratio of the entrainment velocity to the estimated air centerline velocity provides us an estimate of α in each plume. These results are shown in figure 4.11.

The entrainment coefficient is similar between the three plumes. After the development region, the three entrainment coefficients are relatively stable and average out to $\alpha_{P_1} = 0.042$, $\alpha_{P_2} = 0.044$ and $\alpha_{P_3} = 0.036$. This seems to lend credence to the idea
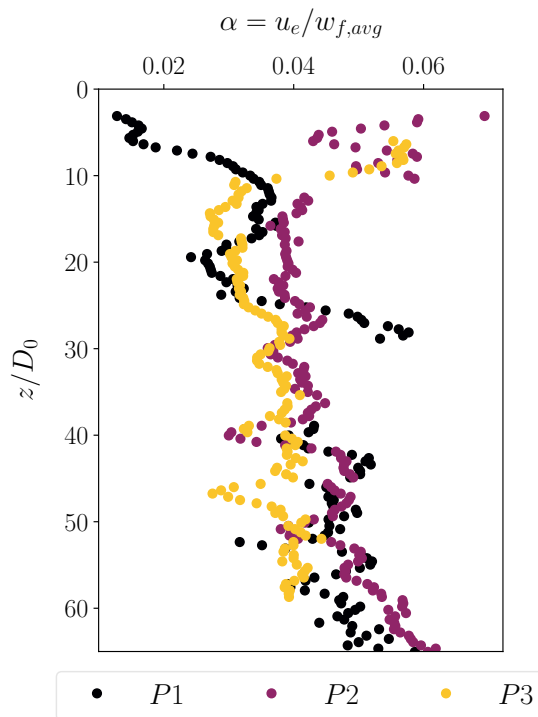
Figure 4.11: Estimated entrainment coefficient for the three particle plumes tested.

that α is constant with axial distance as proposed by Morton *et al.* (1956), at least in the far-field where the particle plumes have returned to self-similarity. α_{P_3} is slightly lower than the other two estimates, though this variation is probably within the random error. For plumes P_2 and P_3, we se an initial jump in the entrainment coefficient, similar to the results of Marjanovic (2018) for all their plumes tested (pure, forced, lazy). However we do not observe the same increasing trend in P_1, possibly due to experimental error, or simply not resolving close enough to the plume source to measure any increase in initial entrainment where the plume first enters the test chamber. Compared to other studies which measured entrainment coefficients in multiphase plumes, our estimates were somewhat lower: McHugh & Cardoso (2011) found experimental values of $\alpha \sim 0.09$, while the simulations of Marjanovic (2018) found α initially spike to between 0.3 and 0.4, followed by a decay and an asymptotic decay to $\alpha \approx 0.12$. The thesis of Liu (2003)

however found a value of 0.03 based on best fits of their experimental air volume flux measurements.

4.4   Comparing Experiments to 1-D Models

We compared our experimental results with four models: i) single-phase pure plumes, ii) single-phase lazy plumes, iii) single-phase forced plumes and iv) multiphase particle plume model inspired by Liu (2003) and Lai *et al.* (2016). All four models use Morton's entrainment hypothesis. Until now, without measurements of α, we were unable to classify our plumes as either forced, lazy or pure. The equations for mass, momentum and buoyancy flux are slightly different than those for single-phase plumes, as they take into account the solid-volume fraction, ϕ_v Marjanovic (2018):

$$Q_f(z) = \int_0^\infty 2\pi r(1 - \phi_v(r,z))w_f(r,z)dr \tag{4.6}$$

$$Q_p(z) = \int_0^\infty 2\pi r\phi_v(r,z)w_p(r,z)dr \tag{4.7}$$

$$M(z) = \int_0^\infty 2\pi r\left[w_f(r,z)^2(1 - \phi_v(r,z)) + \frac{\rho_p}{\rho_f}w_p(r,z)^2\phi_v(r,z)\right]dr \tag{4.8}$$

$$B(z) = \int_0^\infty 2\pi r\phi_v(r,z)g\frac{\rho_f - \rho_p}{\rho_f}w_p(r,z) \tag{4.9}$$

Using our estimates of initial velocity and concentration (4.1), and assuming the fluid lags the particle velocity by $\tau_p g$, we can calculate these fluxes, and thus our initial plume function, $\Gamma_0 = (5(Q_{f,0} + Q_{p,0})^2 B_0)/(8\alpha\sqrt{\pi}M_0^{5/2})$. All three plumes are forced, with $\Gamma_{P_1,0} = 0.16$, $\Gamma_{P_2,0} = 0.052$ and $\Gamma_{P_3,0} = 0.015$.

van Den Bremer & Hunt (2010) showed that using the entrainment hypothesis, the solutions to the plume conservation equations are universal for pure, lazy and forced plumes, with a minor difference between Boussinesq and non-Boussinesq. Those plume conservation equations generally use top-hat profiles to describe the time-averaged radial

variation of vertical velocity and density, and can be written as:

$$\frac{d(\eta w b^2)}{dz} = 2bu_e \tag{4.10}$$

$$\frac{d(\eta w^2 b^2)}{dz} = g(1 - \eta)b^2 \tag{4.11}$$

$$\frac{d(w b^2)}{dz} = 2bu_e \tag{4.12}$$

for mass, momentum and volume flux conservation respectively. w denotes vertical velocity, b the plume radius, η the density ratio of the bulk plume density ρ_b and the ambient ρ_f, and u_e is the entrainment velocity. van Den Bremer & Hunt (2010) manipulated these equations in terms of the non-dimensional plume function Γ, $\hat{\beta} = b/b_0$ the plume radius normalized by its initial value, $\hat{w} = w/w_0$, the vertical velocity normalized by its initial value, and a non-dimensional axial distance $\zeta = 4\alpha z/b_0$ such that the conservation equations 4.10–4.12 are recast:

$$\frac{d\Gamma}{d\zeta} = \frac{\Gamma(1 - \Gamma)}{\hat{\beta}} \text{sign}(w) \tag{4.13}$$

$$\frac{d\hat{\beta}}{d\zeta} = \frac{1}{5}\left(\frac{5}{2} - \Gamma\right)\text{sign}(w) \tag{4.14}$$

$$\frac{d\hat{w}}{d\zeta} = \frac{2}{5}\frac{\hat{w}}{\hat{\beta}}\left(\Gamma - \frac{5}{4}\right)\text{sign}(w) \tag{4.15}$$

Following the notation of van Den Bremer & Hunt (2010), the density ratio η is also recast as:

$$\Delta = \begin{cases} 1 - \eta & \text{Boussinesq} \\ \dfrac{1 - \eta}{\eta} & \text{non-Boussinesq} \end{cases}$$

For pure plumes ($\Gamma = 1$), the solutions for width, velocity and density to equations 4.13-4.15 are:

$$\frac{b}{b_0} = \frac{3}{10}\left(\frac{10}{3} + \zeta\right) \tag{4.16}$$

$$\frac{w}{w_0} = \left(\frac{10}{3}\right)^{1/3}\left(\frac{10}{3} + \zeta\right)^{-1/3} \tag{4.17}$$

$$\frac{\Delta}{\Delta_0} = \left(\frac{10}{3}\right)^{5/3}\left(\frac{10}{3} + \zeta\right)^{-5/3}. \tag{4.18}$$

The solutions for forced and lazy plumes are more complicated. Equations 4.13 and 4.14 can be solved simulataneously to get the plume radius for these plumes:

$$\frac{b}{b_0} = \sqrt{\frac{\Gamma}{\Gamma_0}}\left(\frac{1 - \Gamma_0}{1 - \Gamma}\right)^{3/10} \tag{4.19}$$

which is then substituted into 4.13 to get the rate of change of the plume function with height:

$$\frac{d\Gamma}{d\zeta} = \Gamma(1 - \Gamma)\sqrt{\frac{\Gamma_0}{\Gamma}}\left(\frac{1 - \Gamma_0}{1 - \Gamma}\right)^{3/10}\text{sign}(w) \tag{4.20}$$

which can then be integrated to find the height ζ at which a given value of Γ is reached (see eq. 4.3 in van Den Bremer & Hunt (2010)). The solutions for velocity and density follow as:

$$\frac{w}{w_0} = \sqrt{\frac{\Gamma_0}{\Gamma}}\left(\frac{1 - \Gamma}{1 - \Gamma_0}\right)^{1/10} \tag{4.21}$$

$$\frac{\Delta}{\Delta_0} = \sqrt{\frac{\Gamma_0}{\Gamma}}\sqrt{\frac{1 - \Gamma}{1 - \Gamma_0}} \tag{4.22}$$

With the requisite source conditions, these equations can be solved.

The following multiphase model is inspired by the thesis of Liu (2003), but modified to better represent the conditions of our plumes. Starting with the forces, drag, F_D, and

buoyancy forces, F_B act on the the particles via the following equations:

$$F_D = \frac{1}{2}\rho_f C_D C_s (\pi d_p^2/4)(w_p - w_f)^2 \tag{4.23}$$

$$F_B = \frac{1}{6}\pi d_p^3 (\rho_p - \rho_f)g \tag{4.24}$$

where d_p is the particle diameter, g is the gravitational acceleration, C_D is coefficient and C_s is a factor meant to modify the drag to better describe drag acting on a multiparticle system. In Liu (2003), this factor is taken to be proportional to the solid-volume fraction: $C_s = (1 - \phi_v)^{-4.7}$. We use the drag coefficient with the Schiller & Naumann correction as described in Crowe *et al.* (2011): $C_D = (24/Re_p)(1 + 0.15Re_p^{0.687})$, where Re_p is the particle Reynolds number ($Re_p = (w_p - w_f)d_p/\nu$, with ν being the kinematic viscosity of air in our case). Assuming that with time, the plume will average out to an axisymmetric cone shape, the number of particles within a given annular ring of width Δr and height Δz is given by:

$$N_p = \frac{\phi_{v,avg}2\pi r\Delta r\Delta z}{\frac{1}{6}\pi d_p^3} \tag{4.25}$$

and therefore the sum of forces acting on the volume of that annular ring is $N_p(F_B - F_D)$. The rate of change of the momentum of falling particles is then: $\dot{m}_p\frac{dw_p}{dt} = N_p(F_B - F_D)$, which under the assumption of steady flow becomes a relation with axial distance:

$$\frac{dw_p}{dt} = \dot{m}_p w_p\frac{dw_p}{dz} = N_p(F_B - F_D) \tag{4.26}$$

To model the volume flux of entrained air Liu (2003) also used the entrainment hypothesis, and simplifying with top-hat profiles, the conservation equation is written as:

$$\frac{d}{dz}\left(\pi b_f^2 w_f\right) = 2\pi b_f \alpha w_f \tag{4.27}$$

where b_f is the radius of the fluid-phase of the plume. The momentum of the air-phase is modeled using Newton's second law–the rate of change of momentum flux of the

entrained air with respect to axial distance has to be equal to the sum of drag forces acting on the particles per unit drop height:

$$\frac{d}{dz}\left(\rho_f \pi b_f^2 w_f^2\right) = \frac{1}{w_p} F_D \tag{4.28}$$

Equations 4.25, 4.26 and 4.27 can then be discretized, and solved using Euler's method. Specifying initial conditions, the remainder of the variables can be solved for. Using conservation of mass, the bulk density of the plume at each step of axial distance is:

$$\rho_b = \frac{\dot{m}_p}{\pi b_p^2 w_p} + \rho_f \tag{4.29}$$

which can be converted to a volume fraction for calculating C_s. Finally, Liu (2003) uses the expression for the volume of air entrained, $Q_f = \pi b_f^2 w_f$, to solve for b_f, and the definition of the entrained air momentum $M_f = \rho_f \pi b_f^2 w_f^2$ to solve for w_f. Missing from Liu's model is a solution for b_p, the radius of the particle-phase of the plume. Liu's original model assumes particles fall in a stream, with a stable core of particles that does not expand. Thus if we wanted to additionally solve for b_p, we had to find another equation to close the system of equations. This equation was inspired by the spreading hypothesis model of Lai *et al.* (2016). They assumed that the particles' spread over a differential time dt is proportional to the fluid's: $db_p \sim \frac{db_f}{dz} w_f dt$ where w_f is the characteristic velocity of the fluid, as before. Using the mean vertical particle velocity, w_p, the axial distance particles travel over a time dt is $dz \sim w_p dt$, leading to the particle-phase spread rate:

$$\frac{db_p}{dz} = \frac{db_f}{dz}\frac{w_f}{w_p}. \tag{4.30}$$

Equation 4.30 is a fourth differential equation, which can also be discretized and solved via Euler's method and completes our system of equations.

We solve the pure plume equations (eqs. 4.16–4.18), forced/lazy plume equations (eqs. 4.19–4.22) and the multiphase plume model (eqs. 4.26–4.30, in addition to the

definitions of Q_f, M_f and C_s) and compare the predictions of the preceeding four models with the observables from our experiments: the particle-phase plume width and the particle velocity.

The initial conditions are chosen to match our experimental parameters. For the multiphase model, the mass flow rate, initial particle velocity and bulk density are taken from table 4.1. The initial fluid velocity is, as before, assumed to lag by $\tau_p g$. For the single-phase models, the mass flow rate, initial bulk density and velocity are the same as in table 4.1. For the lazy plume model, these source conditions determine the plume function Γ_0; while to model the force plumes, we substitute in our experimental estimates for Γ_0. The inital particle and fluid phase radii are initialized as equaling the chute outlet diameter, D_0, in all cases. Finally, we use our experimentally determined values of the entrainment coefficient, α to close the equations. Though the models are written and solved for top-hat quantities, assuming a Gaussian profile, they can be converted between each other. The top-hat velocity is related to the centerline Gaussian value by:

$$w_{avg} = \frac{w_c}{2} \tag{4.31}$$

while the radius of a top-hat distribution is related to the $1/e$ radius calculated in section 4.2 as:

$$b_{avg} = b\sqrt{\ln(2)} \tag{4.32}$$

Figure 4.12 compares the experimentally measured particle-phase radius to the model predictions. The spread rates seem to be described best by our multiphase phase model, followed by the lazy single-phase model, both of which display the initial "necking" behavior. Our experimentally measured plume widths are not as linear as the model predictions, though this could be due to experimental error. As the image intensity decreased due to the particles spreading and mixing into the domain (and the laser sheet

intensity decreasing) the "signal" to noise ratio of the centerline intensity to the background noise lessened, which could be responsible for the increased spread past 50 z/D_0.
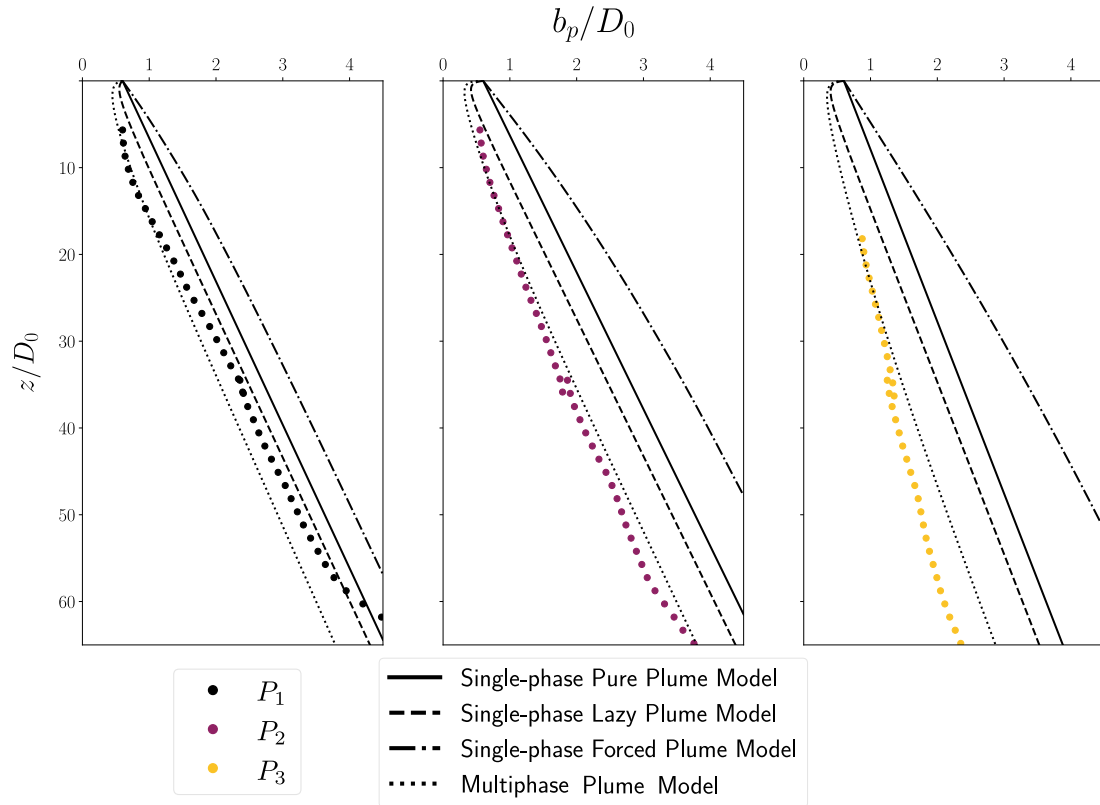
Figure 4.12: From left to right: model and experimental data comparisons for P_1, P_2 and P_3 for the plume widths normalized by the source diameter. The multiphase model is the best performing in all cases.

Figure 4.13 presents our final comparison between the experimental and model centerline velocities, normalized by the Stokes' settling. Here, the limitations of approximating multiphase plumes with single-phase models becomes clear–the forced and pure plumes cannot capture the initial acceleration we observed. The lazy plume does predict an acceleration, though neither of the correct magnitude nor the correct peak location.

The multiphase plume also predicts an initial acceleration with axial distance, and approaches the experimental results. It much more accurately predicts the axial location where the velocity reaches its maximum than the single-phase models. Encouragingly, it also seemed to predict the decay rate of the velocity in plume P_2 particularly accurately.
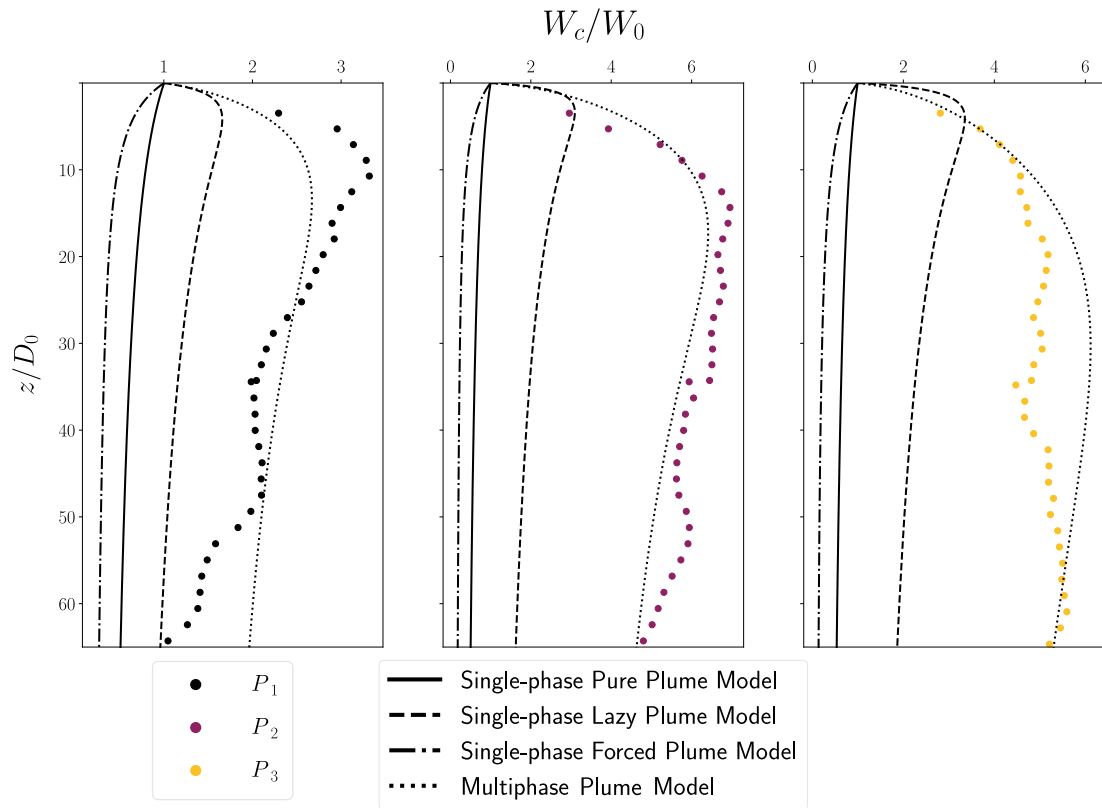
Figure 4.13: From left to right: model and experimental data comparisons for P_1, P_2 and P_3 for the centerline velocities normalized by the source velocity. Again the multiphase model well-represents our laboratory findings.

There are several ways the multiphase model in particular could be improved upon. Besides a better formulation for predicting the particle plume radius, the drag particles experience when in dense clusters could also be important. We attempted to capture these physics through the drag factor C_s in our multiphase model, though it

would be interesting to see other formulations tested. Additionally, our model relies on experimentally determined entrainment coefficients. A model for that all-important quantity based on plume initial conditions would be immensely helpful, especially when trying to predict the behavior of particle plumes outside the laboratory setting. Still, these comparisons are useful for determining where, when and how very simple 1-D integral models can be helpful when predicting the time-averaged dynamics of turbulent particle plumes in particular. Pure and forced single-phase plumes in particular cannot capture the initial acceleration particle plumes undergo. This is particularly interesting considering the single-phase forced plumes are prescribed the same value of Γ as our multiphase plumes. Evidently the plume function does not directly translate between multi and single-phase plumes. One major difference between the single and multiphase plume models is the presence of a slip velocity between the phases. As Marjanovic (2018); Socolofsky & Adams (2002) have noted, the slip velocity is important because it does not decay as the average plume velocity does. This leads directly to the erosion of self-similarity, and correctly predicting the slip velocity could be responsible for the difference between a representative multiphase model, and an unsuccessful one.

Chapter 5

General Conclusions and Perspectives

In this thesis, we conducted experimental studies of inertial particles falling in air. Using the high-speed imaging, PIV and PTV we were able to access the motion of inertial particles as well as the dynamics of the surrounding turbulent air flow. For the dilute-regime experiments, simultaneous measurment of the inertial particle trajectories and the turbulence yielded statistical analyses of the particle-turbulence coupling that was previously inaccessible experimentally. The results from the homogeneous particle-laden turbulence section of the thesis can be summarized as follows:

1. The jet-stirred homogeneous air turbulence chamber is particularly suitable to characterize the considered regime: the lack of mean flow enables the unbiased measurement of the settling velocity, also yielding a much larger dynamic range for the velocity fluctuations compared to wind tunnel experiments (Carter & Coletti, 2017). Moreover, the large region of homogeneous turbulence is crucial for the particles to interact with the full range of turbulent scales (Bellani & Variano, 2014). The simultaneous imaging of both phases allows the characterization of their interplay, within the inherent limits posed by the imaging accuracy and its planar nature. Finally, the relatively high Re_λ warrants the separation of scales needed to identify the dominant flow parameters.

2. We have characterized the particle spatial distribution using both RDF and Voronoï diagrams. The former show a power-law decay over (and beyond) the near-dissipative scales, followed by a long exponential tail. The latter indicates that clustering extends far beyond the dissipation range, although the particle field does not display scale-invariant properties over such distances. It is confirmed that clustering is most intense for $St_\eta \approx 1$, but remains significant even for more inertial particles, which in fact cluster over larger regions. This is due partly to their response time being comparable to the time scales of larger eddies, and partly to the effect of gravity. It was indeed reported in several numerical investigations that

gravitational settling enhances clustering for $St_\eta > 1$ (see Ireland *et al.*, 2016*b*). Gravity is unavoidable in laboratory experiments, thus its effect is hard to discern from inertia. However, our results for various St_η and Sv_η are at least consistent with this trend. We argue that such an effect is associated to u' becoming the relevant velocity scale for the interaction of turbulence with fast-falling particles: the latter quickly decorrelate from Kolmogorov-size eddies, and rather respond to large-scale velocity fluctuations. Indeed, the fraction of clustered particles and the cluster size generally increases with particle inertia.

3. The Voronoï diagram method generally confirms the findings from the RDF analysis, and allows us to explore further aspects of the particle distribution, focusing on individual clusters. The properties of those discrete groups of highly concentrated particles bears particular significance, as these may interact with one other and, by virtue of their collective action, modify the surrounding flow (Monchaux *et al.*, 2012). We find that sufficiently large clusters (i.e. "coherent clusters" in the definition of Baker *et al.* (2017) follow power-law size distributions over several decades, and display a precise fractal dimension. Therefore, borrowing the terminology proposed by Paola *et al.* (2009) to describe scale-invariance in geomorphology, these objects exhibit both internal similarity (between the system and small parts of it) and external similarity (between the system and small copies of it). This also suggests that they follow (without necessarily replicating) the self-similar topology of the underlying turbulence. The clusters are usually elongated and often aligned with the vertical direction. The mean particle concentration in a cluster can be an order of magnitude higher than the average, and is largely independent on the cluster size.

4. It may appear surprising that particle clusters display both internal and external similarity, and over such a wide range of scales. After all, turbulence is known

to display strong departures from self-similarity associated to its intermittent behavior. However, a few considerations are in order. First, intermittency is most evident in high-order quantities in which the size and shape of the clusters of inertial particles might be relatively insensitive. In fact, the intense vortex filaments usually regarded as responsible for scale-variant behaviors are precisely the structures where particles of $St_\eta = O(1)$ are unlikely to be found. Also, by focusing on coherent clusters, we set a size threshold larger than the scale over which intermittency is manifest.

5. One of the major findings of the study is that, for St_η and Sv_η of order unity and in the considered range of Re_λ, turbulence produces almost a three-fold increase in settling velocity with respect to quiescent conditions. Such a dramatic effect has far-reaching consequences in a myriad of natural and engineering settings, from atmospheric precipitation to industrial processes and pollutant dispersion. Remarkably, the effects of turbulence on the fallspeed of hydrometeors have only recently begun to be addressed in field studies (Garrett & Yuter, 2014). In particular, the present results are consistent with the measurements by Nemes *et al.* (2017) who imaged snowflakes settling in the atmospheric surface layer. The data is best collapsed by a mixed scaling based on τ_η and u', which may reflect how the latter is indeed the relevant velocity scale ruling the settling enhancement. This argument is consistent with the idea of distant-scale interaction, which has been used in wall-bounded flows to explain the success of mixed scaling of the streamwise turbulent fluctuations (Marusic & Kunkel, 2003).

6. Clusters fall even faster than the average particle in turbulence. In the considered range of parameters, this appears to be due to the particle tendency to oversample downward flow regions, according to the preferential sweeping mechanism. The latter is shown to be responsible for the observed enhanced settling, and in the present regime is a more recognizable feature than the preferential concentration in

high-strain/low-vorticity regions. Owing to the crossing trajectory and continuity effects, the vertical velocity fluctuations of the particles are stronger than the horizontal ones. The r.m.s. of the vertical slip velocities are also larger than the horizontal, and both can largely exceed their respective mean values. Thus, the actual particle Reynolds number can greatly differ from the nominal value usually used to correct Stokes' law. Indeed, the effective drag coefficient calculated via the simultaneous two-phase measurements is found to depart significantly from the standard estimate. This points to clear limitations of the point-particle approach, perhaps accounting for some of the quantitative disagreement between experiments and DNS at matching conditions (Good *et al.*, 2014).

7. At sufficient concentrations, the particles excite small-scale fluid velocity fluctuations, which however may represent a small fraction of the turbulent kinetic energy. For the heavier particles, we generally observe a reduction of turbulent energy at the larger scales. Over the considered range of parameters, the measurements did not indicate a trend of augmentation versus attenuation of the overall turbulence intensity. This is perhaps not surprising, considering the multiple counteracting effects contributing to turbulence modification at the different scales, along with the difficulty of varying one parameter at a time. Dedicated experiments in which the volume fraction is systematically varied over a wide range, keeping all other settings constant, stand a higher chance of providing some conclusive answer. Such a study, however, is expected to be challenging: for sub-Kolmogorov particles and relatively high Re_λ, substantial mass loadings require large number densities, posing problems for the fluid velocimetry. Those can be alleviated by imaging at very high resolution; but this limits the FOV, and consequently the insight into multi-scale mechanisms. Therefore, the use of very large sensors and/or the simultaneous deployment of multiple cameras appear necessary to fully quantify two-way coupling effects in preferentially concentrated particle-laden turbulence.

Our study of dense, falling particle-laden plumes provided unique experimental results into the dynamics of these multiphase plumes. By conducting two experiments–one capturing the inertial particle behavior and another zoomed in onto the plume interface–we were able to measure both the time-averged particle phase dynamics and the air entrainment across the plume interface. Our observations revealed the following:

1. The particle-laden plumes were reasonably self-similar in their mean velocity and concentration radial profiles. This is an important conclusions, especially when using or developing integral models of particle-laden plumes as the self-similarity assumption greatly simplifies the governing equations. It is not a trivial assumption either, as the slip velocity between the disperse and continuous phase generally acts to degrade the self-similarity of multiphase plumes (Marjanovic, 2018).

2. We found a trend of decreased spread for lower plume functions, Γ_0 (corresponding to higher initial mass flux). Evidently, more jet-like particle-laden plumes are more resistant to mixing with the ambient, retaining their dense cores for longer. The centerline plume velocity initially acclerated in all three plumes, but to different magnitudes. The least dense plume accelerated to $<2{\times}W_0$, the source velocity whereas the denser plumes accelerated to between 4.5–$6{\times}W_0$. After the initial acceleration region, the least dense plume's centerline velocity decayed according to a power law with a -0.4 exponent, similar to the expected decay rate for a single-phase pure plume of $-1/3$. However, increasing the initial mass flux changed the decay rate. The two more jet-like plume centerline velocities decayed much more slowly, with the densest not significantly decaying at all over our imaging area.

3. Our PIV measurements of the ambient fluid flow field allowed us to calculate the entrainment velocity into the particle plumes along the ambient-plume interface instantaneously. The time-averaged quantity was remarkably consistent with axial

distance despite being a composite of multiple runs. We estimated the average fluid velocity assuming the slip velocity was constant and equal to the Stoke's settling velocity. This allowed us to calculated an estimated entrainment coefficient for the three particle-laden plumes. After the initial plume development region, the entrainment rate was relatively constant for the extent of the measurement length, indicating that at least over the axial distance we observed a constant entrainment coefficient, as assumed by many plume models, is a reasonable assumption.

4. Finally, we compared our experimental results to single and multiphase 1-dimensional plume models. While our multiphase plumes were all forced, the single-phase forced plume model generally performed worst when predicting the characteristics of multiphase plumes in large part due to the differences in how multiphase plumes evolve in the near-field region. The initial acceleration is only observed in lazy single-phase plumes, but the lazy plume model was unable to capture the peak of the average velocity. A 1-D multiphase plume model inspired by Liu (2003) and Lai *et al.* (2016) was generally the best performer, as it was able to predict the average velocity and plume spread quite well.

Future Outlook

The ideas and observations provided in this thesis can be improved upon in several ways. Overcoming the limitations of planar measurements will require a leap in performance of 3D particle imaging at high concentrations. Novel approaches based on Tomographic PTV are breaking grounds in single-phase velocimetry (Schanz *et al.*, 2016), and may be applied to inertial particles. Advanced numerical methods are also expected to shed new light on dilute particle suspensions in turbulence: particle-resolved DNS has been successfully applied to investigate relatively large particles (Naso & Prosperetti, 2010; Lucci *et al.*, 2010; Tenneti & Subramaniam, 2014; Cisse *et al.*, 2013;

Gao *et al.*, 2013; Uhlmann & Doychev, 2014; Fornari *et al.*, 2016), and recently even Kolmogorov-sized particles (Schneiders, Meinke & Schroeder 2017). The ever-increasing computational power will soon allow resolving even smaller objects, elucidating the role of mechanisms such as the local hydrodynamic interaction between particles (Wang *et al.*, 2007). Still, capturing truly collective effects with this approach will require enormous computational resources. Considering the dilute experiments in this thesis as an example (e.g., $L \approx 100$ mm and $d_p \approx 50\mu$m), a cubic domain of size $2\pi L$ with a volume fraction of $5 \cdot 10^{-5}$ contains $\sim O(10^8)$ particles. Low-order methods able to incorporate the essential physics are therefore sorely needed; the role of experiments and particle-resolved simulations in informing and validating them will be essential. Furthermore, future experiments could better investigation particle back-reaction onto the flow by systematically varying quantities like the ϕ_v, St_η and Sv_η to examine any underlying trends between those quantities and turbulence augmentation/attenuation.

Understanding the dynamics of multiphase plumes will require more study on the experimental and computational side. There are relatively few works on particle-laden plumes in air in particular due to the experimental challenges, but there are also few computational studies on the systems studied in this thesis. Our study on particle-laden plumes in this thesis focused on first-order statistics of the particle and fluid phases. Future investigations into higher order quantities are planned. Examining for example, the turbulent fluxes and seeing to what degree the eddy-viscosity and gradient-diffusion hypotheses hold for these multiphase shear flows. Our datasets also permit the study of the instantaneous plume structures, like the billowing instabilities at the plume boundary. These structures seem largely responsible for air entrainment and mixing, but we have not yet examined their role quantitatively. Our integral model of multiphase plumes could also be improved upon. We see two particular avenues–incorporating a model for the entrainment coefficient and trying different formulations for the drag experienced by dense groupings of inertial particles. Finally, our setup inside the turbulence box

described in chapter 2 begs the question: how would a turbulent ambient environment affect these particle-laden plumes? Real world scenarios in which one might find these plumes are bound not to be shielded from turbulent fluid flow, which could have drastic effects on the structure of these plumes and thus the transport of the dispersed phase.

References

Agrawal, L., Mandal, J.C. & Marathe, A.G. 2001 Computations of laminar and turbulent mixed convection in a driven cavity using pseudo-compressibility approach. *Computers & fluids* **30** (5), 607–620.

Alendal, Guttorm & Drange, Helge 2001 Two-phase, near-field modeling of purposefully released co2 in the ocean. *Journal of Geophysical Research: Oceans* **106** (C1), 1085–1096.

Aliseda, A., Cartellier, A., Hainux, F. & Lasheras, J. C. 2002 Effect of preferential concentration on the settling velocity of heavy particles in homogeneous isotropic turbulence. *J. Fluid Mech.* **468**, 77–105.

Alméras, Elise, Mathai, Varghese, Lohse, Detlef & Sun, Chao 2017 Experimental investigation of the turbulence induced by a bubble swarm rising within incident turbulence. *J. of Fluid Mech.* **825**, 1091–1112.

Ayyalasomayajula, S., Gylfason, A., Collins, L.R., Bodenschatz, E. & Warhaft, Z. 2006 Lagrangian measurements of inertial particle accelerations in grid generated wind tunnel turbulence. *Phys. Rev. Lett.* **97** (14), 144507.

Bachelor, GK 1953 *Theory of Homogeneous Turbulence*. Cambridge University Press, Cambridge.

BAGCHI, P. & BALACHANDAR, S. 2003 Effect of turbulence on the drag and lift of a particle. *Physics of Fluids* **13**, 3496.

BAKER, LUCIA, FRANKEL, ARI, MANI, ALI & COLETTI, FILIPPO 2017 Coherent clusters of inertial particles in homogeneous turbulence. *J Fluid Mech.* **833**, 364–398.

BALACHANDAR, S. 2009 A scaling analysis for point–particle approaches to turbulent multiphase flows. *International Journal of Multiphase Flow* **35** (9), 801–810.

BALACHANDAR, S. & EATON, JOHN K. 2010 Turbulent dispersed multiphase flow. *Annual Review of Fluid Mechanics* **42** (1), 111–133.

BATCHELOR, G.K. 1954 Heat convection and buoyancy effects in fluids. *Quarterly journal of the royal meteorological society* **80** (345), 339–358.

BATESON, COLIN P. & ALISEDA, ALBERTO 2012 Wind tunnel measurements of the preferential concentration of inertial droplets in homogeneous isotropic turbulence. *Exp. in Fluids* **52** (6), 1373–1387.

BEC, JÉRÉMIE 2003 Fractal clustering of inertial particles in random flows. *Phys. of Fluids* **15**, L81.

BEC, J., BIFERALE, L., BOFFETTA, G., CELANI, A., LANOTTE, A., MUSACCIO, S. & TOSCHI, F. 2006 Acceleration statistics of heavy particles in turbulence. *J. Fluid Mech.* **550**, 349–358.

BEC, J., BIFERALE, L., CENCINI, M. & LANOTTE, A.S. 2010 Intermittency in the velocity distribution of heavy particles in turbulence. *J. Fluid Mech.* **646**, 527–536.

BEC, J., BIFERALE, L., CENCINI, M., LANOTTE, A., MASUCCHIO, S. & TOSCHI, F. 2007 Heavy particle concentration in turbulence at dissipative and inertial scales. *Physical Review Letters* **98**.

Bec, Jérémie, Cencini, Massimo, Hillerbrand, Rafaela & Turitsyn, Konstantin 2008 Stochastic suspensions of heavy particles. *Physica D: Nonlinear Phenomena* **237**, 2037–2050.

Bec, Jérémie, Homann, Holger & Ray, Simriddhi Sankar 2014*a* Gravity-driven enhancement of heavy particle clustering in turbulent flow. *Phys. Rev. Lett.* **112** (18), 184501.

Bec, Jérémie, Homann, Holger & Ray, Samriddhi Sankar 2014*b* Gravity-driven enhancement of heavy particle clustering in turbulent flow. *Phys. Rev. Lett.* **112**, 184501.

Bellani, Gabriele, Byron, Margaret L., Collignon, Audric G., Meyer, Colin R. & Variano, Evan A. 2012 Shape effects on turbulent modulation by large nearly neutrally buoyant particles. *J. Fluid Mech.* **712**, 41–60.

Bellani, Gabriele & Variano, Evan A. 2014 Homogeneity and isotropy in a laboratory turbulent flow. *Exp. in Fluids* **55** (1), 1646.

Bendat, Julius S. & Piersol, Allan G. 2011 *Random Data Analysis and Measurement Procedures*. John Wiley & Sons, Inc., Hoboken, New Jersey.

Bernard, Peter S. & Wallace, James M. 2002 *Turbulent flow: Analysis, measurement and prediction*. John Wiley & Sons.

Bewley, Gregory P., Saw, Ewe-Wei & Bodenschatz, Eberhard 2013 Observation of the sling effect. *New Journal of Physics* **15**.

Blum, Daniel B., Kunwar, Surendra B., Johnson, James & Voth, Greg A. 2010 Effects of nonuniversal large scales on conditional structure functions in turbulence. *Physics of Fluids* **22** (1), 015107.

Boivin, Marc, Simonin, Olivier & Squires, Kyle D. 1998 Direct numerical simulation of turbulence modulation by particles in isotropic turbulence. *J. Fluid Mech.* **375**, 235–263.

Bombardelli, F.A., Buscaglia, G.C., Rehmann, C.R., Rincón, L.E. & García, Marcelo Horacio 2007 Modeling and scaling of aeration bubble plumes: A two-phase flow analysis. *J. of Hydraul. Research* **45** (5), 617–630.

Bordás, R., Roloff, Ch., Thévenin, D. & Shaw, R.A. 2013 Experimental determination of droplet collision rates in turbulence. *New Journal of Physics* **15** (4), 045010.

Bosse, Thorsten & Kleiser, Leonhard 2006 Small particles in homogeneous turbulence: Settling velocity enhancement by two-way coupling. *Physics of Fluids* **18**, 027102.

Bourgoin, Mickaël, Ouellette, Nicholas T, Xu, Haitao, Berg, Jacob & Bodenschatz, Eberhard 2006 The role of pair dispersion in turbulent flow. *Science* **311** (5762), 835–838.

Bradley, W.H. 1965 Vertical density currents. *Science* **150** (3702), 1423–1428.

Bragg, Andrew B. & Collins, Lance R. 2014 New insights from comparing statistical theories for inertial particles in turbulence: I. spatial distribution of particles. *New Journal of Physics* **16**.

Bragg, Andrew D., Ireland, Peter J. & Collins, Lance R. 2015 Mechanisms for the clustering of inertial particles in the inertial range of isotropic turbulence. *Phys. Rev. E* **92** (2), 023029.

Calzavarini, Enrico, Kerscher, Martin, Lohse, Detlef & Toschi, Federico 2008 Dimensionality and morphology of particle and bubble clusters in turbulent flow. *J. Fluid Mech.* **607**, 13–24.

CAPECELATRO, JESSE, PEPIOT, PERRINE & DESJARDINS, OLIVIER 2015 Numerical investigation and modeling of reacting gas-solid flows in the presence of clusters. *Chemical Engineering Science* **122**, 403–415.

CARAZZO, G. & JELLINEK, A.M. 2013 Particle sedimentation and diffusive convection in volcanic ash-clouds. *Journal of Geophysical Research: Solid Earth* **118** (4), 1420–1437.

CARAZZO, G., JELLINEK, A.M. & TURCHYN, A.V. 2013 The remarkable longevity of submarine plumes: Implications for the hydrothermal input of iron to the deep-ocean. *Earth and Planetary Science Letters* **382**, 66 – 76.

CARDY, JOHN, FALKOVICH, GREGORY & GAWEDZKI, KRZYSZTOF 2008 Preface. In *Non-equilibrium Statistical Mechanics and Turbulence* (ed. Sergey Nazarenko & Oleg V. Zaboronski), pp. ix–x. Cambridge University Press, New York.

CAREY, S.N., SIGURDSSON, H. & SPARKS, R.S.J. 1988 Experimental studies of particle-laden plumes. *Journal of Geophysical Research: Solid Earth* **93** (B12), 15314–15328.

CAREY, STEVEN & SPARKS, R.S.J. 1986 Quantitative models of the fallout and dispersal of tephra from volcanic eruption columns. *Bulletin of Volcanology* **48** (2-3), 109–125.

CARLOTTI, PIERRO & HUNT, GARY R. 2005 Analytical solutions for turbulent non-boussinesq plumes. *J. of Fluid Mech.* **538**, 343–359.

CARTER, DOUGLAS & COLETTI, FILIPPO 2018 Small-scale structure and scale interaction in homogeneous turbulence. *J. Fluid Mech.* **854**, 505–543.

CARTER, DOUGLA, PETERSEN, ALEC, AMILI, OMID & COLETTI, FILIPPO 2016 Generating and controlling homogeneous air turbulence using random jet arrays. *Exp. in Fluids* **57** (189).

CARTER, DOUGLAS W. & COLETTI, FILIPPO 2017 Scale-to-scale anisotropy in homogeneous turbulence. *J. Fluid Mech.* **827**, 250–284.

CAULFIELD, C.P. 1991 Stratification and buoyancy in geophysical flows. PhD thesis, University of Cambridge.

CENCINI, M., BEC, J., BIFERALE, L., CELANI, A., LANOTTE, A.S., MUSACCHIO, S. & TOSCHI, F. 2006 Dynamics and statistics of heavy particles in turbulent flows. *Journal of Turbulence* **7**.

CHANG, KELKEN, BEWLEY, GREGORY P. & BODENSCHATZ, EBERHARD 2012 Experimental study of the influence of anisotropy on the inertial scales of turbulence. *J. of Fluid Mech.* **692**, 464–481.

CHEN, L., GOTO, S. & VASSILICOS, J.C. 2006 Turbulent clustering of stagnation points and inertial particles. *J. Fluid Mech.* **553**, 143–154.

CHUN, JAEHUN, KOCH, DONALD L., RANI, SARMA L., AHLUWALIA, ARUJ & COLLINS, LANCE R. 2005 Clustering of aerosol particles in isotropic turbulence. *J. Fluid Mech.* **536**, 219–251.

CISSE, MAMADOU, HOMANN, HOLGER & BEC, JÉRÉMIE 2013 Slipping motion of large neutrally buoyant particles in turbulence. *J. Fluid Mech.* **735**, R1.

CLIFT, ROLAND, GRACE, JOHN & WEBER, MARTIN E. 2005 *Bubbles, Drops and Particles*. Dover Publications, Inc., Mineola, New York.

COLEMAN, S.W. & VASSILICOS, J.C. 2009 A unified sweep-stick mechanism to explain particle clustering in two- and three-dimensional homogeneous, isotropic turbulence. *Physics of Fluids* **21**, 113301.

COLETTI, F., TOLOUI, M., FONG, K.O., NEMES, A. & BAKER, L. 2016 Volumetric distribution and velocity of inertial particles in a turbulent channel flow. *18th*

International Symposium on Application of Laser and Imaging Techniques to Fluid Mechanics, Lisbon, Portugal .

COMTE-BELLOT, GENEVIEVE & CORRSIN, STANLEY 1966 The use of a contraction to improve the isotropy of grid-generated turbulence. *J. Fluid Mech.* **25** (4), 657–682.

CROWE, CLAYTON T., SCHWARZKOPF, JOHN D., SOMMERFELD, MARTING & TSUJI, YUTAKA 2011 *Multiphase flows with droplets and particles*. CRC press.

CSANADY, G.T. 1963 Turbulent diffusion of heavy particles in the atmosphere. *Journal of the Atmospheric Sciences* **20** (3), 201–208.

DAVIDSON, PETER ALAN 2015 *Turbulence: an introduction for scientists and engineers*. Oxford university press.

DÁVILA, J. & HUNT, J.C.R. 2001 Settling of small particles near vortices and in turbulence. *J. Fluid Mech.* **440**, 117–145.

DEEN, NIELS GERBRAND, SOLBERG, TRON & HJERTAGER, BJØRN HELGE 2001 Large eddy simulation of the gas–liquid flow in a square cross-sectioned bubble column. *Chemical Engineering Science* **56** (21-22), 6341–6349.

DEJOAN, A. & MONCHAUX, R. 2013 Preferential concentration and settling of heavy particles in homogeneous turbulence. *Physics of Fluids* **25** (1), 013301.

DELNOIJ, E., LAMMERS, F.A., KUIPERS, J.A.M. & VAN SWAAIJ, WILLIBRORDUS PETRUS MARIA 1997 Dynamic simulation of dispersed gas-liquid two-phase flow using a discrete bubble model. *Chemical Engineering Science* **52** (9), 1429–1458.

VAN DEN BREMER, T.S. & HUNT, G.R. 2010 Universal solutions for boussinesq and non-boussinesq plumes. *J. of Fluid Mech.* **644**, 165–192.

Dhotre, Mahesh T. & Smith, Brian L. 2007 Cfd simulation of large-scale bubble plumes: Comparisons against experiments. *Chemical Engineering Science* **62** (23), 6615–6630.

Dou, Zhongwang, Pecenak, Zachary K., Cao, Lujie, Woodward, Scott H., Liang, Zach & Meng, Hui 2016 Piv measurement of high-reynolds-number homogeneous and isotropic turbulence in an enclosed flow apparatus with fan agitation. *Measurement Science and Technology* **27** (3), 035305.

Eaton, John K. 2009 Two-way coupled turbulence simulations of gas-particle flows using point-particle tracking. *International Journal of Multiphase Flow* **35** (9), 792–800.

Eaton, John K. & Fessler, J.R. 1994 Preferential concentration of particles by turbulence. *International Journal of Multiphase Flow* **20** (1), 169–209.

Elghobashi, S. 1994 On predicting particle-laden turbulent flows. *Applied Scientific Research* **52** (4), 309–329.

Elghobashi, S. & Truesdell, G.C. 1992 Direct simulation of particle dispersion in decaying isotropic turbulence. *J. Fluid Mech.* **242**, 655–700.

Elghobashi, S. & Truesdell, G.C. 1993 On the two-way interaction between homogeneous turbulence and dispersed solid particles. i: Turbulence modification. *Physics of Fluids A: Fluid Dynamics* **5** (7).

Esmaily-Moghadam, Mahdi & Mani, Ali 2016 Analysis of the clustering of inertial particles in turbulent flows. *Phys. Rev. Fluids* **1**, 084202.

Fagents, Sarah A., Gregg, Tracy K.P. & Lopes, Rosaly M.C. 2013 *Modeling Volcanic Processes: The Physics and Mathematics of Volcanism*. Cambridge University Press.

Falconer, Kenneth 2003 *Fractal Geometry Mathematical Foundations and Applications*. John Wiley & Sons, Ltd., West Sussex, England.

Falkovich, G., Fouxon, A. & Stepanov, M.G. 2002 Acceleration of rain initiation by cloud turbulence. *Nature* **419**, 151–154.

Ferenc, Járai-Szabó & Néda, Zoltán 2007 On the size distribution of poisson voronoi cells. *Physica A: Statistical Mechanics and its Applications* **385** (2), 518–526.

Ferrante, A. & Elghobashi, S. 2003 On the physical mechanisms of two-way coupling in particle-laden isotropic turbulence. *Physics Of Fluids* **15** (2).

Fessler, John R., Kulick, Jonathan D. & Eaton, John. K. 1994 Preferential concentration of heavy particles in a turbulent channel flow. *Physics of Fluids* **6**, 3742.

Fiscaletti, D., Westerweel, J. & Elsinga, G.E. 2014 Long-range μpiv to resolve the small scales in a jet at high reynolds number. *Exp. in Fluids* **55**, 1812.

Fornari, Walter, Picano, Francesco & Brandt, Luca 2016 Sedimentation of finite-size spheres in quiescent and turbulent environments. *J. Fluid Mech.* **788**, 640–669.

Frankel, Ari, Pouransari, H., Coletti, F. & Mani, A. 2016 Settling of heated particles in homogeneous turbulence. *J. Fluid Mech.* **792**, 869–893.

Gao, Hui, Li, Hui & Wang, Lian-Ping 2013 Lattice boltzmann simulation of turbulent flow laden with finite-size particles. *Computers & Mathematics with Applications* **65** (2), 194–210.

Garrett, Timothy J. & Yuter, Sandra E. 2014 Observed influence of riming, temperature, and turbulence on the fallspeed of solid precipitation. *Geophysical Research Letters* **41** (18), 6515–6522.

GERASHCHENKO, S., SHARP, N.S., NEUSCAMMAN, S. & WARHAFT, Z. 2008 Lagrangian measurements of inertial particle accelerations in a turbulent boundary layer. *J. Fluid Mech.* **617**, 225–281.

GIBERT, MATHIEU, XU, HAITAO & BODENSCHATZ, EBERHARD 2012 Where do small, weakly inertial particles go in a turbulent flow. *J. Fluid Mech.* **698**, 160–167.

GOOD, G.H., GERASHCHENKO, S. & WARHAFT, Z. 2012 Intermittency and inertial particle entrainment at a turbulent interface: the effect of the large-scale eddies. *J. Fluid Mech.* **694**, 371–398.

GOOD, G.H., IRELAND, P.J., BEWLEY, G.P. & BODENSCHATZ, E. 2014 Settling regimes of inertial particles in isotropic turbulence. *J. Fluid Mech.* **759**, R3.

GORE, R.A. & CROWE, C.T. 1991 Modulation of turbulence by a dispersed phase. *Journal of Fluids Engineering* **113** (2), 304–307.

GOTO, SUSUMU & VASSILICOS, J.C. 2006 Self-similar clustering of inertial particles and zero-acceleration points in fully developed two-dimensional turbulence. *Physics of Fluids* **18**, 115103.

GOTO, SUSUMU & VASSILICOS, J.C. 2008 Sweep-stick mechanism of heavry particle clustering in fluid turbulence. *Phys. Rev. Lett.* **100**.

GRAFF, DAVID B. DE & EATON, JOHN K. 2000 Reynolds-number scaling of the flat-plate turbulent boundary layer. *J. Fluid Mech.* **422**, 319–346.

GUALA, MICHELE, LIBERZON, ALEXANDER, HOYER, KLAUS, TSINOBER, ARKADY & KINZELBACH, WOLFGANG 2008 Experimental study on clustering of large particles in homogeneous turbulent flow. *Journal of Turbulence* **9**, N34.

GUALTIERI, P., SARDINA, F. PICANO G. & CASCIOLA, C.M. 2013 Clustering and turbulence modulation in particle-laden shear flows. *J. Fluid Mech.* **715**, 134–162.

GUALTIERI, P., SARDINA, F. PICANO G. & CASCIOLA, C.M. 2015 Exact regularized point particle method for multiphase flows in the two-way coupling regime. *J. Flui Mech.* **773**, 520–561.

GUSTAVSSON, K. & MEHLIG, B. 2016 Statistical models for spatial patterns of heavy particles in turbulence. *Advances in Physics* **65** (1), 1–57.

GUSTAVSSON, K., VAJEDI, S. & MEHLIG, B. 2014 Clustering of particles falling in a turbulent flow. *Phys. Rev. Lett.* **112**, 214501.

HALL, NEIL, ELENANY, MOHAMMED, ZHU, DAVID Z. & RAJARATNAM, N. 2010 Experimental study of sand and slurry jets in water. *Journal of Hydraulic Engineering* **136** (10), 727–738.

HASSAN, Y.A., BLANCHAT, T.K. & JR., C.H. SEELEY 1992 Piv flow visualisation using particle tracking techniques. *Measurement Science and Technology* **3** (7), 633.

HEARST, R.J., BUXTON, O.R.H., GANAPATHISUBRAMANI, B. & LAVOIE, P. 2012 Experimental estimation of fluctuating velocity and scalar gradients in turbulence. *Exp. in Fluids* **53** (4), 925–942.

HETSRONI, G. 1989 Particles-turbulence interaction. *International Journal of Multiphase Flow* **15** (5), 735–746.

HOLTZER, GRETCHEN L. & COLLINS, LANCE R. 2002 Relationship between the intrinsic radial distribution function for an isotropic field of particles and lower-dimensional measurements. *J. Fluid Mech.* **459**, 93–102.

HORWITZ, J.A.K. & MANI, A. 2016 Accurate calculation of stokes drag for point–particle tracking in two-way coupled flows. *Journal of Computational Physics* **318** (1), 85–109.

Huck, P. D., Bateson, C., Volk, R., Cartellier, A., Bourgoin, M. & Aliseda, A. 2018 The role of collective effects on settling velocity enhancement for inertial particles in turbulence. *J. Fluid Mech.* **846**, 1059–1075.

Hunt, G.R. & van den Bremer, T.S. 2010 Classical plume theory: 1937–2010 and beyond. *IMA Journal of Applied Mathematics* **76** (3), 424–448.

Hunt, G.R. & Kaye, N.G. 2001 Virtual origin correction for lazy turbulent plumes. *J. of Fluid Mech.* **435**, 377–396.

Hunt, G.R. & Kaye, N.B. 2005 Lazy plumes. *J. of Fluid Mech.* **533**, 329–338.

Hunt, J.C.R., Wray, A.A & Moin, P. 1988 Eddies, streams, and convergence zones in turbulent flows. *In Studying Turbulence Using Numerical Simulation Databases, 2. Proceedings of the 1988 Summer Program.* .

Hwang, W. & Eaton, J.K. 2004 Creating homogeneous and isotropic turbulence without a mean flow. *Experiments in Fluids* **36** (3), 444–454.

Hwang, Wontae & Eaton, John K. 2006a Homogeneous and isotropic turbulence modulation by small heavy ($st \sim 50$) particles. *J. Fluid Mech.* **564**, 361–393.

Hwang, Wontae & Eaton, John K. 2006b Turbulence attenuation by small particles in the absence of gravity. *International Journal of Multiphase Flow* **32** (12), 1386–1396.

Ireland, Peter J., Bragg, Andrew D. & Collins, Lance R. 2016a The effect of reynolds number on inertial particle dynamics in isotropic turbulence. part 1. simulations without gravitational effects. *J. Fluid Mech* **796**, 617–658.

Ireland, Peter J., Bragg, Andrew D. & Collins, Lance R. 2016b The effect of reynolds number on inertial particle dynamics in isotropic turbulence. part 2. simulations with gravitational effects. *J. Fluid Mech* **796**, 617–658.

IRELAND, PETER J. & DESJARDINS, OLIVIER 2017 Improving particle drag predictions in euler–lagrange simulations with two-way coupling. *Journal of Computational Physics* **338** (1), 405–430.

ISHIMA, TSUNEAKI, HISHIDA, KOICHI & MAEDA, MASANOBU 1993 Effect of particle residence time on particle dispersion in a plane mixing layer. *J. Fluids Eng.* **115** (4), 751–759.

JENNY, PATRICK, ROEKAERTS, DIRK & BEISHUIZEN, NIJSO 2012 Modeling of turbulent dilute spray combustion. *Progress in Energy and Combustion Science* **38** (6), 846–887.

JIANG, JUNSHENG, LAW, ADRIAN WING-KEUNG & CHENG, NIAN-SHENG 2005 Two-phase analysis of vertical sediment-laden jets. *Journal of Eng. Mech.* **131** (3), 308–318.

DE JONG, J., CAO, L., WOODWARD, S.H., SALAZAR, J.P.L.C., COLLINS, L.R. & MENG, H. 2009 Dissipation rate estimation from piv in zero-mean isotropic turbulence. *Experiments in Fluids* **46** (3), 499.

DE JONG, J., SALAZAR, J.P.L.C, WOODWARD, S.H., COLLINS, L.R. & MENG, H. 2010 Measurement of inertial particle clustering and relative velocity statistics in isotropic turbulence using holographic imaging. *International Journal of Multiphase Flow* **36** (4), 324–332.

KAWANISI, KIYOSI & SHIOZAKI, RYOHEI 2008 Turbulent effects on the settling velocity of suspended sediment. *J. Hydraulic Engineering* **134** (2).

KHALITOV, D.A. & LONGMIRE, E.K. 2002 Simultaneous two-phase piv by two-parameter phase discrimination. *Exp. In Fluids* **32** (2), 252–268.

KHALITOV, DANIEL A. & LONGMIRE, ELLEN K. 2003 Effect of particle size on velocity correlations in turbulent channel flow. *ASME/JSME 2003 4th Joint Fluids Summer Engineering Conference* **Volume 1: Fora, Parts A, B, C, and D**.

KIDANEMARIAM, AMAN G., CHAN-BRAUN, CLEMENS, DOYCHEV, TODOR & UHLMANN, MARKUS 2013 Direct numerical simulation of horizontal open channel flow with finite-size, heavy particles at low solid volume fraction. *New Journal of Physics* **15**.

KIGER, K.T. & PAN, C. 2000 Piv technique for the simultaneous measurement of dilute two-phase flows. *J. Fluids Eng.* **122** (4), 811–818.

KIGER, K.T. & PAN, C. 2002 Suspension and turbulence modification effects of solid particulates on a horizontal turbulent channel flow. *Journal of Turbulence* **3**.

KOLMOGOROV, AN 1941 Cr acad, sci., ussr 30, p. 302.1941 c. *CR Acad, Sci., USSR* **32**, 16.

KULICK, J.D., FESSLER, J.R. & EATON, J.K. 1993 On the interactions between particles and turbulence in a fully-developed channel flow in air. mech. engng rep. md-66.

KULICK, J.D., FESSLER, J.R. & EATON, JOHN K. 1994 Particle response and turbulence modification in fully developed channel flow. *J. Fluid Mech.* **277**, 109–134.

LAI, ADRIAN C.H., CHANG, SHU NING, LAW, ADRIAN WING-KEUNG & ADAMS, E. ERIC 2016 Spreading hypothesis of a particle plume. *Journal of Hydraulic Engineering* **142** (12), 04016065.

LANCE, M. & BATAILLE, J. 1991 Turbulence in the liquid phase of a uniform bubbly air–water flow. *J. of Fluid Mech.* **222**, 95–118.

LÁZARO, B.J. & LASHERAS, J.C. 1989 Particle dispersion in a turbulent, plane, free shear layer. *Phys. of Fluids A: Fluid Dynamics* **1**.

LIBERZON, A., GUALA, M., LÜTHI, B., KINZELBACH, W. & TSINOBER, A. 2005 Turbulence in dilute polymer solutions. *Physics of Fluids* **17** (3), 031707.

Liu, Z., Cooper, P. & Wypych, P.W. 2007 Experimental investigation of air entrainment in free-falling particle plumes. *Particulate Science and Technology* **25** (4), 357–373.

Liu, Ze Qin 2003 Air entrainment in free falling bulk materials. PhD thesis, University of Wollongong.

Longmire, Ellen K. & Eaton, John K. 1992 Structure of a particle-laden round jet. *J. Fluid Mech.* **236**, 217–257.

Lozano-Durán, Adrián, Flores, Oscar & Jiménez, Javier 2012 The three-dimensional structure of momentum transfer in turbulent channels. *J. Fluid Mech.* **694**, 100–130.

Lucci, Francesco, Frrante, Antonino & Elghobashi, Said 2010 Modulation of isotropic turbulence by particles of taylor length-scale size. *J. Fluid Mech.* **650**, 5–55.

Manville, B. & Wilson, C.J.N. 2004 Vertical density currents: a review of their potential role in the deposition and interpretation of deep-sea ash layers. *Journal of the Geological Society* **161** (6), 947–958.

Marjanovic, Goran 2018 Direct numerical simulations of single and multiphase turbulent plumes in the forced, pure and laxy regimes at large grashof numbers. PhD thesis, University of Florida.

Marusic, Ivan & Kunkel, Gary J. 2003 Streamwise turbulence intensity formulation for flat-plate boundary layers. *Physics of Fluids* **15**, 2461.

Matsude, Keigo, Onishi, Ryo & Takahashi, Keiko 2017 Influence of gravitational settling on turbulent droplet clustering and radar reflectivity factor. *Flow, Turbulence and Combustion* **98** (1), 327–340.

Maxey, M.R. 1987 The gravitational settling of aerosol particles in homogeneous turbulence and random flow fields. *J. Fluid Mech.* **174**, 441–465.

Maxey, M.R. & Corrsin, S. 1986 Free access gravitational settling of aerosol particles in randomly oriented cellular flow fields. *J. Atmos. Sci.* **43**, 1112–1134.

Maxey, Martin R. & Riley, James J. 1983 Equation of motion for a small rigid sphere in a nonuniform flow. *Physics of Fluids* **26** (4).

Mazurek, K.A., Christison, K. & Rajaratnam, N. 2002 Turbulent sand jets in water. *Journal of Hydraulic Research* **40** (4), 527–530.

McHugh, Sean T. & Cardoso, Silvana S.S. 2011 Turbulent entrainment into inert and reacting multiphase plumes. *J. of Fluid Mech.* **682**, 577–589.

McKenna, Sean P. & McGillis, Wade R. 2004 Observations of flow repeatability and secondary circulation in an oscillating grid-stirred tank. *Physics of Fluids* **16** (9), 3499–3502.

Mei, R. 1994 Effect of turbulence on the particle settling velocity in the nonlinear drag range. *International Journal of Multiphase Flow* **20** (2), 273–284.

Mei, Renwei, Adrian, Ronald J. & Hanratty, Thomas J. 1991 Particle dispersion in isotropic turbulence under stokes drag and basset force with gravitational settling. *J. Fluid Mech.* **225**, 481–495.

Mercado, Julian Martinez, Gomez, Daniel Chehata, van Gils, Dennis, Sun, Chao & Lohse, Detlef 2010 On bubble clustering and energy spectra in pseudo-turbulence. *J. of Fluid Mech.* **650**, 287–306.

Moisy, F. & Jiménez, J. 2004 Geometry and clustering of intense structures in isotropic turbulence. *J. Fluid Mech.* **513**, 111–133.

Monchaux, R., Bourgoin, M. & Cartellier, A. 2010 Preferential concentration of heavy particles: A voronoï analysis. *Physics of Fluids* **22** (10), 103304.

Monchaux, Romain, Bourgoin, Mickaël & Cartellier, Alain 2012 Analyzing preferential concentration and clustering of inertial particles in turbulence. *International Journal of Multiphase Flow* **40**, 1–18.

Monchaux, R. & Dejoan, A. 2017 Settling velocity and preferential concentration of heavy particles under two-way coupling effects in homogeneous turbulence. *Phys. Rev. Fluids* **2**, 104302.

Morton, B.R. 1959 Forced plumes. *Journal of Fluid mechanics* **5** (1), 151–163.

Morton, B.R., Taylor, Geoffrey Ingram & Turner, John Stewart 1956 Turbulent gravitational convection from maintained and instantaneous sources. *Proceedings of the Royal Society of London. Series A. Mathematical and Physical Sciences* **234** (1196), 1–23.

Mudde, Robert F. & Simonin, Oliver 1999 Two-and three-dimensional simulations of a bubble plume using a two-fluid model. *Chemical Engineering Science* **54** (21), 5061–5069.

Mydlarski, Laurent & Warhaft, Zellman 1996 On the onset of high-reynolds-number grid-generated wind tunnel turbulence. *J. of Fluid Mech.* **320**, 331–368.

Naso, Aurore & Prosperetti, Andrea 2010 The interaction between a solid particle and a turbulent flow. *New Journal of Physics* **12** (3), 033040.

Nedderman, R. M. 1992 *The prediction of mass flow rate*. Cambridge University Press.

Nemes, A., Coletti, F., Fong, K.O. & Toloui, M. 2016 Experimental observation of three-dimensional particle clustering in turbulent channel flow. *International Conference on Multiphase Flows, Florence, Italy* .

Nemes, Andras, Dasari, Teja, Hong, Jiarong, Guala, Michele & Coletti, Filippo 2017 Snowflakes in the atmospheric surface layer: observation of particle–turbulence dynamics. *J. Fluid Mech.* **814**, 592–613.

Nemes, András, Jacono, David Lo, Blackburn, Hugh M. & Sheridan, John 2015 Mutual inductance of two helical vortices. *J. Fluid Mech.* **774**, 298–310.

Nielsen, Peter 1993 Turbulence effects on the settling of suspended particles. *Journal of Sedimentary Research* **63** (5), 835–838.

Obligado, Martín, Teitelbaum, Tomás, Cartellier, Alain, Mininni, Pablo & Bourgoin, Mickaël 2014 Preferential concentration of heavy particles in turbulence. *Journal of Turbulence* **15** (5), 293–310.

Ohmi, K. & Li, H.Y. 2000 Particle-tracking velocimetry with new algorithms. *Measurement Science and Technology* **11** (6), 603.

Paola, G. De, Kim, I.S. & Mastorakos, E. 2009 Second-order conditional moment closure simulations of autoignition of an n-heptane plume in a turbulent coflow of heated air. *Flow, Turbulence and Combustion* **82** (4), 455.

Paris, A.D. 2001 Turbulence attenuation in a particle-laden channel flow. PhD thesis, Stanford University.

Parthasarathy, R.N. & Faeth, Gerard M. 1987 Structure of particle-laden turbulent water jets in still water. *International Journal of Multiphase Flow* **13** (5), 699–716.

Perry, A.E. & Chong, M.S. 1994 Topology of flow patterns in vortex motions and turbulence. *Applied Scientific Research* **53** (3-4), 357–374.

Poelma, Christian & Ooms, Gijs 2006 Particle-turbulence interaction in a homogeneous, isotropic turbulent suspension. *ASME. Appl. Mech. Rev.* **59** (2), 78–90.

Poelma, C., Westerweel, J. & Ooms, G. 2007 Particle-fluid interactions in grid-generated turbulence. *J. Fluid Mech.* **589**, 315–351.

Prosperetti, Andrea & Tryggvason, Grétar 2009 *Computational Methods for Multiphase Flow*. Cambridge University Press.

Rabencov, B. & van Hout, R. 2015 Voronoi analysis of beads suspended in a turbulent square channel flow. *International Journal of Multiphase Flow* **68**, 10–13.

Raffel, Markus, Willert, Christian E., Scarano, Fulvio, Kähler, Christian J., Wereley, Steven T. & Kompenhans, Jürgen 2018 *Particle Image Velocimetry: A Practical Guide*, 3rd edn. Springer International Publishing.

Ramaprian, B.R. & Chandrasekhara, M.S. 1989 Measurements in vertical plane turbulent plumes. *J. Fluids Eng.* **111** (1), 69–77.

Reade, Walter C. & Collins, Lance R. 2000 Effect of preferential concentration on turbulent collision rates. *Physics of Fluids* **12**, 2530.

Reeks, M.W. 1977 On the dispersion of small particles suspended in an isotropic turbulent fluid. *J. Fluid Mech.* **83** (3), 529–546.

Ricou, Francis Paul & Spalding, D.B. 1961 Measurements of entrainment by axisymmetrical turbulent jets. *J. of Fluid Mech.* **11** (1), 21–32.

Risso, Frédéric & Ellingsen, Kjetil 2002 Velocity fluctuations in a homogeneous dilute dispersion of high-reynolds-number rising bubbles. *J. of Fluid Mech.* **453**, 395–410.

Rogers, C.B. & Eaton, J.K. 1991 The effect of small particles on fluid turbulence in a flat-plate, turbulent boundary layer in air. *Physics of Fluids A: Fluid Dynamics* **3** (5).

ROGERS, CHRIS B. & EATON, JOHN K. 1989 *The interaction between dispersed particles and fluid turbulence in a flat-plate turbulent boundary layer in air*. Stanford University.

ROONEY, G.G. & LINDEN, P.F. 1996 Similarity considerations for non-boussinesq plumes in an unstratified environment. *J. of Fluid Mech.* **318**, 237–250.

ROSA, BOGDAN, PARISHANI, HOSSEIN, AYALA, ORLANDA & WANG, LIAN-PING 2016 Settling velocity of small inertial particles in homogeneous isotropic turbulence from high-resolution dns. *International Journal of Multiphase Flow* **83**, 217–231.

RUDOFF, R. & BACHALO, W. 1988 Direct particle–fluid simulation of kolmogorov-length-scale size particles in decaying isotropic turbulencemeasurements of droplet drag coefficients in a polydispersed turbulent flow field. *26th Aerospace Sciences Meeting. Reno,NV,U.S.A.* .

SABBAN, LILACH & VAN HOUT, RENÉ 2011 Measurements of pollen grain dispersal in still air and stationary, near homogeneous, isotropic turbulence. *Journal of Aerosol Science* **42** (12), 867–882.

SAHU, S., HARDALUPAS, Y. & TAYLOR, A.M.K.P. 2014 Droplet–turbulence interaction in a confined polydispersed spray: effect of droplet size and flow length scales on spatial droplet–gas velocity correlations. *J. of Fluid Mech.* **741**, 98–138.

SAHU, S., HARDALUPAS, Y. & TAYLOR, A.M.K.P. 2016 Droplet–turbulence interaction in a confined polydispersed spray: effect of turbulence on droplet dispersion. *J. Fluid Mech.* **794**, 267–309.

SALAZAR, JUAN P.L.C. & COLLINS, LANCE R. 2012 Inertial particle acceleration statistics in turbulence: Effects of filtering, biased sampling, and flow topology. *Physics of Fluids* **24**, 083302.

SALAZAR, JUAN P.L.C, DE JONG, JEREMY, CAO, LUJIE & WOODWARD, SCOTT H. 2008 Experimental and numerical investigation of inertial particle clustering in isotropic turbulence. *J. Fluid Mech.* **600**, 245–256.

SAW, EWE-WEI, BEWLEY, GREGORY P., BODENSCHATZ, EBERHARD, RAY, SAMRIDDHI SANKAR & BEC, JÉRÉMIE 2014 Extreme fluctuations of the relative velocities between droplets in turbulent airflow. *Physics of Fluids* **26** (11).

SAW, E.-W., DEBUE, P., KUZZAY, D., DAVIAUD, F. & DUBRULLE, B. 2018 On the universality of anomalous scaling exponents of structure functions in turbulent flows. *J. Fluid Mech.* **837**, 657–669.

SAW, EWE WEI, SHAW, RAYMOND A., AYYALASOMAYAJULA, SATHYANARAYANA, CHUANG, PATRICK Y. & ÁRMANN GYLFASON 2008 Inertial clustering of particles in high-reynolds-number turbulence. *Phys. Rev. Lett.* **100** (21), 214501.

SAW, EWE-WEI, SHAW, RAYMOND A., SALAZAR, JUAN P.L.C. & COLLINS, LANCE R. 2012 Spatial clustering of polydisperse inertial particles in turbulence: Ii. comparing simulation with experiment. *New Journal of Physics* **14** (10), 105031.

SCHANZ, DANIEL, GESEMANN, SEBASTIAN & SCHRÖDER, ANDREAS 2016 Shake-the-box: Lagrangian particle tracking at high particle image densities. *Exp. in Fluids* **57** (5), 70.

SCHILLER, L & NAUMANN, A 1933 Drag coefficient for spherical shape. *VDI, Zeits* **13**, 318.

SCHMIDT, W. 1941a Turbulente ausbreitung eines stromes erhitzter luft. teil i. *Z. Angew Math. Mech.* **21**, 265–278.

SCHMIDT, W. 1941b Turbulente ausbreitung eines stromes erhitzter luft. teil ii. *Z. Angew Math. Mech.* **21**, 351–363.

Scollo, Simona, Bonadonna, Costanza & Manzella, Irene 2017 Settling-driven gravitational instabilities associated with volcanic clouds: new insights from experimental investigations. *Bulletin of Volcanology* **79** (6), 39.

Scollo, Simona, Tarantola, Stefano, Bonadonna, Costanza, Coltelli, Mauro & Saltelli, Andrea 2008 Sensitivity analysis and uncertainty estimation for tephra dispersal models. *Journal of Geophysical Research: Solid Earth* **113** (B6).

Seol, Dong-Guan, Bhaumik, Tirtharaj, Bergmann, Christian & Socolofsky, Scott A. 2007 Particle image velocimetry measurements of the mean flow characteristics in a bubble plume. *J. of Eng. Mech.* **133** (6), 665–676.

Shabbir, Aamir & George, William K. 1994 Experiments on a round turbulent buoyant plume. *J. of Fluid Mech.* **275**, 1–32.

Shaw, Raymond A. 2003 Particle-turbulence interactions in atmospheric clouds. *Annual Review of Fluid Mechanics* **35**, 183–227.

Socolofsky, S.A. & Adams, E.E. 2002 Multi-phase plumes in uniform and stratified crossflow. *J. of Hydraul. Research* **40** (6), 661–672.

Soldati, Alredo & Marchioli, Christian 2009 Physics and modelling of turbulent particle deposition and entrainment: Review of a systematic study. *International Journal of Multiphase Flow* **35** (9), 827–839.

Squires, Kyle D. & Eaton, John K. 1991 Preferential concentration of particles by turbulence. *Phys. of Fluids A: Fluid Dynamics* **3**.

Squires, Kyle D. & Eatons, John K. 1991 Measurements of particles dispersion obtained from direct numerical simulations of isotropic turbulence. *J. Fluid Mech.* **226**, 1–35.

Sumbekova, Sholpan, Cartellier, Alain, Aliseda, Alberto & Bourgoin, Mickaël 2017 Preferential concentration of inertial sub-kolmogorov particles: The roles of mass loading of particles, stokes numbers, and reynolds numbers. *Phys. Rev. Fluids* **2**, 024302.

Sundaram, Shivshankar & Collins, Lance R. 1997 Collision statistics in an isotropic particle-laden turbulent suspension. part 1. direct numerical simulations. *J. Fluid Mech.* **335**, 75–109.

Sundaram, Shivshankar & Collins, Lance R. 1999 A numerical study of the modulation of isotropic turbulence by suspended particles. *J. Fluid Mech.* **379**, 105–143.

Tagawa, Yoshiyuki, Mercado, Julián Martínez, Prakash, Vivek N., Calzavarini, Enrico, Sun, Chao & Lohse, Detlef 2012 Three-dimensional lagrangian voronoï analysis for clustering of particles and bubbles in turbulence. *J. Fluid Mech.* **693**, 201–215.

Tanaka, Tomohiko & Eaton, John K. 2008 Classification of turbulence modification by dispersed spheres using a novel dimensionless number. *Phys. Rev. Lett.* **101**, 114502.

Tanaka, Tomohiko & Eaton, John K. 2010 Sub-kolmogorov resolution partical image velocimetry measurements of particle-laden forced turbulence. *J. Fluid Mech.* **643**, 177–206.

Tang, Dongming & Marangoni, Alejandro G. 2006 3d fractal dimension of fat crystal networks. *Chemical Physics Letters* **433** (1-3), 248–252.

Taub, Gordon N. 2013 A numerical and experimental study of turbulent single and multiphase forced plumes and jets at moderate reynolds numbers. PhD thesis.

Taylor, G.I. 1946 *Dynamics of a mass of hot gas rising in air*, , vol. 919. Technical Information Division, Oak Ridge Operations.

TAYLOR, GEOFFREY INGRAM 1935 Statistical theory of turbulence iv-diffusion in a turbulent air stream. *Proceedings of the Royal Society of London. Series A-Mathematical and Physical Sciences* **151** (873), 465–478.

TCHEN, C.M. 1947 Mean value and correlation problems connected with the motion of small particles in a turbulent fluid. PhD thesis, Dissertation-Delft, The Hague, Martinus Nijhoff.

TENNETI, SUDHEER & SUBRAMANIAM, SHANKAR 2014 Particle-resolved direct numerical simulation for gas-solid flow model development. *Annual Review of Fluid Mechanics* **46**, 199–230.

TOOBY, PAUL F., WICK, GERALD L. & ISAACS, JOHN D. 1977 The motion of a small sphere in a rotating velocity field: A possible mechanism for suspending particles in turbulence. *J. Geophysical Research* **82** (15), 2096–2100.

TURNER, JOHN STEWART 1979 *Buoyancy effects in fluids*. Cambridge university press.

UHLMANN, MARKUS & DOYCHEV, TODOR 2014 Sedimentation of a dilute suspension of rigid spheres at intermediate galileo numbers: the effect of clustering upon the particle motion. *J. Fluid Mech.* **752**, 310–348.

VARIANO, EVAN A., BODENSCHATZ, EBERHARD & COWEN, EDWIN A. 2004 A random synthetic jet array driven turbulence tank. *Experiments in Fluids* **37** (4), 613–615.

VARIANO, EVAN A. & COWEN, EDWIN A. 2008 A random-jet-stirred turbulence tank. *J. Fluid Mech.* **604**, 1–32.

VOLK, R., CALZAVARINI, E., VERHILLE, G., LOHSE, D., MORDANT, N., PINTON, J.-F. & TOSCHI, F. 2008 Acceleration of heavy and light particles in turbulence: Comparison between experiments and direct numerical simulations. *Physica D: Nonlinear Phenomena* **237** (14-17), 2084–2089.

VOTH, GREG A., LA PORTA, ARTHUR, CRAWFORD, ALICE M., ALEXANDER, JIM & BODENSCHATZ, EBERHARD 2002 Measurement of particle accelerations in fully developed turbulence. *Journal of Fluid Mechanics* **469**, 121–160.

WANG, L.-P., AYALA, O. & GRABOWSKI, W.W. 2007 Effects of aerodynamic interactions on the motion of heavy particles in a bidisperse suspension. *Journal of Turbulence* **8**.

WANG, LIAN-PING & MAXEY, MARTIN R. 1993 Settling velocity and concentration distribution of heavy particles in homogeneous isotropic turbulence. *J. Fluid Mech* **256**, 27–68.

WANG, LIAN-PING & STOCK, DAVD E. 1993 Dispersion of heavy particles by turbulent motion. *J. Atmos. Sci.* **50**, 1897–1913.

WANG, LIAN-PING, WEXLER, ANTHONY S. & ZHOU, YONG 2000 Statistical mechanical description and modelling of turbulent collision of inertial particles. *J. Fluid Mech.* **415**, 117–153.

WARNICA, W.D., RENKSIZBULUT, M. & STRONG, A.B. 1995 Drag coefficients of spherical liquid droplets part 2: Turbulent gaseous fields. *Exp. in Fluids* **18** (4), 265–276.

WELLS, M.R. & STOCK, D.E. 1983 The effects of crossing trajectories on the dispersion of particles in a turbulent flow. *J. Fluid Mech.* **136**, 31–62.

WESTERWEEL, JERRY & SCARANO, FULVIO 2005 Universal outlier detection for piv data. *Exp. in Fluids* **39**, 1096–1100.

WILKINSON, M. & MEHLIG, B. 2005 Caustics in turbulent aerosols. *Europhysics Letters* **71** (2), 186.

Woittiez, Eric J.P., Jonker, Harm J.J. & Portela, Luís 2009 On the combined effects of turbulence and gravity on droplet collisions in clouds: A numerical study. *Journal of the Atmospheric Sciences* **66** (7), 1926–1943.

Wood, A.M., Hwang, W. & Eaton, J.K. 2005 Preferential concentration of particles in homogeneous and isotropic turbulence. *International Journal of Multiphase Flow* **31** (10-11), 1220–1230.

Wood, Ian R., Bell, Robert G. & Wilkinson, David L. 1993 *Ocean disposal of wastewater*. World Scientific.

Worth, N.A. & Nickels, T.B. 2011 Time-resolved volumetric measurement of fine-scale coherent structures in turbulence. *Physical Review E* **84** (2), 025301.

Worth, N.A., Nickels, T.B. & Swaminathan, N. 2010 A tomographic piv resolution study based on homogeneous isotropic turbulence dns data. *Exp. in Fluids* **49** (3), 637–656.

Wu, J.-S. & Faeth, G.M. 1994 Sphere wakes at moderate reynolds numbers in a turbulent environment. *AIAA Journal* **32** (3), 535–54166.

Yang, C.Y. & Lei, U. 1998 The role of the turbulent scales in the settling velocity of heavy particles in homogeneous isotropic turbulence. *J. Fluid Mech.* **371**, 179–205.

Yang, T.S. & Shy, S.S. 2003 The settling velocity of heavy particles in an aqueous near-isotropic turbulence. *Physics of Fluids* **15** (4).

Yang, T.S. & Shy, S.S. 2005 Two-way interaction between solid particles and homogeneous air turbulence: particle settling rate and turbulence modification measurements. *J. Fluid Mech.* **526**, 171–216.

Yoshimoto, Hiroshi & Goto, Susumu 2007 Self-similar clustering of inertial particles in homogeneous turbulence. *J. Fluid Mech.* **577**, 275–286.

YUDINE, M.I. 1959 Physical considerations on heavy-particle diffusion. *Advances in Geophysics* **6**, 185–191.

ZAICHIK, LEONID I. & ALIPCHENKOV, VLADIMIR M. 2009 Statistical models for predicting pair dispersion and particle clustering in isotropic turbulence and their applications. *New Journal of Physics* **11**.

ZAMANSKY, R., COLETTI, F., MASSOT, M. & MANI, A. 2016 Turbulent thermal convection driven by heated inertial particles. *J. Fluid Mech.* **809**, 390–437.

ZELDOVICH, Y.B. 1937 The asymptotic laws of freely-ascending convective flows. *Zh. Eksp. Teor. Fiz.* **7**, 1463–1465, english translation in Selected Works of Yakov Borisovich Zeldovich, 1, 1992 (J. P. Ostriker ed.), 82–85, Princeton University Press.

ZHAO, L.H., MARCHIOLI, C. & ANDERSSON, H.I. 2012 Stokes number effects on particle slip velocity in wall-bounded turbulence and implications for dispersion models. *Physics of Fluids* **24**, 021705.

ZIMMERMANN, ROBERT, XU, HAITAO, GASTEUIL, YOANN, BOURGOIN, MICKAËL, VOLK, ROMAIN, PINTON, JEAN-FRANÇOIS & BODENSCHATZ, EBERHARD 2010 The lagrangian exploration module: An apparatus for the study of statistically homogeneous and isotropic turbulence. *Review of Scientific Instruments* **81** (5), 055112.